

1

UNIVERSITY OF BRISTOL

2

DOCTORAL THESIS

3

4

Investigating, implementing, and creating methods for analysing large neuronal ensembles

5

6

Author:

Thomas J. DELANEY

Supervisors:

Dr. Cian O'DONNELL

Dr. Michael C. ASHBY

7

*A thesis submitted in fulfillment of the requirements
for the degree of Doctor of Philosophy*

8

in the

9

Biological Intelligence & Machine Learning Unit
Department of Computer Science

10

11

July 12, 2020

¹⁵ **Declaration of Authorship**

¹⁶ I declare that the work in this dissertation was carried out in accordance with the require-
¹⁷ ments of the University's Regulations and Code of Practice for Research Degree Programmes
¹⁸ and that it has not been submitted for any other academic award. Except where indicated by
¹⁹ specific reference in the text, the work is the candidate's own work. Work done in collabora-
²⁰ tion with, or with the assistance of, others, is indicated as such. Any views expressed in the
²¹ dissertation are those of the author.

²² Signed:

²³ _____

²⁴ Date:

²⁵ _____

26 *Abstract*

27 Since the use of multi-electrode recording in neuroscience began, the number neurons
28 being recorded in parallel has been increasing. Recently developed methods using calcium
29 or voltage imaging have also contributed to the growth in neuronal datasets. As datasets grow,
30 the need for new analysis methods also grows. In this research we attempted to address some
31 of the problems associated with reading from large neuronal ensembles using fluorescent
32 calcium indicators, and some of the problems with analysing data read from large neuronal
33 ensembles.

34 We created a biophysical model for the fluorescence trace produced by a calcium indicator
35 responding to a given spike train. Our model reproduced the characteristics of a real
36 fluorescence trace recognised by spike inference algorithms. This model will be useful for
37 anyone using or considering calcium imaging.

38 To find order in the correlated behaviour of a large multi-region neuronal ensemble, we
39 applied a novel method from network science to detect structure and communities in correlated
40 behaviour. We investigated the similarities between these communities and their brain
41 anatomy. Our results indicate local correlated networks function at shorter timescales (<
42 50ms), while multi-region correlated networks function over longer timescales (> 100ms).
43 This result agrees with previous findings from EEG data, but has not been shown before using
44 spiking data.

45 We developed a statistical model for the number of neurons spiking in a neuronal ensemble
46 based on the Conway-Maxwell-binomial distribution. Our aim was to capture correlated
47 activity in a neuronal population without measuring correlation coefficients directly. The
48 model captured correlated activity at very short timescales better than measuring correlation
49 coefficients. We also replicated one of the findings of Churchland et al. (2010) relating to
50 the quenching of neural variability at stimulus onset. We propose a connection between this
51 result and the changes in association captured by our model.

Acknowledgements

53 I would like to thank my supervisors, Cian O'Donnell and Mike Ashby, for their help, en-
54 couragement, advice, and patience over the last four years. This includes not only helping
55 with research, but also enabling and encouraging me to make the most of my opportunities
56 during that time. Without their help, I would not have grown as much as I have done in those
57 years. I very grateful for their time and effort.

58 I would also like to thank the members of the Bristol Computational Neuroscience Unit
59 for introducing me to all the various aspects of computer science, neuroscience, and machine
60 learning, of which I otherwise would not have heard. As the first person to introduce me to
61 the concept of mathematical neuroscience during my undergraduate days, and a great source
62 of advice and guidance during my PhD, I would also like to thank Conor Houghton.

63 Personally, I would to thank my girlfriend Ashley, who has been nothing but helpful since
64 I met her.

65 Finally, I would like to that my father, mother, brother and sister. I am truly fortunate to
66 have such a good family. I thank them for their love, encouragement, and excellent example.

67 **Contents**

68	Declaration of Authorship	iii
69	Abstract	v
70	Acknowledgements	vii
71	1 Introduction	1
72	1.1 Overview	1
73	1.2 Modelling the fluorescence of calcium indicators	2
74	1.3 Functional networks	4
75	1.4 A new statistical model for capturing correlated behaviour	6
76	2 Sensitivity of the spikes-to-fluorescence transform to calcium indicator and neu-	
77	ron properties	9
78	2.1 Introduction	10
79	2.2 Methods	12
80	2.2.1 Calcium dynamics model	12
81	Photon release & capture	14
82	2.2.2 Parameter optimisation	15
83	Fixed parameters	16
84	2.2.3 Julia	18
85	2.2.4 Spike inference	18
86	Comparing spike inference quality	20
87	2.2.5 Perturbation analysis	20
88	2.2.6 Signal-to-noise ratio	21
89	2.2.7 Data sources	21
90	2.3 Results	21
91	2.3.1 A biophysical computational model can generate accurate fluores-	
92	cence traces from spike trains	21

93	2.3.2	Spike inference algorithms perform similarly on real data compared with time series simulated from the model	22
94	2.3.3	Relative effects of various buffers to the fluorescence signal	23
95	2.3.4	Spike inference accuracy is sensitive to indicator properties, and likely varies within and between cells	26
96	2.3.5	Single spike inference accuracy drops for high firing rates, but firing rate itself can be estimated from mean fluorescence amplitude	31
97	2.4	Discussion	31
101	3	Functional networks expand across anatomical boundaries as correlation time- scale increases	35
102	3.1	Introduction	36
103	3.2	Data	37
104	3.2.1	Brain regions	37
105	3.2.2	Video recordings	38
106	3.3	Methods	38
107	3.3.1	Binning data	38
108	3.3.2	Correlation coefficients	39
109		Total correlations, r_{SC}	39
110		Shuffled total correlations	40
111		Separating Correlations & Anti-correlations	40
112	3.3.3	Conditioning on behavioural data	40
113		Linear regression	40
114		Elastic net regularisation	41
115		Conditional covariance	41
116		Measures of conditional correlation	42
117	3.3.4	Information Theory	43
118		Entropy $H(X)$	43
119		Maximum entropy limit	43
120		Mutual Information $I(X; Y)$	44
121		Variation of Information $VI(X, Y)$	46
122		Measuring entropies & mutual information	46
123	3.3.5	Network analysis	46
124		Correlation networks	46
125			

126	Rectified correlations	47
127	Sparsifying data networks	47
128	Communities	47
129	Weighted configuration model	48
130	Sparse weighted configuration model	48
131	Spectral rejection	48
132	Node rejection	49
133	Community detection	50
134	3.3.6 Clustering Comparison	50
135	Adjusted Rand Index	50
136	Clusterings as random variables	51
137	Information based similarity measures	52
138	Information based metrics	52
139	Comparing detected communities and anatomical divisions	53
140	3.4 Results	53
141	3.4.1 Average correlation size increases with increasing time bin width . .	54
142	3.4.2 Goodness-of-fit for Poisson and Gaussian distributions across increasing time bin widths	56
143	3.4.3 Differences between and inter- and intra- regional correlations decrease with increasing bin width	56
144	3.4.4 Connected and divided structure in correlation based networks reduces in dimension with increasing bin width	59
145	3.4.5 Detecting communities in correlation based networks	60
146	3.4.6 Functional communities resemble anatomical division at short timescales	63
147	3.4.7 Conditional correlations & signal correlations	63
148	3.4.8 Absolute correlations and negative rectified correlations	68
149	3.5 Discussion	69
150	4 A simple two parameter distribution for modelling neuronal activity and capturing neuronal association	75
151	4.1 Introduction	76
152	4.2 Data	77
153	4.2.1 Experimental protocol	77
154	4.3 Methods	78

159	4.3.1	Binning data	78
160	4.3.2	Number of <i>active</i> neurons	78
161	4.3.3	Moving windows for measurements	78
162	4.3.4	Fano factor	80
163	4.3.5	Probability Distributions suitable for modelling ensemble activity	80
164		Association	80
165		Binomial distribution	81
166		Beta-binomial distribution	81
167		Conway-Maxwell-binomial distribution	82
168	4.3.6	Fitting	84
169	4.3.7	Goodness-of-fit	86
170	4.4	Results	86
171	4.4.1	Increases in mean number of active neurons and variance in number of active neurons at stimulus onset in some regions	86
172		Primary visual cortex	87
173		Hippocampus	87
174		Thalamus	87
175	4.4.2	Conway-Maxwell-binomial distribution is usually a better fit than binomial or beta-binomial	87
176	4.4.3	Conway-Maxwell-binomial distribution captures changes in association at stimulus onset	92
177	4.4.4	Replicating stimulus related quenching of neural variability	92
178	4.5	Discussion	94
182	5	Studies with practical limitations & negative results	97
183	5.1	Dynamic state space model of pairwise and higher order neuronal correlations	98
184	5.2	A multiscale model for hierarchical data applied to neuronal data	98
186	6	Discussion	101
187	Bibliography		109

¹⁸⁸ List of Figures

189	2.1 A: Example spike train (blue) and the corresponding GCaMP6s fluorescence	
190	trace (green), data replotted from (Berens et al., 2018). Inset shows zoomed	
191	section of traces to highlight slow decay of GCaMP6s fluorescence relative	
192	to spike time intervals. B: Schematic diagram of the neuron calcium and	
193	GCaMP computational model. C: Good visual match of data fluorescence	
194	trace (green) and model simulated fluorescence (orange) in response to an	
195	identical spike train (blue).	11
196	2.2 A: Workflow to compare spike inference for real versus simulated fluores-	
197	cence data. B: True positive rates achieved by three different spike inference	
198	algorithms when applied to observed spike trains, and simulated spike trains.	
199	Data points overlaid as blue circles. The performance is similar from real	
200	and simulated data for each of the algorithms.	24
201	2.3 Calcium Buffering Dynamics (A) The proportions of bound and free cal-	
202	cium concentrations within a cell, with the associated spike train. (B)-(F)	
203	The dynamics of the concentration of (B) excited indicator bound calcium,	
204	(C) indicator bound calcium, (D) immobile endogenous buffer bound cal-	
205	cium, (E) mobile endogenous buffer bound calcium, and (F) free calcium in	
206	response to an action potential at $\sim 23.2\text{s}$	25
207	2.4 (A) An example trace for each of the five pairs of values used for the binding	
208	and unbinding rates of the fluorescent calcium indicator. (B) The signal-to-	
209	noise ratio of the modelled fluorescence traces using each of the four per-	
210	turbed value pairs, and the experimental value. The SNRs for the value pairs	
211	perturbed downward are lower than that for the unperturbed value pair or	
212	the higher value pairs. (C) The true-positive rates of the deconvolution al-	
213	gorithm's predictions when inferring from the observed data, and inferring	
214	from modelled traces using the perturbed and experimental values.	27

215	2.5 (A) An example trace for each of the five perturbed values for the concen-	
216	tration of fluorescent calcium indicator. The top two traces are produced	
217	by the lower perturbed values, the middle trace is produced by the experi-	
218	mental value, and the lowest two traces are produced when using the higher	
219	perturbed values. (B) The signal-to-noise ratio of the modelled fluorescence	
220	traces using each of the four perturbed values, and the experimental value.	
221	Extreme perturbations of the concentration either above or below the experi-	
222	mental level lowered the SNR. (C) The true-positive rates of the deconvolu-	
223	tion algorithm's predictions when inferring from the observed data, and	
224	inferring from modelled traces using the perturbed and experimental values.	
225	We found that the algorithms performs equally badly on the two most ex-	
226	treme values, and performs equally well on the experimental value, and the	
227	next higher perturbed value.	28
228	2.6 (A) An example trace for each of the five perturbed values for the concen-	
229	tration of immobile endogenous buffer. (B) The signal-to-noise ratio of the	
230	modelled fluorescence traces using each of the four perturbed values, and	
231	the experimental value. The lower values for the immobile buffer produce	
232	the same SNR as the experimental value. But the higher perturbed values	
233	produce fluorescence traces with a lower SNR. (C) The true-positive rates of	
234	the deconvolution algorithm's predictions when inferring from the observed	
235	data, and inferring from modelled traces using the perturbed and experimen-	
236	tal values.	30
237	2.7 Simulating fluorescence traces at different firing rates Example modelled	
238	traces created using simulated spike trains with a mean firing rate of 1Hz	
239	(left column), 5Hz (middle column), and 10Hz (right column). Note the	
240	difference in amplitude with different mean firing rates.	32
241	2.8 Inference quality and $\Delta F/F_0$ vs Firing rate (left) The spike inference ac-	
242	curacy when applied to 30 traces created using simulated spike trains with	
243	mean firing rates of 1, 5, and 10 Hz. (right) The mean $\Delta F/F_0$ across those	
244	30 traces for each frequency.	32
245	3.1 Probe Locations: The locations of the probes in each of the three mouse	
246	brains (Stringer et al., 2019).	38

247	3.2	Entropy Limit: The upper limit on entropy of binned spike count data as a function of the maximum observed spike count. The orange line is the analytical maximum. The blue line is the entropy of samples with $N = 1000$ data points taken from the discrete uniform distribution.	44
251	3.3	(A) An example of the correlation coefficients between two different pairs of cells, one where both cells are in the same brain region (intra-regional pair), and one where both cells are in different brain regions (inter-regional pair). The correlation coefficients have been measured using different time bin widths, ranging from 5ms to 3s. Note the increasing amplitude of the correlations with increasing bin width. (B) A raster plot showing the spike times of each pair of cells.	54
258	3.4	Mean correlation coefficients measured from pairs of 50 randomly chosen neurons. (A) All possible pairs, (B) positively correlated pairs, and (C) neg- atively correlated pairs. (D) Mean and standard error of χ^2 test statistics for Poisson and Gaussian distributions fitted to neuron spike counts.	55
262	3.5	(Left)The mean intra-region and inter-region correlations using all possible pairs of ~ 500 neurons, spread across 9 different brain regions. (Right) Courtesy of Stringer et al. (2019), mean inter-regional (out-of-area) corre- lation coefficients vs mean intra-regional (within-area) correlation coefficients for a bin width of 1.2s. Note that the intra-regional coefficients are higher in each case.	57
268	3.6	The mean intra-regional correlations (coloured dots) and mean inter-regional correlations (black dots) for a given region, indicated on the x-axis, for dif- ferent time bin widths. Each black dot represents the mean inter-regional correlations between the region indicated on the x-axis and one other region. (A) shows these measurements when we used a time bin width of 5ms. (B) shows these measurements when we used a time bin width of 1s. Note that the difference between the mean inter-regional correlations and mean intra- regional correlations is smaller for 1s bins.	58
276	3.7	Mean inter-regional (main diagonal) and intra-regional (off diagonal) corre- lation coefficients. (A) Shows these measurements when spike times were binned using 5ms time bins. (B) Shows the same, using 1s time bins. Note that the matrices are ordered according to the main diagonal values, therefore the ordering is different in each subfigure.	59

281	3.8 The number of dimensions in the k -partite and connected structure in the cor-	
282	relation based networks beyond the structure captured by a sparse weighted	
283	configuration null network model (see section 3.3.5), shown for different time	
284	bin widths. Note that the k -partite structure disappears for time bin width	
285	greater than 200ms for all three subjects. The dimension of the connected	
286	structure reduces with increasing bin width for 2 of the 3 subjects (top row).	61
287	3.9 (A-B) Correlation matrices with detected communities indicated by white	
288	lines. Each off main diagonal entry in the matrix represents a pair of neu-	
289	rons. Those entries within a white square indicate that both of those neurons	
290	are in the same community as detected by our community detection proce-	
291	dure. Matrices shown are for 5ms and 1s time bin widths respectively. Main	
292	diagonal entries were set to 0. (C-D) Matrices showing the anatomical dis-	
293	tribution of pairs along with their community membership. Entries where	
294	both cells are in the same region are given a colour indicated by the colour	
295	bar. Entries where cells are in different regions are given the grey colour also	
296	indicated by the colour bar.	62
297	3.10 (A) The variation of information is a measure of distance between cluster-	
298	ings. The distance between the anatomical ‘clustering’ and community de-	
299	tection ‘clustering’ increases with increasing time bin width. (B) The ad-	
300	justed Rand index is a normalised similarity measure between clusterings.	
301	The anatomical and community detection clusterings become less similar as	
302	the time bin width increases.	64
303	3.11 Comparing the components of the total covariance across different values for	
304	the time bin width. We observed a consistent increase in $E[\text{cov}(X, Y Z)]$ as	
305	the time bin width increased. But we saw different trends for $\text{cov}(E[X Z], E[Y Z])$	
306	for each mouse.	65
307	3.12 Comparing the components of the total covariance across different values for	
308	the time bin width. We saw a consistent increase in $\rho_{X,Y Z}$ as the time bin	
309	width increased in all three subjects. But we saw different trends in ρ_{signal} for	
310	each of the subjects.	66

311	3.13 Matrices showing the regional membership of pairs by colour, and the com-	
312	munities in which those pairs lie. (A-B) Detected communities and regional	
313	membership matrix for network based on rectified spike count correlation	
314	$\rho_{X,Y Z}$, using time bin widths of 0.005s and 1s respectively. (C-D) Detected	
315	communities and regional membership matrix for network based on rectified	
316	signal correlation ρ_{signal} , using time bin widths of 0.005s and 1s respectively.	67
317	3.14 Distance and similarity measures between the anatomical division of the neu-	
318	rons, and the communities detected in the network based on the spike count	
319	correlations $\rho_{X,Y Z}$. (A) The variation of information is a ‘distance’ mea-	
320	sure between clusterings. The distance between the anatomical ‘clustering’	
321	and the community clustering increases as the time bin width increases. (B)	
322	The adjusted Rand index is a similarity measure between clusterings. The	
323	detected communities become less similar to the anatomical division of the	
324	cells as the time bin width increases.	68
325	3.15 Distance and similarity measures between the anatomical division of the neu-	
326	rons, and the communities detected in the network based on the signal cor-	
327	relations ρ_{signal} . (A) The variation of information is a ‘distance’ measure be-	
328	tween clusterings. The distance between the anatomical ‘clustering’ and the	
329	community clustering increases as the time bin width increases. (B) The ad-	
330	justed Rand index is a similarity measure between clusterings. The detected	
331	communities become less similar to the anatomical division of the cells as	
332	the time bin width increases.	69
333	3.16 (A-B) Absolute correlation matrices with detected communities indicated by	
334	white lines. These communities are based on the absolute value of the total	
335	correlation between each pair of cells. Those entries within a white square in-	
336	dicate that both of those neurons are in the same community. Matrices shown	
337	are for 5ms and 1s time bin widths respectively. Main diagonal entries were	
338	set to 0. (C-D) Matrices showing the anatomical distribution of pairs along	
339	with their community membership. Regional membership is indicated by the	
340	colour bar. (E) Variation of information between the anatomical division of	
341	the cells, and the detected communities. (F) Adjusted Rand index between	
342	the anatomical division, and the detected communities.	70

343	3.17 (A-B) Sign reversed rectified correlation matrices with detected communities indicated by white lines. Those entries within a white square indicate that both of those neurons are in the same community. Matrices shown are for 5ms and 1s time bin widths respectively. Main diagonal entries were set to 0. (C-D) Matrices showing the anatomical distribution of pairs along with their community membership. Regional membership is indicated by the colour bar. (E) Variation of information between the anatomical division of the cells, and the detected communities. (F) Adjusted Rand index between the anatomical division, and the detected communities.	71
352	4.1 Figures showing the over-dispersion possible for a beta-binomial distribution relative to a binomial distribution. Parameters are shown in the captions. . .	82
354	4.2 Figures showing (A) the under-dispersion and (B) over-dispersion permitted by the COMb distribution relative to a binomial distribution. (C) illustrates that the p parameter of the COMb distribution does not correspond to the mean of the distribution, as it does for the binomial and beta-binomial distributions. (D) shows a heatmap for the value of the Kullback-Liebler divergence between the COMb distribution and the standard binomial distribution with same value for n , as a function of p and ν . Parameters are shown in the captions.	85
362	4.3 (A) Raster plot showing the spikes fired by 33 randomly chosen neurons in the primary visual cortex. (B-C) (B) average and (C) variance of the number of active neurons, measured using a sliding window 100ms wide, split into 100 bins. The midpoint of the time interval for each window is used as the timepoint (x-axis point) for the measurements using that window. The grey shaded area indicates the presence of a visual stimulus. The opaque line is an average across the 160 trials that included a visual stimulus of any kind. We can see a transient increase in the average number of active neurons and the variance of this number, followed by a fluctuation and another increase. .	88

371	4.4 (A) Raster plot showing the spikes fired by 33 randomly chosen neurons in	
372	the hippocampus. (B-C) (B) average and (C) variance of the number of active	
373	neurons, measured using a sliding window 100ms wide, split into 100 bins.	
374	The midpoint of the time interval for each window is used as the timepoint (x-	
375	axis point) for the measurements using that window. The grey shaded area	
376	indicates the presence of a visual stimulus. The opaque line is an average	
377	across the 160 trials that included a visual stimulus of any kind. We can see	
378	a transient increase in the average number of active neurons and the variance	
379	of this number at stimulus onset.	89
380	4.5 (A) Raster plot showing the spikes fired by 33 randomly chosen neurons in	
381	the thalamus. (B-C) (B) average and (C) variance of the number of active	
382	neurons, measured using a sliding window 100ms wide, split into 100 bins.	
383	The midpoint of the time interval for each window is used as the timepoint (x-	
384	axis point) for the measurements using that window. The grey shaded area	
385	indicates the presence of a visual stimulus. The opaque line is an average	
386	across the 160 trials that included a visual stimulus of any kind. We can	
387	see an immediate increase at stimulus onset, a subsequent fall, and another	
388	sustained increase until the stimulus presentation ends.	90
389	4.6 (A) An example of the binomial, beta-binomial, and Conway-Maxwell-binomial	
390	distributions fitted to a sample of neural activity. The Conway-Maxwell-	
391	binomial distribution is the best fit in this case. The histogram shows the	
392	empirical distribution of the sample. The probability mass function of each	
393	distribution is indicated by a different coloured line. (B) Across all samples	
394	in all trials, the proportion of samples for which each fitted distribution was	
395	the best fit. The Conway-Maxwell-binomial distribution was the best fit	
396	for 93% of the samples taken from V1 using a bin width of 1ms.	91

397	4.7 (A) We fit a Conway-Maxwell-binomial distribution to the number of active	
398	neurons in 1ms time bins of a 100ms sliding window. We did this for all	
399	trials with a visual stimulus and took the average across those trials. We see	
400	a transient drop in value for the distribution's ν parameter at stimulus onset.	
401	This shows an increase in positive association between the neurons. (B) We	
402	measured the correlation coefficient between the spike counts of all possible	
403	pairs of neurons in the same sliding window. The took the average of those	
404	coefficients. We also did this for every visually stimulated trial, and took the	
405	average across trials. The increase in positive association is not reflected with	
406	an increase in average correlation.	93
407	4.8 (A) The mean Fano factor of the spike counts of the cells in the primary visual	
408	cortex. Means were taken across cells first, then across trials. There was a	
409	significant decrease in the Fano factors immediately after stimulus onset. (B)	
410	The mean Fano factor of the spike counts of the cells in the motor cortex. No	
411	significant change in measurements at any point.	94

412 List of Tables

413	2.1	Fixed parameters A table of the parameters fixed before optimising the model. The values of these parameters could be changed to model different fluorescent calcium indicators.	17
414	4.1	Details of the different bin width and analysis window sizes used when binning spike times, and analysing those data.	79
415	4.2	Relative dispersion of the COMb distribution, and association between Bernoulli variables as represented by the value of the ν parameter.	84
416	4.3	Proportion of samples for which each distribution was the best fit, grouped by bin width. The COMb distribution is the best fit most of the time.	92
417			
418			
419			
420			
421			

422 **List of Abbreviations**

COMb Conway-Maxwell-binomial (distribution)

OASIS Online active set method to infer spikes

SNR Signal to noise ratio

⁴²³

List of Symbols

$[Ca^{2+}]$	Free calcium concentration	mol
$[BCa]$	Fluorescent indicator bound calcium	mol
$[ECa]$	Endogenous mobile buffer bound calcium	mol
$[ImCa]$	Immobile mobile buffer bound calcium	mol
$[BCa^*]$	excited fluorescent indicator bound calcium	mol
k_{X_f}	binding (affinity) rate	$mol^{-1} s^{-1}$
k_{X_b}	unbinding (dissociation) rate	s^{-1}

424 **Chapter 1**

425 **Introduction**

426 **1.1 Overview**

427 Since Hodgkin and Huxley's squid experiments featuring a single axon (Hodgkin and Hux-
428 ley, 1939), to more recent research with spike sorted data from ~ 24000 neurons from 34
429 brain regions from 21 mice (Allen et al., 2019), the number of neurons contributing to elec-
430 trophysiological datasets has been growing. The number of simultaneously recorded neurons
431 has doubled approximately every seven years since the use of multi-electrode recording in
432 neuroscience began (Stevenson and Kording, 2011). Recording methods using two-photon
433 calcium imaging have also been used to extract data from populations containing over 10000
434 neurons (Peron et al., 2015). This dramatic growth in the number of neurons available for
435 analysis requires a dramatic change in analysis methods.

436 There are multiple methods for reading activity from neuronal ensembles: electrophysiolog-
437 ical, calcium imaging, and voltage imaging. Electrophysiology involves inserting electrodes
438 into the brain of an animal. The electrodes read extra-cellular membrane potential, and using
439 these readings we observe activity in the ensemble. Calcium imaging and voltage imaging
440 use indicator dyes or fluorescent proteins that emit fluorescence traces that indicate either
441 the concentration of calcium in a neuron's cytoplasm, or the neuron's membrane potential.
442 In this project, we have attempted to address some of the difficulties in collecting data from
443 these large ensembles using fluorescent calcium indicators, and some of the difficulties in
444 analysing the collected data.

445 The rest of this introductory chapter will give some background about methods of record-
446 ing from the brain, and some background for the rest of the document. Chapter two describes
447 a biophysical model for the fluorescence trace induced by a given spike train in a cell con-
448 taining a fluorescent calcium indicator. Our third chapter describes our investigations into

449 the correlated activity across different regions of a mouse behaving spontaneously. We ap-
450 plied a novel community detection method (Humphries et al., 2019) from network science
451 to correlation based networks of neurons, and observed differences in the structure of these
452 correlations at different timescales. In our fourth chapter, we detail a new statistical model
453 for the number of neurons spiking in a neuronal ensemble at any given moment. With this
454 model, we attempted to capture correlated activity in a new way. The fifth chapter is a brief
455 description of the work that yielded negative results or was abandoned. The final chapter is a
456 discussion of our work and results from the previous chapters and their implications.

457 1.2 Modelling the fluorescence of calcium indicators

458 To focus on calcium imaging for a start, a neuron that contains a fluorescent calcium indicator
459 in its cytoplasm will fluoresce when bombarded with photons. The amount that the cell
460 will fluoresce is dependent on the concentration of fluorescent indicator within the cell, and
461 the concentration of calcium within the cell. When a neuron fires an action potential, the
462 influx of free calcium ions causes an increase in fluorescence when those ions bond with the
463 fluorescent indicator and those bounded molecules are bombarded with photons. After the
464 action potential, as calcium is extruded from the cell the fluorescence returns to a baseline
465 level. This is the basic mechanism of fluorescent calcium indicator based imaging.

466 This method has some advantages over electrophysiology as measure of neuronal ensem-
467 ble activity. Many of the problems with electrophysiology are within the processes used to
468 isolate spikes in the extracellular voltage readings, and assign these spikes to individual cells.
469 These processes are collectively called ‘spike sorting’. A comparison of many different spike
470 sorting algorithms found that these algorithms only agreed on a fraction of cases (Buccino
471 et al., 2019). Furthermore, because electrodes measure extracellular voltage, neurons that do
472 not spike will not be detected. Isolating individual neurons is easier and more reliable when
473 using calcium imaging data, because cells will emit a baseline level of fluorescence when not
474 firing action potentials. Another advantage is that calcium imaging sites can be re-used for
475 weeks for longitudinal studies (Chen et al., 2013). One of the methods of delivering the flu-
476 orescent indicator is by adeno-associated viruses, consequently there can be problems with
477 indicator gradients around the infection site, and expression levels will change in individual
478 cells over weeks (Tian et al., 2009; Chen et al., 2013). This delivery method can also cause
479 cell pathology, and nuclear filling (Zariwala et al., 2012), but these problems can be solved by
480 using lines of transgenic mice (Dana et al., 2014). The fluorescence signal itself can serve a a

481 good indicator of cell activity, but similarly to electrophysiology, the aim of calcium imaging
482 is often spike detection.

483 If the imaging data is collected at a high enough frequency, and the signal-to-noise ratio
484 of the fluorescence trace is high enough, it should be possible to infer the spike times to some
485 level of accuracy. For example, the calmodulin based indicator GCaMP6s has a sufficiently
486 high signal-to-noise ratio that isolated action potentials can be detected and inferred (Chen
487 et al., 2013). Many spike inference algorithms exist (Vogelstein et al., 2010; Pnevmatikakis
488 et al., 2016; Friedrich and Paninski, 2016; Pnevmatikakis et al., 2013; Pnevmatikakis et al.,
489 2014; Deneux et al., 2016; Greenberg et al., 2018), and some of these can perform both cell
490 isolation and spike detection simultaneously (Vogelstein et al., 2010; Pnevmatikakis et al.,
491 2016; Pnevmatikakis et al., 2014; Deneux et al., 2016). But the relationship between spik-
492 ing and fluorescence change is not fully understood. For example, the fluorescent indicator
493 will act like an additional calcium buffer within the cell cytoplasm and will compete with
494 the other endogenous buffers to bind with free calcium ions. Therefore, the concentration
495 of those endogenous buffers, and the binding dynamics of those buffers will have an effect
496 on the change in fluorescence in response to an action potential. Furthermore, the binding
497 dynamics of the fluorescent indicator itself will have an effect on the change in fluorescence.
498 For example, the GCaMP series of fluorescence indicators are based on the calcium buffer
499 protein calmodulin. This protein has four binding sites, whose affinities interact non-linearly.
500 But most of the spike inference algorithms model the fluorescence as a linear function of
501 a calcium trace, and they model this calcium trace as a first or second order autoregression
502 with a pulse input to represent action potentials. Deneux et al. (2016) developed two dif-
503 ferent calcium fluorescence models behind their spike inference algorithm (MLspike) with a
504 more biological inspiration. For their simpler model, they take a physiological approach and
505 account for baseline calcium indicator dynamics. They end up with a system of first order
506 differential equations defining the dynamics of calcium concentration, baseline fluorescence,
507 and fluorescence. For their more complicated model specifically for genetically encoded cal-
508 cium indicators, they also took into account indicator binding and unbinding rates, which
509 added another equation to their system of equations. The algorithms that use the autore-
510 gression model and the MLspike algorithm are outperformed by the most recently published
511 spike inference algorithm (Greenberg et al., 2018). This algorithm takes into account the
512 binding dynamics of both the endogenous buffers and fluorescent calcium indicator, and the
513 concentrations of free calcium, indicator, and endogenous buffer within the cell cytoplasm.
514 The performance of this algorithm shows that there is value in more biologically inspired

515 models of fluorescent calcium indicators.

516 In light of the growing popularity of two-photon calcium imaging, and the lack of biolog-
517 ically inspired spike inference algorithms (Greenberg et al. developed their spike inference
518 algorithm in parallel to our work), we decided to develop a biologically inspired model for
519 fluorescent calcium indicator fluorescence. The idea being that our model would take a spike
520 train, or simply spike times, provided by the user, and return the fluorescence trace that would
521 be induced by this spike train or spike times. The model contains parameters for concentra-
522 tions of indicator and endogenous buffers, as well as affinity and unbinding rates for these
523 buffers. There are also parameters for the baseline concentration of free calcium in the cell
524 cytoplasm, and the cell radius (as a means for calculating the cell volume). With this model,
525 we hoped that experimentalists would be able to test out different calcium indicators on the
526 types of spike trains that they expect to encounter. This way they could decide ahead of time
527 which indicator suited their situation best. Since the output of our model is a fluorescence
528 trace, the spike inference models mentioned above can be applied to the modelled fluores-
529 cence. This means that the model could also be used to benchmark the performance of these
530 spike inference algorithms, and to investigate the impact of variations in the model on spike
531 inference accuracy.

532 1.3 Functional networks

533 We have outlined some of the advantages that calcium imaging has over electrophysiology.
534 But electrophysiology is more useful in some situations. One particular drawback for two-
535 photon calcium imaging is that usually it can only be used for imaging near to the surface
536 of the brain. This problem can be solved by removing the tissue around the area to be im-
537 aged, and custom building a two-photon microscope Dombeck et al., 2010. Imaging with
538 three (or presumably more) photons may solve this problem in the future (Ouzounov et al.,
539 2017). A better option for reading activity from neurons beyond the surface of the brain is to
540 use Neuropixels probes (Jun et al., 2017). These probes can be used to read from thousands
541 of neurons simultaneously in many different areas of the brain (Allen et al., 2019; Stringer
542 et al., 2019; Steinmetz, Carandini, and Harris, 2019; Steinmetz et al., 2019). This brings us
543 to another problem for which we require new innovations in our analysis methods. Specif-
544 ically, analysing correlated behaviour in neural ensembles consisting of neurons from many
545 different brain regions.

546 Until the invention of new technologies such as the Neuropixels probes, most elec-
547 trophysiology datasets read from neurons in only one or two regions. Therefore most of
548 the research on interactions between neurons in different regions is limited to two regions
549 (Wierzynski et al., 2009; Patterson et al., 2014; Girard, Hupé, and Bullier, 2001). In chapters
550 3 and 4 we used datasets with neurons from 9 and 5 different brain regions respectively. In
551 their review of the interaction between growing the number of neurons in datasets and the
552 analysis methods applied to those dataset, Stevenson and Kording (2011) assert that an im-
553 portant objective of computational neuroscience is to find order in these kinds multi-neuron
554 of datasets. This was our main aim for the research described in chapter 3.

555 In light of recent findings based on correlated behaviour showing that spontaneous be-
556 haviours explain activity in many different parts of the brain that would otherwise be regarded
557 as noise (Stringer et al., 2019), that satiety is represented brain wide (Allen et al., 2019), and
558 that exploratory and non-exploratory states are represented in the amygdala (Gründemann
559 et al., 2019), it was clear that state representation or motor control had an influence on cor-
560 related behaviour in areas of the brain not usually associated with these tasks. Also, given
561 differences in timescales of fluctuations in different brain regions (Murray et al., 2014), and
562 different timescales for event representation in different brain regions (Baldassano et al.,
563 2017), we decided to investigate brain wide correlated behaviour at timescales ranging from
564 5ms up to 3s.

565 We started off measuring the correlations in spike counts between individual neurons in
566 our ensemble. These measurements induced a weighted undirected graph where each node
567 represented a neuron, and the weight of each edge was the strength of the correlation be-
568 tween the neurons represented by the nodes at either end of that edge. In order to put the
569 neurons into groups with correlated behaviour, we applied a novel community detection al-
570 gorithm (Humphries et al., 2019) to this graph. We repeated this analysis for timescales
571 from milliseconds to seconds. Bear in mind that our correlation based graph was completely
572 agnostic of the anatomical regions in which our cells resided. We then compared our corre-
573 lated communities to their anatomy at each timescale. In this way, we used a novel method,
574 never applied neuronal data before, to analyse the makeup of correlated communities across
575 different regions at different timescales.

576 1.4 A new statistical model for capturing correlated behaviour

577 Many important findings have been made by measuring the correlations between binned
 578 spike counts, but there are some problems with this method of analysis. Firstly, the width
 579 of the bins used to bin spike times into spike counts has an effect on the magnitude of the
 580 correlations measured. Using a short bin width can cause your measurements to be artificially
 581 small (Cohen and Kohn, 2011). This may not be an issue if one is considering relative size of
 582 correlations when using the same bin width, but it is still not ideal. Secondly, while pairwise
 583 correlations can capture most of the information in a small network (up to 40 cells) of highly
 584 correlated cells (Schneidman et al., 2006), a model based on pairwise correlations alone will
 585 fail to capture the activity of larger (~ 100 cells) networks, higher order correlated activity
 586 is required (Ganmor, Segev, and Schneidman, 2011). One problem with these higher order
 587 correlations is that they may be defined in different ways (Staude, Grün, and Rotter, 2010).
 588 Furthermore if we want to include them in a model this usually involves greatly increasing the
 589 number of parameters to fit, which increases the dimension of the parameter space leading
 590 to the ‘curse of dimensionality’. Some models attempt to sidestep these problems while
 591 still capturing higher-order correlations. These models attempt to capture the relationship
 592 between each individual neuron in the ensemble, and the ensemble as a whole. Okun et al
 593 (2015) called the strength of this relationship the ‘population coupling’, and demonstrated
 594 that this quantity can predict an individual neuron’s response to optogenetic stimulation of
 595 the whole ensemble. They also showed that this quantity was an indicator of the neuron’s
 596 synaptic connectivity (Okun et al., 2015). With the ‘population tracking model’, O’Donnell
 597 et al. (2016) linked the probability of firing an action potential for each individual neuron
 598 with the distribution of the number of active neurons. This allowed model fitting for a large
 599 number of neurons, as well as calculation of full pattern probabilities, and population entropy
 600 (O’Donnell et al., 2017).

601 In this work, we also aimed to capture correlated behaviour between the neurons in a
 602 neuronal ensemble without measuring correlations directly. Correlation coefficients capture
 603 the linear component of the relationship between two random variables, but will not mea-
 604 sure any relationship beyond linearity. Also, measuring correlation coefficients using short
 605 timebins can be difficult for neuronal data (Cohen and Kohn, 2011). We decided to abandon
 606 correlation, and we aimed to quantify a more general concept of association by modelling
 607 the number of active neurons in the ensemble using a Conway-Maxwell-binomial (COMb)
 608 distribution (Kadane, 2016).

609 The COMb distribution is a probability distribution over the number of successes in a
610 sequence of Bernoulli trials, where these trials can be associated in some way. The COMb
611 distribution is an extension of the standard binomial distribution, with an additional parameter
612 to model association between the Bernoulli variables. Using this additional parameter the
613 distribution can capture positive association, where the Bernoulli variables tend to take the
614 same value, negative association, where the Bernoulli variables tend to take opposite values,
615 or no association i.e. the standard binomial distribution.

616 We fit a COMb distribution to spike sorted electrophysiological data taken from five
617 different regions in the brain of an awake mouse exposed to visual stimuli (Steinmetz et al.,
618 2019). We examined whether or not a model based on the COMb distribution was able to
619 capture changes in the number of active neurons in these neuronal ensembles in response to
620 the stimuli. We also investigated the relationship between the changes as captured by the
621 COMb model and the change in neural variability as measured by Churchland et al. in their
622 famous paper (Churchland et al., 2010).

623 Our overall aim was to investigate some of the challenges in analysing large ensembles
624 of neurons present today. That included collecting the data to analyse (via calcium imaging),
625 and subsequently analysing these data. We felt that this was a worthwhile project because
626 the size of datasets, in terms of numbers of neurons and data collected, is growing rapidly.
627 Consequently these challenges will only become greater unless they are addressed. This is
628 our attempt at addressing them.

629 **Chapter 2**

630 **Sensitivity of the**
631 **spikes-to-fluorescence transform to**
632 **calcium indicator and neuron**
633 **properties**

634 *Abstract*

635 Fluorescent calcium indicators such as GCaMP are widely used to monitor neuronal activity.
636 However the relationship between the fluorescence signal and the underlying action potential
637 firing is poorly understood. This lack of knowledge makes it difficult for experimenters
638 to decide between different indicator variants for a given application. We addressed this
639 problem by studying a basic biophysical model of calcium dynamics in neuronal soma. We
640 fit the model parameters to publicly available data where GCaMP6s fluorescence and whole-
641 cell electrophysiological recordings were made simultaneously in the same single neurons.
642 We systematically varied the model's parameters to characterise the sensitivity of spike train
643 inference algorithms to the calcium indicator's main biophysical properties: binding rate,
644 dissociation rate, and molecular concentration. This model should have two potential uses:
645 experimental researchers may use it to help them select the optimal indicator for their desired
646 experiment; and computational researchers may use it to generate simulated data to aid design
647 of spike inference algorithms.

648 **2.1 Introduction**

649 Although fluorescent calcium indicators such as GCaMP are widely used to monitor neuronal
650 activity, the relationship between the fluorescence signal and the underlying action potential
651 firing is imperfect. The fluorescence signal has a low signal-to-noise ratio, and most indica-
652 tors' kinetics are slow relative to the millisecond-timescale dynamics of the membrane volt-
653 age (example in figure 2.1A). This makes spike inference difficult. Furthermore, the effects
654 of the indicator and cell properties on the fluorescence signal are unknown. For example,
655 genetically encoded indicators can accumulate within neurons over weeks and months (Chen
656 et al., 2013). Studies using calcium-sensitive fluorescent dyes have shown that indicator con-
657 centration has substantial effects on the spike-to-fluorescence relationship (Maravall et al.,
658 2000). Therefore spike rates inferred from GCaMP fluorescence signals may give mislead-
659 ing results if comparing across imaging sessions. More generally, the poor understanding of
660 the spike-to-fluorescence transform means experimenters may not know whether to trust the
661 outputs of spike train inference methods in any given application.

662 Spike trains are usually inferred from the time series of intensity values of one pixel of the
663 fluorescence image, where the pixel is located at the cell's soma. The problems of identifying
664 these pixels, and inferring spikes from their time series can solved separately or together.
665 When attempting to infer spikes, the fluorescence trace is modelled as a linear combination of
666 calcium concentration dynamics, a baseline calcium concentration, and some Gaussian noise.
667 The calcium concentration dynamics are modelled as an autoregressive process of degree 1
668 or 2 with a pulse input corresponding to the spike train, or the number of spikes fired in a
669 time step. The model includes no dynamics for the fluorescent indicator itself. Furthermore,
670 in order to make this model into an easily solvable linear programming problem the number
671 of spikes fired in a timestep is not restricted to non-negative integers but to arbitrary non-
672 negative values (Vogelstein et al., 2010; Pnevmatikakis et al., 2016; Friedrich and Paninski,
673 2016; Pnevmatikakis et al., 2013; Pnevmatikakis et al., 2014). More biologically inspired
674 spike inference models do exist (Deneux et al., 2016), but their fundamentals are very similar.
675 In this work, we investigated the effect of changing dynamics and buffer concentrations on
676 the accuracy of the inference algorithms based on these models.

677 The aim of this project was to model the fluorescence traces produced by a fluorescent
678 calcium indicator in a neuron soma resulting from a specific spike train, given calcium indi-
679 cator parameters such as binding rate, dissociation rate, and molecular concentration. Such

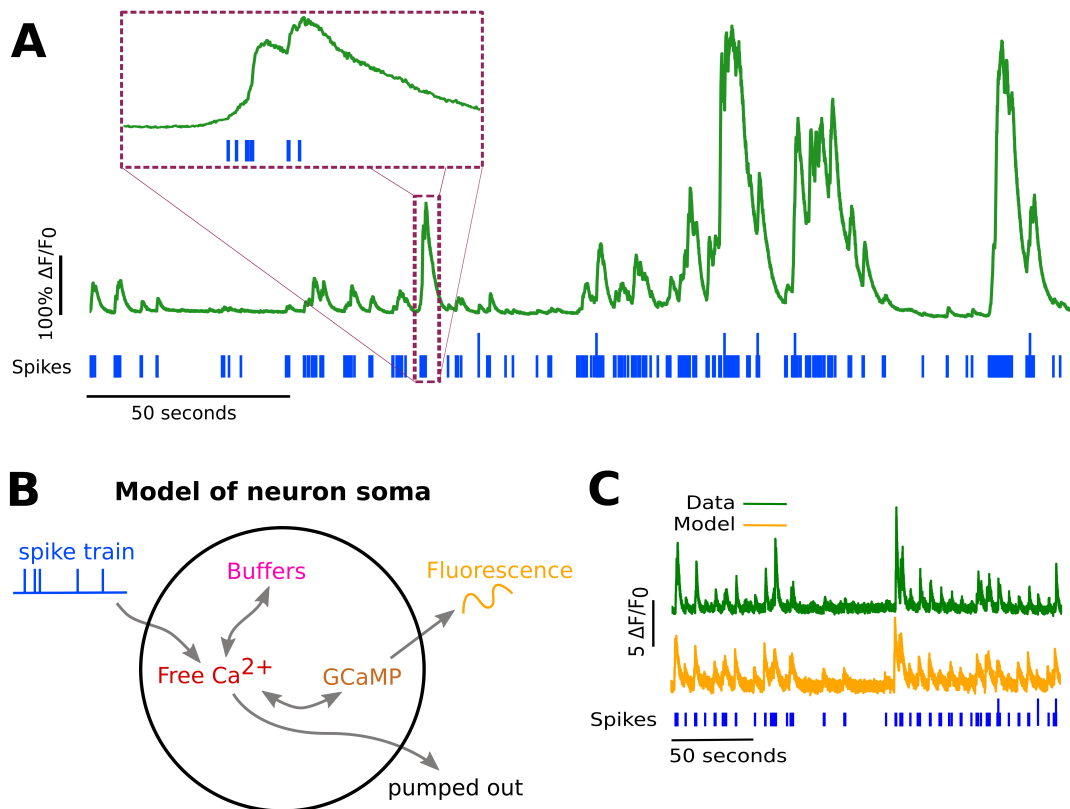


FIGURE 2.1:

A: Example spike train (blue) and the corresponding GCaMP6s fluorescence trace (green), data replotted from (Berens et al., 2018). Inset shows zoomed section of traces to highlight slow decay of GCaMP6s fluorescence relative to spike time intervals.

B: Schematic diagram of the neuron calcium and GCaMP computational model.

C: Good visual match of data fluorescence trace (green) and model simulated fluorescence (orange) in response to an identical spike train (blue).

680 a model would allow benchmarking of various spike inference algorithms, and enable under-
681 standing of how indicator characteristics affect the quality of spike train inference.

682 The model we developed consisted of free calcium, fluorescent indicator molecules, and
683 mobile and immobile endogenous calcium buffers. The indicator molecules which were
684 bound to a calcium molecule could be either excited, i.e. able to release a photon, or relaxed.
685 In order to reproduce the noise inherent in the data collection, we modelled the release of
686 photons from the excited indicator bound calcium as a stochastic process.

687 The fluorescence traces produced by the simulation were calibrated to reproduce the
688 signal-to-noise ratio observed in experimental data. Previously published spike inference
689 algorithms were then used to infer spike trains from the experimental fluorescence traces and
690 the modelled fluorescence traces. The parameters of the model were then varied in order to
691 determine the effect on the system dynamics and the effects on spike inference.

692 2.2 Methods

693 2.2.1 Calcium dynamics model

694 We wrote a biophysical model of the calcium dynamics within a cell soma. When a neuron
695 fires an action potential, voltage-dependent calcium ion-channels open up that allow a current
696 of calcium ions (Ca^{2+}) to flow into the neuron (Koch, 1999). The increase in the free calcium
697 ion concentration inside of the cell, along with changes in the concentration of potassium
698 and sodium, causes the change in cell membrane potential, which must be depolarised. The
699 depolarising process consists of free calcium ions leaving the cell through open ion channels,
700 or binding to molecules within the cell called buffers, or calcium storage by organelles such
701 as the endoplasmic reticulum. A diagram illustrating the cell, its channels, and its buffers
702 can be seen in figure 2.1A. There are several different types of calcium buffer, each with
703 different dynamics and different concentrations within different types of excitable cell. The
704 fluorescent calcium indicator is another calcium buffer, with the useful property that when it
705 is bound to a calcium ion, the bound molecule may become excited by a photon and release
706 a photon in return. This is what creates the fluorescence. After the action potential has taken
707 place, the free calcium concentration within the cell will return to a baseline level (Maravall
708 et al., 2000).

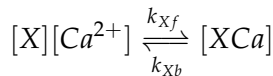
709 We modelled the the dynamics of five molecular concentrations,

- 710 • Free calcium ion concentration, $[\text{Ca}^{2+}]$

2.2. Methods

- 711 • Fluorescent indicator bound calcium, $[BCa]$
 712 • Endogenous mobile buffer bound calcium, $[ECa]$
 713 • Endogenous immobile buffer bound calcium, $[ImCa]$
 714 • Excited buffered calcium, $[BCa^*]$

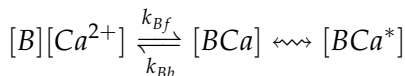
The term ‘buffering’ refers to free calcium ions coming into contact with buffer molecules followed by the binding of those molecules. Diagrammatically:



715 where $[X]$ represents any buffer molecule, and k_{X_f} and k_{X_b} represent the binding (affinity)
 716 and unbinding (dissociation) rates in units of per molar concentration per second ($M^{-1} s^{-1}$)
 717 and per second (s^{-1}) respectively. The speed of this chemical reaction is determined by the
 718 binding and unbinding rates.

719 There are a number different endogenous buffers in any neuron. Which buffers are
 720 present, and the buffers’ concentrations vary from cell to cell. In order to capture the ef-
 721 fects of mobile and immobile endogenous buffers without introducing several parameters,
 722 they were modelled as two buffers. One representing mobile buffers and the other represent-
 723 ing immobile buffers. Each with their own binding and unbinding rates.

The fluorescent calcium indicator behaves similarly to the other calcium buffers. The calcium is buffered by the indicator in the same way. But an indicator bound calcium molecule can become excited by absorbing the energy from a photon. An excited indicator bound calcium molecule can then release a photon to go back to its ‘relaxed’ state.



724 The released photons are captured by a photon collector. This gives us the fluorescence trace.
 725 Ignoring the baseline level of free calcium in a neuron, the system of equations we used
 726 to model all of these interactions is as follows:

$$\begin{aligned} \frac{d[Ca^{2+}]}{dt} = & k_{Bb}[BCa] + k_{Eb}[ECa] + k_{Imb}[ImCa] \\ & - k_{Bf}[B][Ca^{2+}] - k_{Ef}[E][Ca^{2+}] - k_{Imf}[Im][Ca^{2+}] \\ & + \beta([Ca_0^{2+}] - [Ca^{2+}]) \end{aligned} \quad (2.1)$$

$$\frac{d[BCa]}{dt} = k_{Bf}[B][Ca^{2+}] - k_{Bb}[BCa] + r[BCa^*] - e[BCa] \quad (2.2)$$

$$\frac{d[ECa]}{dt} = k_{Ef}[E][Ca^{2+}] - k_{Eb}[ECa] \quad (2.3)$$

$$\frac{d[ImCa]}{dt} = k_{Imf}[Im][Ca^{2+}] - k_{Imb}[ImCa] \quad (2.4)$$

$$\frac{d[BCa^*]}{dt} = \eta[BCa] - r[BCa^*] \quad (2.5)$$

727 where $[Ca_0^{2+}]$ is the baseline calcium concentration within the cell soma, β is a rate defining
728 how quickly free calcium enters or leaves the cell in the absence of an action potential, η
729 is the excitation rate for indicator bound calcium, r is the photon release rate for the excited
730 indicator bound calcium, and f and b are used to indicate the forward and backward rates
731 for chemical reactions respectively. The excitation rate defines the proportion of indicator
732 bound calcium that becomes excited at each time step. The photon release rate defines the
733 proportion of excited indicator bound calcium that releases a photon and returns to its relaxed
734 state at each time step. An action potential is modelled as a discontinuous increase in the free
735 calcium concentration to an appropriate value (Maravall et al., 2000).

736 Note that each of the three pairs of binding and unbinding terms in the first equation has a
737 corresponding pair in one of the subsequent three equations. Binding removes a free calcium
738 molecule and adds a bound calcium molecule, and unbinding does the opposite.

739 When using this model to simulate a fluorescence trace, the system of equations above are
740 first solved over a period of 25s without action potentials. This lets each of the five tracked
741 chemical concentrations reach their steady state. Then we use the given spike train and the
742 parameters to model the fluorescence trace.

743 Note that since the model has no spatial component, the mobile and immobile buffers
744 only differ in their binding and unbinding rates.

745 Photon release & capture

746 We used a simple model for the photon release. The number of photons released at each time
747 step was controlled by the number of excited indicator bound calcium molecules in the cell
748 and a parameter called the ‘release rate’. The release rate is an optimised free parameter of
749 the model.

750 As for the photon capture, in two-photon excitation microscopy the photons scattered
751 by the fluorescent indicator get scattered in all directions. Therefore the number of photons
752 detected is stochastic. This made the process for capturing photons the natural source of
753 noise in the system. The number of photons captured, and therefore the intensity of the

2.2. Methods

754 fluorescence, is modelled using a binomial distribution. The number of photons released was
755 used as the number of trials. The probability of success, or ‘capture rate’ was a free parameter
756 of the model that we optimised.

757 2.2.2 Parameter optimisation

758 The free parameters of the model are as follows:

759 **Calcium rate, β** Controls how quickly the concentration of free calcium will be driven to
760 the baseline concentration.

761 **Capture rate, p** The average proportion of photons captured by the photon detector.

762 **Excitation rate, η** The number of indicator bound calcium molecules that become excited
763 by photon bombardment at each time step.

764 **Release rate, r** The number of excited indicator bound calcium molecules that release a
765 photon at each time step.

766 To optimise the free parameters given a fluorescence trace, we applied the following proce-
767 dure:

- 768 1. The frequency power spectrum of the trace was measured.
- 769 2. The power spectrum was smoothed using a boxcar smoother (aka. sliding average, box
770 smoother).
- 771 3. The log of the smoothed power spectrum was measured.
- 772 4. Use the model to create a modelled fluorescence trace.
- 773 5. Apply steps 1, 2, and 3 to the modelled fluorescence trace.
- 774 6. Calculate the root mean squared difference between the log power of the actual fluo-
775 rescence trace, and the log power of the modelled fluorescence trace.
- 776 7. Calculate the root mean squared difference between the actual fluorescence trace and
777 the modelled fluorescence trace.
- 778 8. Use an optimisation algorithm to reapply this process, attempting to minimize the sum
779 of the two root mean squared differences at each iteration.

780 Using the root mean squared difference of the log power spectra as part of the objective
781 function forces the model to match the noise frequency of the actual fluorescence. Using
782 the root mean squared difference of the traces themselves forces the model to match the
783 amplitude of the fluorescence trace more accurately.

784 In order to minimise the objective function, a suite of meta-heuristic optimisation (aka.
785 black-box optimisation) algorithms were implemented on each of the traces in the dataset.
786 These methods were chosen because they don't require a gradient for the objective function
787 (gradient-free) and they are particularly useful for minimising stochastic objective functions
788 like the one we used here. The free parameters were optimised for each individual fluores-
789 cence trace. The most successful method for each trace was recorded. The method that was
790 most often successful was probabilistic descent, and the second most successful method was
791 generating set search. Both of these methods are examples of pattern search. These two
792 methods were the best optimisers on about 75% of the traces in the dataset.

793 Although this optimisation procedure minimises the value of the optimisation function,
794 the value never reaches zero for a number of reasons. Firstly, the fluorescence traces carry
795 low frequency fluctuations that cannot be captured by the model. Secondly, the model as-
796 sumes that the process of calcium binding to the fluorescent indicator is linear in time (see
797 equation 1), but there are more complicated dynamics involved here. Fluorescent calcium
798 indicators, the GCaMP series for example, are often built upon the calcium binding protein
799 called 'calmodulin'. This protein has four calcium binding sites. These sites are locally split
800 into two pairs. Each pair has a different affinity for calcium, and the affinity of the binding
801 sites is affected by the occupancy of the other binding sites (Kilhoffer et al., 1992). So the
802 calcium to calcium indicator binding process is non-linear, but the model does not take this
803 into account.

804 **Fixed parameters**

805 As well as the optimised parameters mentioned in section 2.2.2, the model also has thirteen
806 fixed parameters. Please see table 2.1 for details of these parameters and their values. In
807 an application of the model, these parameters can be changed in order to model any given
808 fluorescent calcium indicator, or even prospective indicators that only exist in theory.

2.2. Methods

Parameter	Description	Value	Source
baseline	The baseline concentration of free calcium within the cell soma	$4.5 \times 10^{-8} M$	(Maravall et al., 2000)
cell radius	The radius of the soma (assumed to be spherical)	$10^{-5} M$	(Fiala and Harris, 1999)
endogenous	The concentration of endogenous mobile buffer within the cell soma	$10^{-4} M$	(Faas et al., 2011)
frequency	The frequency at which the spike trains are sampled.	100Hz	
immobile	The concentration of endogenous immobile buffer within the cell soma	$7.87 \times 10^{-5} M$	(Bartol et al., 2015)
indicator	The concentration of fluorescent indicator within the cell soma	$10^{-4} M$	(Maravall et al., 2000)
k_{Bb}	The unbinding rate of the fluorescent calcium indicator	$160 s^{-1}$	(Bartol et al., 2015)
k_{Bf}	The binding rate of the fluorescent calcium indicator	$7.77 \times 10^8 s^{-1} M^{-1}$	(Bartol et al., 2015)
k_{Eb}	The unbinding rate of the endogenous mobile buffer	$10^4 s^{-1}$	(Bartol et al., 2015)
k_{ef}	The binding rate of the endogenous mobile buffer	$10^8 s^{-1} M^{-1}$	(Bartol et al., 2015)
k_{Imb}	The unbinding rate of the endogenous immobile buffer	$524 s^{-1}$	(Bartol et al., 2015)
k_{Imf}	The binding rate of the endogenous immobile buffer	$2.47 \times 10^8 s^{-1} M^{-1}$	(Bartol et al., 2015)
peak	The increase in free calcium concentration within the cell induced by an action potential	$2.9 \times 10^{-7} M$	(Maravall et al., 2000)

TABLE 2.1: **Fixed parameters** A table of the parameters fixed before optimising the model. The values of these parameters could be changed to model different fluorescent calcium indicators.

809 **2.2.3 Julia**

810 The programming language used to write and execute the model was ‘Julia’. Julia is a dy-
811 namic programming language designed for technical computing. Julia was designed specif-
812 ically to provide a convenient high-level dynamic language similar to MATLAB, or Python,
813 with improved performance. Julia’s type system and Julia’s direct interfaces with C and
814 Fortran allow this aim to be achieved (Bezanson et al., 2012). The Julia version of the
815 ‘Sundials’ package for ODE solving was used to solve the system of equations above. The
816 BlackBoxOptim.jl package for Julia was used to perform the optimisation.

817 **2.2.4 Spike inference**

818 We used spike inference algorithms to compare the quality of spike inference using the mod-
819 eled traces to the quality of spike inference using the observed traces. We also used the
820 spike inference algorithms to assess the effect of parameter perturbation on the spike infer-
821 ence. Three algorithms were used:

822 **Constrained non-negative matrix deconvolution algorithm (aka CNMD algorithm)** The
823 underlying model models the fluorescence as a linear function of a calcium trace with
824 additional noise. This calcium trace is a first order autoregression with a pulse input to
825 represent action potentials. This algorithm uses a constrained version of non-negative
826 Weiner deconvolution to infer a calcium signal and a ‘spiking activity signal’ from the
827 fluorescence trace (Vogelstein et al., 2010; Pnevmatikakis et al., 2016). The spiking ac-
828 tivity signal is a non-negative vector of real numbers reflecting the cell’s activity rather
829 than an actual spike train. We inferred a spike train by choosing an optimised thresh-
830 old for the spiking activity signal. Whenever the spiking activity signal exceeded that
831 threshold, an action potential was inferred. The threshold was optimised by minimis-
832 ing the difference between the number of spikes observed and the number of spikes
833 predicted.

834 **MLSpike algorithm** Deneux et al. (2016) developed two different calcium fluorescence
835 models behind their spike inference algorithm (MLspike) with a more biological in-
836 spiration. For their simpler model, they take a physiological approach and account for
837 baseline calcium indicator dynamics. They end up with a system of first order differen-
838 tial equations defining the dynamics of calcium concentration, baseline fluorescence,
839 and fluorescence. For their more complicated model specifically for genetically en-
840 coded calcium indicators, they also took into account indicator binding and unbinding

2.2. Methods

841 rates, which added another equation to their system of equations. This algorithm uses a
842 generalised version of the Viterbi algorithm to return the spike train that maximises the
843 likelihood of producing the given fluorescence trace. The Viterbi algorithm is an algo-
844 rithm for estimating the most likely sequence of hidden states resulting in a sequence
845 of observed states in a discrete-time finite-state Markov process (Forney, 1973). In this
846 case, each hidden state is defined by the presence or absence of an action potential, and
847 each observed state is the value of the fluorescence trace at each time step. (Deneux
848 et al., 2016).

849 **Online Active Set method to Infer Spikes (OASIS)** This algorithm is once again based on
850 an auto-regressive model of the fluorescence trace, but can be generalised to any or-
851 der. Both the first and second order versions can be fit to a spike train in a reasonable
852 time. The algorithm itself is a generalisation of the pool adjacent violators algorithm
853 (PAVA) that is used in isotonic regression. The OASIS algorithm works through the
854 fluorescence trace from beginning to end, this combined with the speed of the algo-
855 rithm means that it could be used for real-time online spike inference (Friedrich and
856 Paninski, 2016). Given a fluorescence trace, the algorithm will return the most likely
857 spike train and an inferred denoised fluorescence signal.

858 In order to quantify the quality of spike inference for a given algorithm, we ran that algorithm
859 on all of the fluorescence traces in dataset number eight of the spike finder datasets. Then we
860 measured some binary classification measures on the results. These measures included

- 861 ● Accuracy
- 862 ● True positive rate (aka recall, sensitivity, hit rate)
- 863 ● True negative rate (aka specificity)
- 864 ● Precision
- 865 ● Negative predicted value
- 866 ● False negative rate (aka miss rate)
- 867 ● False positive rate (aka fall-out)
- 868 ● False discovery rate
- 869 ● False omission rate

870 In making these measurements, we allowed a tolerance of two subsequent time bins for spike
871 prediction. For example, the spike train data is a vector of 0s and 1s, with one element for
872 each time bin. A ‘0’ denotes inactivity, a ‘1’ denotes the presence of at least one action
873 potential. The inferred spike trains produced by the spike inference algorithms take the same
874 form. In our analysis, if a spike appeared in the inferred spike train up to two time frames
875 after a spike in the observed spike train, that spike was considered correctly inferred i.e. a
876 true positive. However, once a spike in the inferred spike train was matched to a spike from
877 the observed spike train, the inferred spike could not be matched to another observed spike.
878 To illustrate, if two spikes were inferred in the two time bins following an isolated observed
879 spike, the first inferred spike was considered correctly inferred, but the second inferred spike
880 was considered incorrectly inferred, i.e. a false positive.

881 The most useful measure was the true positive rate. This is because the spiking is sparse
882 and this measurement is sensitive to the number of spikes observed and inferred, but is not
883 affected by the true negative or false negative rates. After optimising the parameters for each
884 fluorescence trace we measured the spike inference quality for the observed fluorescence
885 traces, and compared this to the spike inference quality for the modelled traces.

886 When measuring the spike inference quality for higher frequency spike train (1 – 10Hz),
887 we used the accuracy as our binary classification measure. At these frequencies the variance
888 of the fluorescence trace was much higher than for sparser spiking regimes, therefore we
889 wanted to take into account the number of false negatives inferred by the algorithm.

890 **Comparing spike inference quality**

891 In order to compare spike inference quality we had to use methods for comparing samples.
892 When comparing the true positive rate distributions arising from two different datasets, or
893 two different algorithms on the same dataset, we compared the distributions using a paired
894 t-test.

895 **2.2.5 Perturbation analysis**

896 In order to measure the sensitivity of spike inference to changes in a given model parameter,
897 we perturbed the parameter and compared the quality of spike inference with the perturbed
898 parameters to the quality of spike inference with the experimental or optimised parameters.
899 In order to maximise the possibility of observing a difference due to the perturbation, we
900 perturbed the chosen parameter by a relatively large amount. For example, the experimen-
901 tal value for the molar concentration of the fluorescent indicator within the cell was $10^{-4}M$

2.3. Results

902 (Maravall et al., 2000). The perturbed values used for this parameter were $10^{-2}M$, $10^{-3}M$,
903 $10^{-5}M$, and $10^{-6}M$. The quality of the inference was compared by measuring the true posi-
904 tive rate for each perturbed value and using a t-test to compare the distributions of the results.

905 This analysis was performed firstly without any optimisation of the free parameters for
906 use with the perturbed parameters. Then the analysis was performed after the optimised
907 parameters for each perturbed value were calculated.

908 2.2.6 Signal-to-noise ratio

909 To assess the effect of perturbation on the modelled traces, we measured and compared the
910 signal to noise ratio (SNR) on each of the modelled traces. We calculated the SNR as the
911 peak change in fluorescence divided by the standard deviation of the baseline fluctuation of
912 the fluorescence trace (Tada et al., 2014). We measured these values by running the model
913 on a spike train consisting a long period of inactivity followed by one action potential. We
914 ran the model on this spike train one hundred times. We then measured the mean change
915 in fluorescence and standard deviation of baseline activity across the one hundred modelled
916 fluorescence traces, and calculated the SNR.

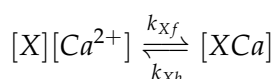
917 2.2.7 Data sources

918 All of the data used in this project was sourced from the ‘Spike Finder’ project (spikefinder.codeneuro.org).
919 The data consisted of a collection of datasets with simultaneously measured fluorescence
920 traces and action potentials (Berens et al., 2018).

921 2.3 Results

922 2.3.1 A biophysical computational model can generate accurate fluorescence 923 traces from spike trains

To study the relationship between action potential firing and calcium fluorescence, we built a computational model of calcium dynamics in a neuronal soma. The model consisted of four dynamic variables: the concentration of free calcium, two types of endogenous buffer, and the calcium-sensitive fluorescent indicator. Each of the buffers and the indicator could independently bind and unbind with calcium. These reactions were modelled as



where X is the buffer concentration and Ca^{2+} is the calcium concentration. Each species could therefore exist in two states: either bound with calcium or unbound. To model the imaging process, we also added a third, excited state to the indicator. When in the calcium-bound state, the indicator could be converted to an excited state, corresponding to the absorption of a photon. The rate of this excitation process could be interpreted as the intensity of the light illuminating the sample. Once excited, the species decayed back to the unexcited state at a fixed rate, corresponding to the spontaneous emission of photons. The total emitted fluorescence signal was interpreted as proportional to this de-excitation flux. To represent experimental noise in the photon capture process, we drew a random number of captured photons at each time step from a binomial distribution, parameterised by a number p that corresponds to the mean fraction of released photons that are captured.

The model had 17 parameters in total describing the molecules' concentrations and reaction rates (Methods). We set 13 of these parameters to values from the literature. The remaining 4 parameter values we fit to publicly-available data (Berens et al., 2018), briefly explained as follows (see Methods for full details). Single neurons from acute rat cortical slices expressing GCaMP6f were imaged with two-photon microscopy while the membrane potentials of the somata of the same neurons were simultaneously recorded via whole-cell patch clamp electrophysiology. In this dataset, the electrical recordings give unambiguous information about neurons' spike times. To do the parameter fitting, we feed these spike trains as inputs to the computational model. After running, the model returns a simulated fluorescence trace. We aimed to find the model parameter values that give the best match between this simulated fluorescence trace and the real fluorescence time series recorded in the corresponding neuron. To do this we used a suite of optimisation procedures to jointly fit both the real neuron's fluorescence time series and power spectrum, which capture complementary information about the spikes-to-fluorescence mapping (Methods). We performed the fitting procedure independently for each of the 20 neurons in the spikefinder dataset (<http://spikefinder.org>). After fitting, the model produced realistic-looking fluorescence time series (Figure 2.1).

2.3.2 Spike inference algorithms perform similarly on real data compared with time series simulated from the model

Researchers often pass the fluorescence time series through a spike inference tool before performing further statistical analyses. These spike inference algorithms take the fluorescence trace as input and attempt to estimate the neuronal spike train that triggered them (Vogelstein

2.3. Results

et al., 2010; Pnevmatikakis et al., 2016; Friedrich and Paninski, 2016; Pnevmatikakis et al., 2013; Pnevmatikakis et al., 2014; Deneux et al., 2016). Part of our motivation for building this model was to allow us to ask the question on non-linearities properties of the cell and the calcium indicator affect the quality of spike inference? In order to trust the conclusions from our model, we should first be confident that spike inference from our simulated fluorescence traces is similar to that from the real data. To test this we passed each of the simulated fluorescence traces through three previously published spike inference algorithms, quantified their performance against the ground-truth electrophysiology data, repeated the procedure for the real calcium fluorescence time series, and compared the accuracy of the inference processes in all cases. The *true positive rate*, also known as the *recall*, the *sensitivity*, or the *probability of detection* of spike inference varied across the three inference algorithms we tried (p value and statistical test here). The constrained non-negative matrix deconvolution algorithm (Pnevmatikakis et al., 2016) (CNMD algorithm) correctly detected approximately 45% of the true spikes, the OASIS algorithm (Friedrich and Paninski, 2016) correctly detected approximately 35% of the true spikes, and the ML spike algorithm (Deneux et al., 2016) correctly detected approximately 15% of the true spikes (see figure 2.2). Notably, for two of the three inference algorithms, the quality of inference was also fairly consistent for individual spike trains, not just the group means ($p > 0.05$, paired t-test). This demonstrates that the models were generating fluorescence time series that were similarly difficult to decode as the real data, in ways that were not specific to any one inference algorithm. This is evidence that the models captured real aspects of the spikes-to-fluorescence transform.

2.3.3 Relative effects of various buffers to the fluorescence signal

One of the benefits of computational models over laboratory experiments is that we can observe all the variables in the simulation to gain insight into the system's dynamics, which can be difficult to do in the lab. We plotted the concentrations of the various species over time for a version of the model fit to one data set, in response to the same train of spikes used for fitting (figure 2.3). Figure 2.3a shows the absolute values of the species concentrations, summed. Consistent with experimental estimates (Maravall et al., 2000), only a small fraction ($\sim 0.1\%$) of calcium is free and unbound to any buffer. Of the bound calcium, the vast majority, ($\sim 96\%$) is bound to the GCaMP indicator. The two types of endogenous buffer are bound to the remaining calcium ($\sim 4\%$). An influx of calcium from a single spike adds very little to the total calcium, in relative terms (red line in Figure 3a).

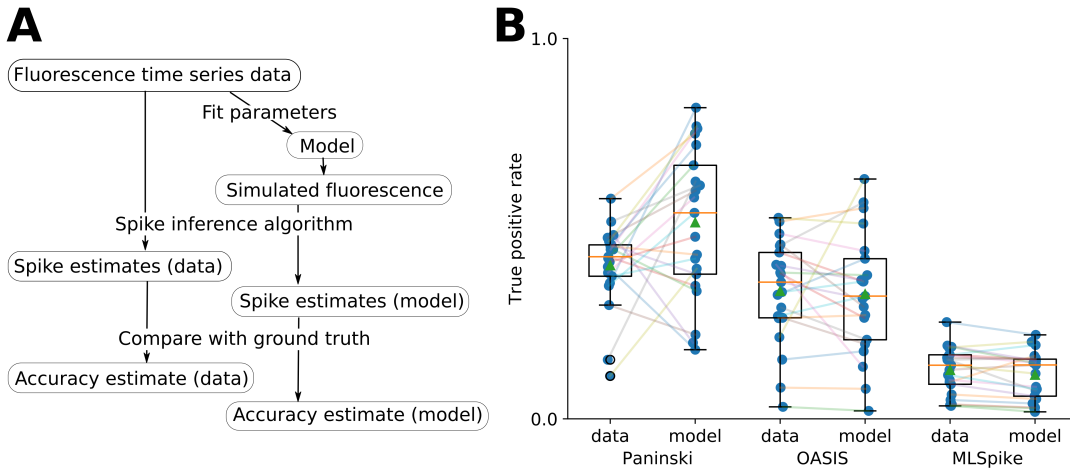


FIGURE 2.2:
A: Workflow to compare spike inference for real versus simulated fluorescence data.
B: True positive rates achieved by three different spike inference algorithms when applied to observed spike trains, and simulated spike trains. Data points overlaid as blue circles. The performance is similar from real and simulated data for each of the algorithms.
quantities

When calcium entered the model neuron it was rapidly buffered (Bartol et al., 2015). However the relative fractions of which buffer molecules bound to the influxed calcium was dynamic, and changed over time. Figure 2.3 (b-f) shows the time course of the various species over time in response to a calcium influx event from a single action potential. Crucially, the indicator $[BCa]$ competed with the endogenous buffers $[ImCa]$ and $[ECa]$ – all three bind calcium on similar timescales. This implies that the timecourse and amplitude of the $[BCa]$ variable will also depend on the binding rates and availabilities of the endogenous buffers. For example if we decreased the concentration of an endogenous buffer, we might expect both a faster rise time and greater peak amplitude of the $[BCa]$ signal in response to a calcium influx event. The slowest component of the decay had a similar time constant for $[BCa]$, $[ImCa]$ and $[ECa]$, which in turn matched the $[Ca]$ extrusion time constant in our model ($\sim 6.29 \times 10^{-22} \text{Ms}^{-1}$). This implies that the buffers and the indicator had reached a dynamic equilibrium and were jointly tracking the free calcium concentration as calcium was slowly extruded from the cell.

Interestingly the excited bound calcium species ($[BCa^*]$) showed a qualitatively different timecourse in response to a calcium influx event. This concentration is subject to the added ‘excitation and release’ dynamic, where a certain proportion of the concentration absorbs the energy from an incoming photon and goes into an ‘excited state’ at each time step. A certain proportion of the concentration releases a photon and reverts to a ‘relaxed state’ at each

2.3. Results

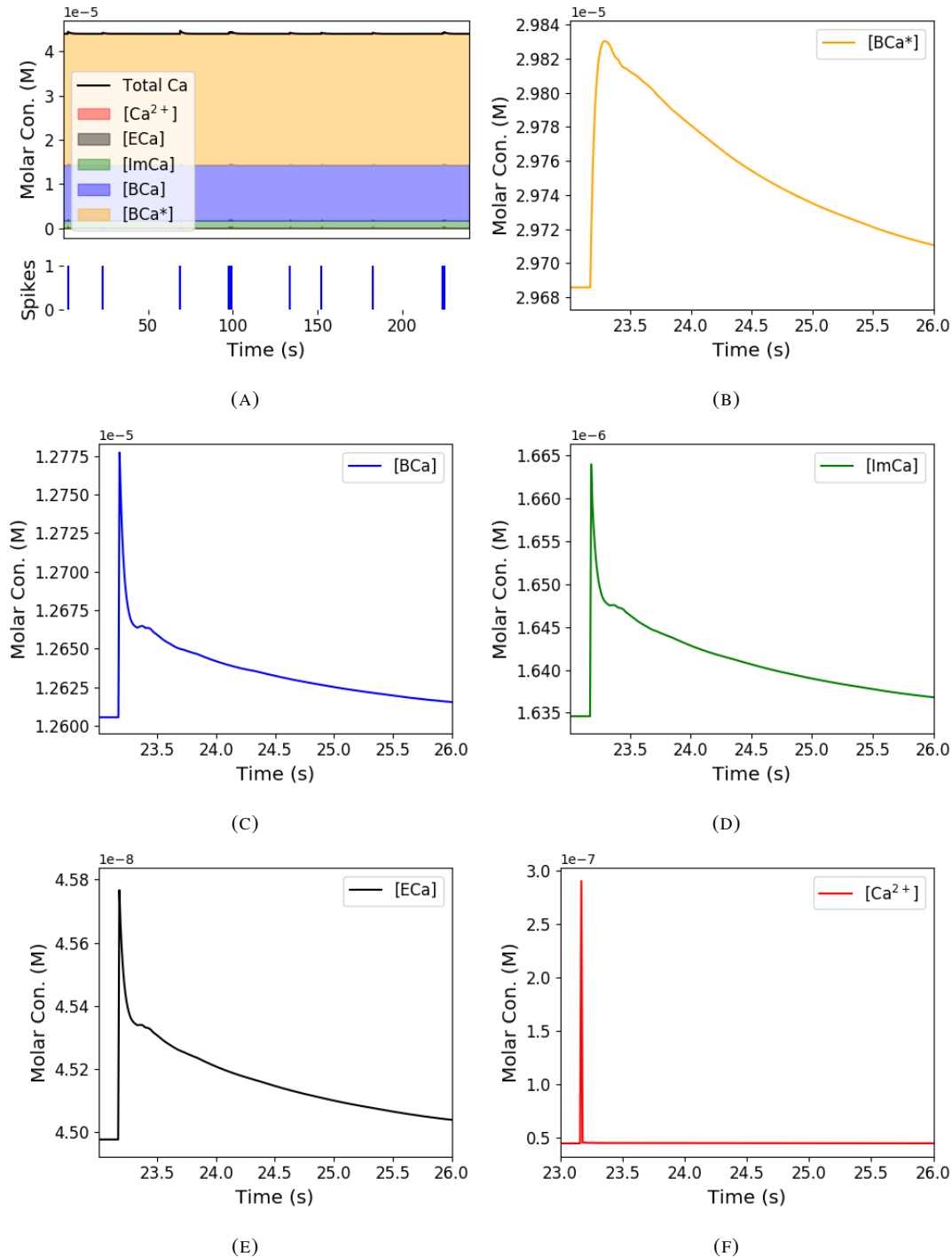


FIGURE 2.3: Calcium Buffering Dynamics (A) The proportions of bound and free calcium concentrations within a cell, with the associated spike train. (B)-(F) The dynamics of the concentration of (B) excited indicator bound calcium, (C) indicator bound calcium, (D) immobile endogenous buffer bound calcium, (E) mobile endogenous buffer bound calcium, and (F) free calcium in response to an action potential at ~ 23.2 s.

1008 timestep also. This means that the excited bound calcium lags behind the bound calcium
1009 trace. We could think of the excited bound calcium trace as a low pass filtered version of the
1010 bound calcium trace.

1011 **2.3.4 Spike inference accuracy is sensitive to indicator properties, and likely
1012 varies within and between cells**

1013 The above results imply that the fluorescence signal depends on the relative properties of
1014 both GCaMP and the endogenous buffers. We next used the model to directly ask how
1015 sensitive spike inference was to these components. We focused on three key parameters that
1016 likely vary from cell to cell and experiment to experiment: GCaMP binding kinetics, GCaMP
1017 concentration, and endogenous buffer concentration.

1018 Several variants of GCaMP itself have been made that differ in calcium binding kinetics,
1019 baseline fluorescence, fluorescence efficiency, and other factors. For example, GCaMP6f has
1020 a decay time constant of $\sim 1\text{s}$, while GCaMP6s has a decay time constant of $\sim 2\text{s}$ (Chen
1021 et al., 2013). Here we asked how these differences in binding kinetics affect spike inference.
1022 We jointly varied the calcium binding and unbinding rates of the indicator by the same factor
1023 over a range from 100-fold slower to 100-fold faster from the fitted values, and simulated the
1024 fluorescence response for each of the parameter settings in response to the same spike trains
1025 as before (figure 2.4). Notably this manipulation does not affect the indicators affinity, and
1026 therefore would not affect steady-state responses to prolonged changes in calcium. Instead
1027 it is likely to affect its sensitivity to the spike train dynamics. We computed two summary
1028 measures from the simulated fluorescence traces: the signal-to-noise ratio for a single spike
1029 (Methods, section 2.2.6), and the accuracy of spike inference for each of the spike trains. We
1030 observed a reduction in the signal-to-noise ratio and the spike inference quality when we set
1031 the binding and unbinding rates were set to one hundredth of their fitted values, and to one
1032 tenth of their fitted values. When we increased the value of both binding rates, we observed
1033 no change in these measurements. The reduction in both rates lead to smaller increases in
1034 fluorescence in response to an action potential and a longer decay time (figure 2.4a), this
1035 caused the reduction in signal-to-noise ratio. As both rates were increased, the change in
1036 $\Delta F/F_0$ in response to an action potential increased and the decay time decreased slightly,
1037 but the fluorescence trace created by these values was very similar to the trace created by the
1038 fitted values.

1039 Second, the overall concentrations of GCaMP often varies from cell to cell. For exam-
1040 ple different cells, even of the same type in the same tissue, can express different levels of

2.3. Results

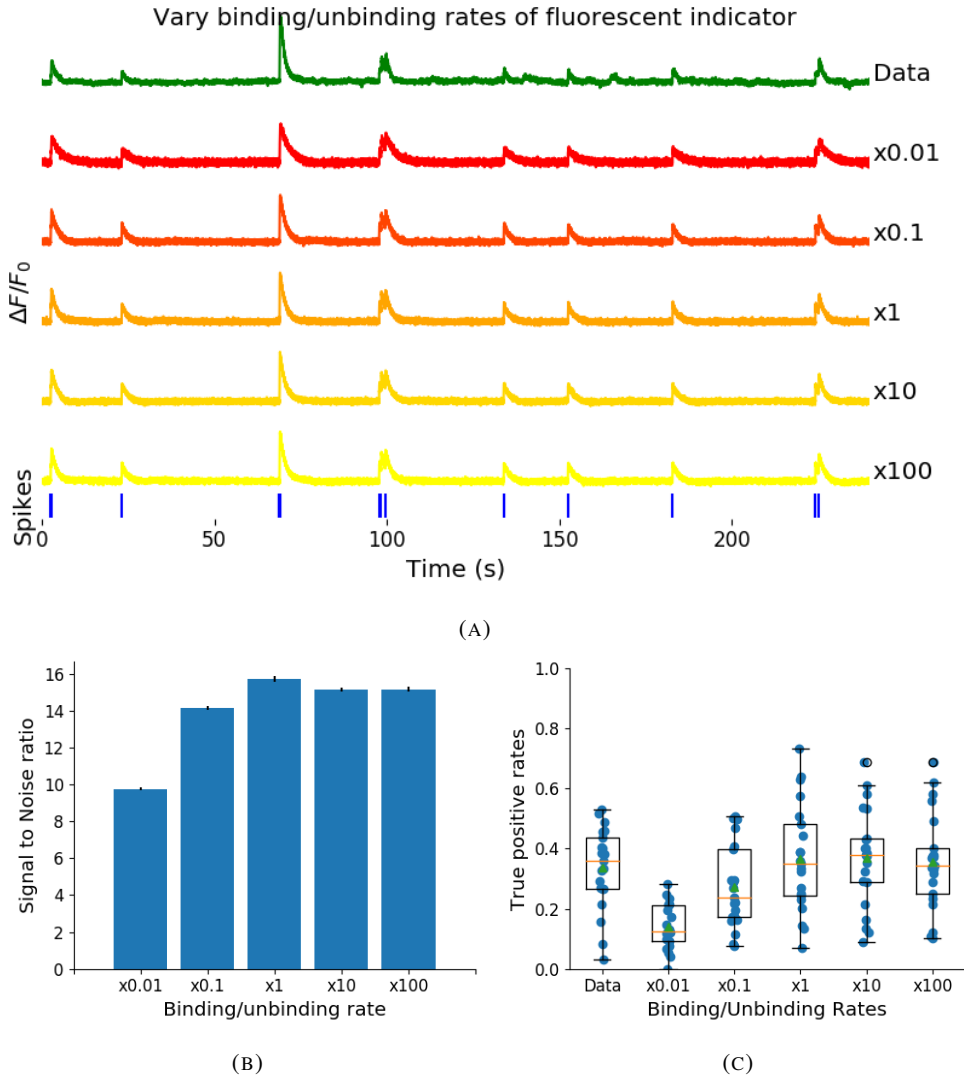


FIGURE 2.4: (A) An example trace for each of the five pairs of values used for the binding and unbinding rates of the fluorescent calcium indicator. (B) The signal-to-noise ratio of the modelled fluorescence traces using each of the four perturbed value pairs, and the experimental value. The SNRs for the value pairs perturbed downward are lower than that for the unperturbed value pair or the higher value pairs. (C) The true-positive rates of the deconvolution algorithm's predictions when inferring from the observed data, and inferring from modelled traces using the perturbed and experimental values.

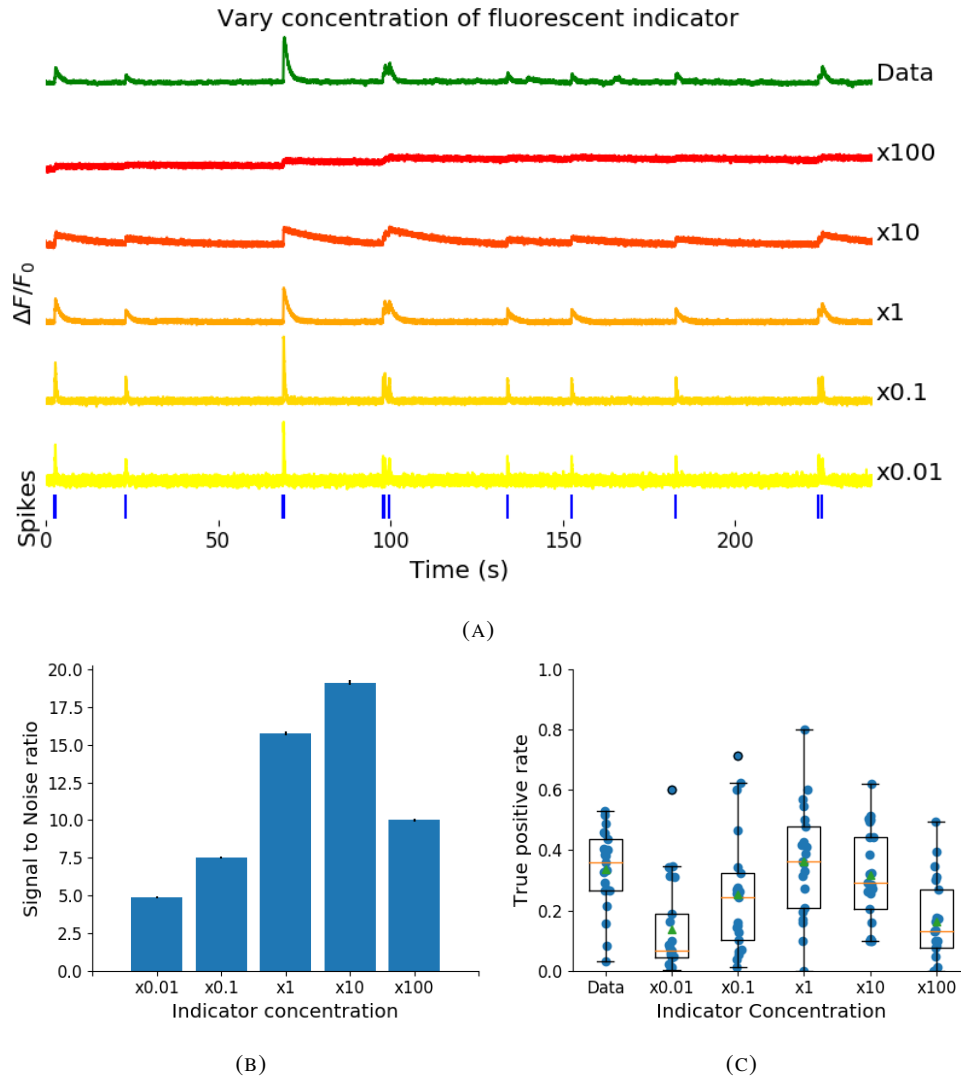


FIGURE 2.5: (A) An example trace for each of the five perturbed values for the concentration of fluorescent calcium indicator. The top two traces are produced by the lower perturbed values, the middle trace is produced by the experimental value, and the lowest two traces are produced when using the higher perturbed values. (B) The signal-to-noise ratio of the modelled fluorescence traces using each of the four perturbed values, and the experimental value. Extreme perturbations of the concentration either above or below the experimental level lowered the SNR. (C) The true-positive rates of the deconvolution algorithm's predictions when inferring from the observed data, and inferring from modelled traces using the perturbed and experimental values. We found that the algorithms performs equally badly on the two most extreme values, and performs equally well on the experimental value, and the next higher perturbed value.

2.3. Results

1041 GCaMP, due to proximity to the infection site, or the cell becoming ‘nuclear-filled’ (Tian et
1042 al., 2009; Chen et al., 2013). Also, GCaMP is often used for longitudinal experiments where
1043 the same cells are re-imaged across multiple days or weeks. However since GCaMP expres-
1044 sion typically ramps up over time (Chen et al., 2013), the accuracy of spike inference may
1045 differ across multiple longitudinal recordings in the same cell. We addressed this by varying
1046 the concentration of calcium indicator in the model, simulating spike trains and measuring
1047 signal-to-noise ratio and spike inference accuracy on the resulting fluorescence traces. Both
1048 increasing and decreasing the concentration of the indicator had effects on the fluorescence
1049 trace, signal-to-noise ratio, and spike inference. The signal-to-noise ratio and spike inference
1050 quality decreased with decreased indicator concentration, and both showed a decrease when
1051 the indicator concentration was increased to 100 times its fitted value (figure 2.5). The signal-
1052 to-noise ratio showed an increase when the indicator concentration was increased to 10 times
1053 its fitted value, but there was no corresponding change in the spike inference quality. The
1054 decrease in indicator concentration caused a reduction in the increase in $\Delta F/F_0$ in response
1055 to an action potential, and an increase in the decay time of this increase (figure 2.5a). The
1056 increase in indicator concentration had the opposite effect, it caused an increase in the change
1057 in $\Delta F/F_0$ in response to an action potential, and a decrease in the decay time.

1058 Third, the concentration and types of endogenous calcium buffers also vary from neuron
1059 to neuron, both within and between cell types (Bartol et al., 2015; Maravall et al., 2000;
1060 Neher and Augustine, 1992). Since the calcium buffer capacity of neurons is high, around
1061 50-70 (Lee et al., 2000) in excitatory hippocampal pyramidal cells, around 100-250 (Lee et
1062 al., 2000) in inhibitory hippocampal pyramidal cells, and 900-200 in Purkinje cells (depend-
1063 ing on the age of the subject), these endogenous buffers compete with GCaMP for binding
1064 to calcium, and variations in endogenous buffer concentration may affect GCaMP signal and
1065 therefore spike inference. To address this we varied the concentration of the endogenous
1066 buffer in the model neuron over five orders of magnitude from 0.8 to 8000 μM , simulated
1067 calcium fluorescence traces in response to the same set of spike trains, and performed spike
1068 inference on the resulting fluorescence time series. Increasing the endogenous buffer con-
1069 centration had a substantial effect on the GCaMP fluorescence signal, both decreasing its
1070 amplitude and slowing its kinetics (figure 2.6(a)). This corresponded with a decrease in both
1071 single-spike signal-to-noise ratio (figure 2.6(b)) and spike inference accuracy (figure 2.6(c)).
1072 In contrast, decreasing endogenous buffer capacity from the fitted value had little effect on
1073 either the GCaMP signal or spike inference (figure 2.6).

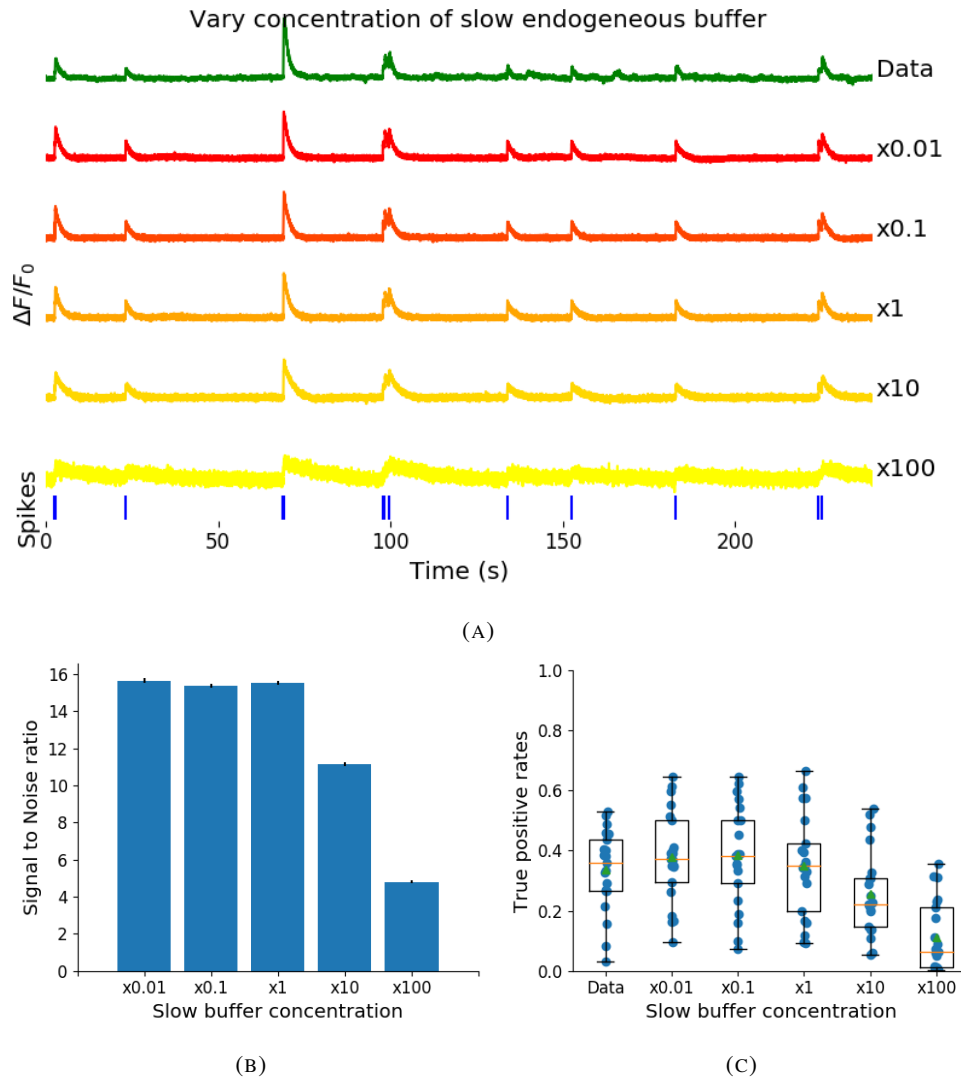


FIGURE 2.6: (A) An example trace for each of the five perturbed values for the concentration of immobile endogenous buffer. (B) The signal-to-noise ratio of the modelled fluorescence traces using each of the four perturbed values, and the experimental value. The lower values for the immobile buffer produce the same SNR as the experimental value. But the higher perturbed values produce fluorescence traces with a lower SNR. (C) The true-positive rates of the deconvolution algorithm's predictions when inferring from the observed data, and inferring from modelled traces using the perturbed and experimental values.

1074 **2.3.5 Single spike inference accuracy drops for high firing rates, but firing rate**
1075 **itself can be estimated from mean fluorescence amplitude**

1076 The fluorescence signal recorded from neurons using calcium indicators is typically much
1077 slower than changes in membrane potential for two reasons: first, because the calcium and
1078 the indicator have slow binding and unbinding kinetics, the signal is a low-pass filtered ver-
1079 sion of the membrane potential. Second, neuronal two-photon imaging experiments are often
1080 performed in scanning mode, which limits their frame rate to $\sim 10\text{Hz}$ or slower. This im-
1081 plies that multiple spike events that occur close in time might be difficult to resolve from a
1082 calcium indicator time series. Many cells, especially several types of inhibitory interneurons,
1083 fire tonically at rates higher than 10Hz. We used the model to test whether spike inference
1084 accuracy depended on the neuron's firing frequency by driving the cell with spike trains sam-
1085 pled from a Poisson processes of varying frequency. We simulated a variable firing rate using
1086 an Ornstein-Uhlenbeck process, and simulated the spike trains using a Poisson distribution
1087 with its rate taken from this process. Because of the high frequency firing rate of these spike
1088 trains, we used the accuracy as the measure of spike inference quality. We simulated 30
1089 spike trains at average firing rate of 1, 5, and 10Hz, and measured the spike inference quality
1090 of all these traces. Spike inference accuracy decreased with increasing firing rate, for up to
1091 10Hz Poisson spike trains (figure 2.8(left)). Although the accuracy remained above 90% for
1092 each of the three frequencies. We also plotted the average $\Delta F / F_0$ as a function of stimula-
1093 tion firing rate. We found that it increased monotonically as a function of firing rate (figure
1094 2.8(right)).

1095 We expected lower spike inference quality as the average spiking frequency increased.
1096 Since the fluorescence trace, in some sense, is a low pass filtered version of the spike train, a
1097 tightly packed groups of spikes will be more difficult to infer than isolated spikes. However,
1098 the increasing amplitude of the fluorescence trace with increasing frequency suggests that
1099 some spike inference algorithm could be developed based on this amplitude.

1100 **2.4 Discussion**

1101 We designed a biophysical model for the changes in free calcium and bound calcium con-
1102 centrations within a cell soma with a fluorescent calcium indicator. We used this model to
1103 model the fluorescence trace resulting from a spike train in this cell. We fit the free parame-
1104 ters of the model by matching the power spectrum and amplitude of fluorescence traces with
1105 simultaneously measured spike trains. We inferred spikes from real fluorescence traces and

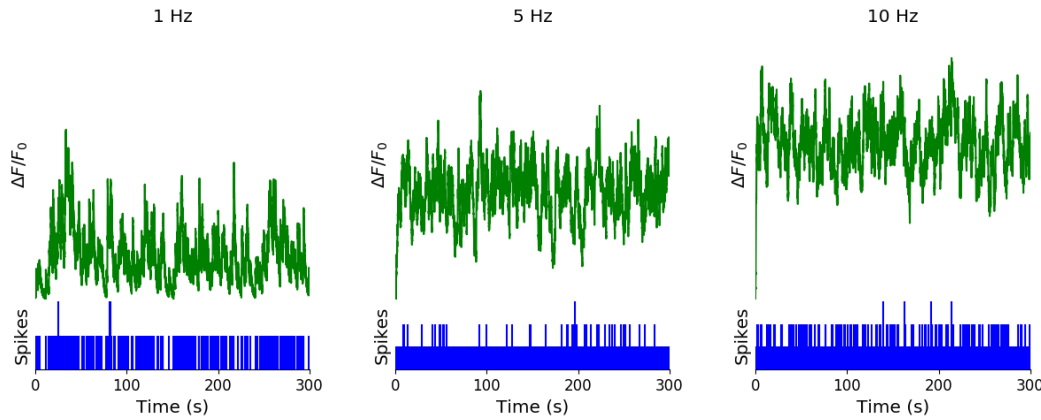


FIGURE 2.7: Simulating fluorescence traces at different firing rates Example modelled traces created using simulated spike trains with a mean firing rate of 1Hz (left column), 5Hz (middle column), and 10Hz (right column). Note the difference in amplitude with different mean firing rates.

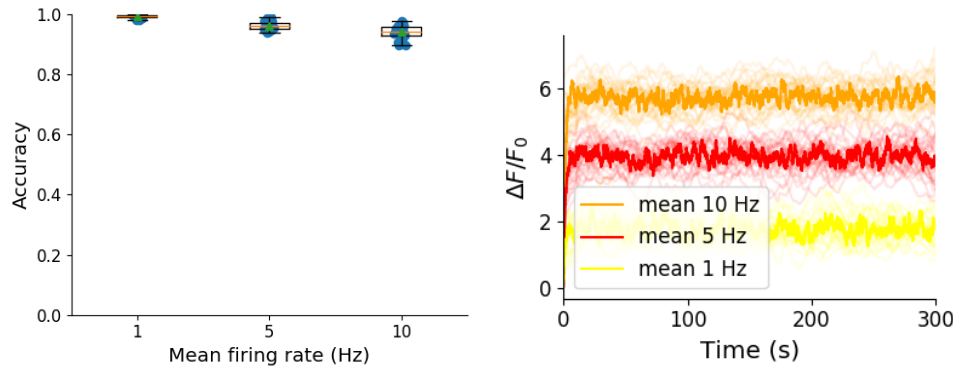


FIGURE 2.8: Inference quality and $\Delta F/F_0$ vs Firing rate (left) The spike inference accuracy when applied to 30 traces created using simulated spike trains with mean firing rates of 1, 5, and 10 Hz. (right) The mean $\Delta F/F_0$ across those 30 traces for each frequency.

1106 modelled fluorescence traces, and measured the quality of the spike inference in both cases.
 1107 We found that the spike inference quality was similar in both cases. We perturbed the concen-
 1108 tration of the calcium buffers in the model, and the binding/unbinding rates of those buffers
 1109 in the model, and measured the effect on the signal-to-noise ratio (SNR) of the modelled
 1110 fluorescence traces and the spike inference quality.

1111 For the fluorescent calcium indicator, we found that any large perturbation away from
 1112 the taken from the literature led to a reduction in SNR, and spike inference quality. For the
 1113 binding/unbinding rates, we kept the ratio of these rates constant, but altered their values in
 1114 parallel. The lower values caused a reduction in SNR, and a reduction in spike inference
 1115 quality. For the endogenous buffer concentration, an increase above the experimental value
 1116 caused a reduction in SNR and spike inference quality.

2.4. Discussion

1117 Although the model produced visually similar time series to the real data, there were a
1118 few aspects it did not capture. First, the real data featured some low-frequency components
1119 that did not appear related to the spike events. These were not captured by the models we
1120 used in this study, but could be added in future by adding a suitable low-frequency term to the
1121 resulting time series. Second, the real data seemed to have some non-linearities not captured
1122 in the model, for example the response to two nearby spikes was greater than expected from
1123 the linear sum of two single spikes. This may be due to the co-operative binding of calmod-
1124 ulin to calcium, which gives calmodulin a supra-linear sensitivity to calcium concentration
1125 (Faas et al., 2011). The non-linear dynamics of this binding have been included in a recently
1126 developed spike inference model (Greenberg et al., 2018). Our model, in contrast, behaved
1127 much more linearly but could be extended in future to include such non-linearities. Third,
1128 in the real data the fluorescence peak amplitude seemed to vary from spike to spike, even
1129 for well-isolated spike events. Recent research has shown that calcium influx due to a single
1130 action potential was quite variable in pyramidal cells, and that this variability had a effect on
1131 spike inference (Éltes et al., 2019). However in our model we assumed each spike lead to the
1132 same fixed-amplitude injection of calcium to the cell, leading to much greater regularity in
1133 fluorescence peak amplitudes. This variability could be added in future versions of the model
1134 by making the injected calcium peak a random variable. Fourth, we modelled the soma as
1135 a single compartment, but in reality there is likely a non-uniform spatial profile of calcium
1136 concentration. This may matter because some endogenous buffers might access calcium right
1137 as it influxes from the extracellular space, whereas the majority of the fluorescence signal is
1138 more likely coming from the bulk of the cytoplasm. Future models could attempt to model
1139 these spatial dependencies to assess whether they affect the overall spike inference procedure.

1140 As well as the optimised parameters, the model has 14 fixed parameters than can be
1141 changed to simulate different types of calcium indicators. This model could be used to test
1142 the theoretical performance of proposed new types of calcium indicator. The model could
1143 also be used by developers of spike inference algorithms to test the effects of changing cal-
1144 cium indicator parameters on spike inference, or to test the affects of changing spiking char-
1145 acteristics on spike inference. For example, high firing rate vs low firing rate, or bursting vs
1146 no bursting. Given the increasing amplitude of the fluorescence trace with increasing mean
1147 firing rate, it would be possible to build a spike inference algorithm on this principle at least
1148 in part.

1149 Our model has already been used as a tool by our colleagues, for simulating fluorescence
1150 traces in response to cells that can fire with a continuous rate between 10 and 20Hz, but do

1151 not always do so. Our colleagues found that a combination of the amplitude and the variance
1152 of the simulated fluorescence trace was the best indicator of firing rate. For example, when
1153 a cell was not firing, the amplitude and variance of the fluorescence trace was relatively low.
1154 When the cell fired with a low firing rate $\sim 1\text{Hz}$, the mean amplitude was still low but
1155 the variance of the fluorescence trace was high, and for high firing rate $\sim 10 - 20\text{Hz}$, the
1156 fluorescence amplitude was high, and the variance was low. In this way, our model may be
1157 useful for investigating firing rates underlying real fluorescence traces in response to cells
1158 which can fire in these rage ranges.

1159 A recent paper by Greenberg et al (2018) described a biophysical model for spike train
1160 inference called the ‘Sequential binding model’. Their model for spike inference was sim-
1161 ilar to our model for fluorescence traces in that their model included parameters for two
1162 types of endogenous buffer. But this model also included dynamics for calcium binding to
1163 and unbinding from these endogenous buffers. Furthermore, this model included dynamics
1164 for calcium binding to and unbinding from the four binding sites present on a GCaMPs6
1165 molecule. In the accuracy measurements specified in that paper, this model performed better
1166 than the MLspike algorithm, which is also partially a biophysically model, and it performed
1167 better than the constrained non-negative deconvolution algorithm. The sequential binding
1168 model also has biophysically interpretable parameters, and its fitted parameters for quantities
1169 such as buffering capacity and calcium influx upon action potential firing fall in line with
1170 experimental values (Greenberg et al., 2018). Biophysical models like this appear to be the
1171 way forward for spike inference algorithms, and would make a good complimentary tool to
1172 our fluorescence model.

1173 **Chapter 3**

1174 **Functional networks expand across
1175 anatomical boundaries as correlation
1176 time-scale increases**

1177 *Abstract*

1178 Decades of research has established that correlated spiking plays a crucial role in represent-
1179 ing sensory information. One drawback associated with the recent improvement in recording
1180 technology and consequent large datasets is the difficulty in analysing higher order correla-
1181 tions in large neuronal ensembles. One benefit of these datasets that has not yet been explored
1182 is the opportunity to compare correlations within anatomical regions to correlations across
1183 anatomical regions. In this work, we measured correlations between neurons residing in
1184 nine different brains regions in three awake and behaving mice. Using the these correlation
1185 measurements, we created weighted undirected graph networks and applied network science
1186 methods to detect functional communities in our neural ensembles. We compared these func-
1187 tional communities to their anatomical distribution. We repeated the analysis, using different
1188 timescales for our correlation measurements, and found that functional communities were
1189 more likely to be dominated by neurons from a single brain region at shorter timescales
1190 (< 100ms).

1191 3.1 Introduction

1192 Decades of research has established that correlations play a crucial role in representing sen-
1193 sory information. For example, the onset of visual attention has been shown to have a greater
1194 affect on the correlations in the macaque V4 region than on the firing rates in that region
1195 (Cohen and Maunsell, 2009). Recent findings show that spontaneous behaviours explain cor-
1196 relations in parts of the brain not associated with motor control (Stringer et al., 2019), that
1197 satiety state appears to have a brain wide representation (Allen et al., 2019), and that subject
1198 exploratory and non-exploratory states are represented in the amygdala (Gründemann et al.,
1199 2019). So, behavioural states are likely represented across many regions of the brain, not just
1200 motor related areas. In order to understand the brain, we must understand the interactions
1201 between neurons and regions.

1202 Because of limitations in recording technology almost all research has explored corre-
1203 lations between neurons within a given brain region, or within only two regions at most
1204 (Wierzynski et al., 2009; Patterson et al., 2014; Girard, Hupé, and Bullier, 2001). Rela-
1205 tively little is known about correlations between neurons in many different brain regions.
1206 However, the recent development of ‘Neuropixels’ probes (Jun et al., 2017) has allowed
1207 extracellular voltage measurements to be collected from multiple brain regions simultane-
1208 ously routinely, and in much larger numbers than traditional methods. In this project we
1209 used a publicly-available Neuropixels dataset to analyse correlations between different brain
1210 regions (Stringer et al., 2019).

1211 A drawback associated with the improvement in recording technology is an increase in
1212 the difficulty in analysing these data. For example, analysing the i th order interactions of
1213 N neurons generally requires estimation of N^i parameters. A number that becomes astro-
1214 nomical for large N . New methods are required for analysing these new large datasets. We
1215 attempted to address this requirement in this piece of research by applying a cutting-edge
1216 network science community detection method to neural data.

1217 Another unexplored area of research is the changes in cell interactions at different timescales.
1218 Studies have shown different timescales for fluctuations in spiking activity (Murray et al.,
1219 2014), and different time scales for event representation (Baldassano et al., 2017) across dif-
1220 ferent brain regions. Still most studies focus on quantifying interactions at a given timescale.
1221 But neurons may interact differently, or may interact with different neurons at different
1222 timescales. Here we explore correlated communities of neurons at different timescales.

1223 In this work, we measured correlations between binned spike counts from neurons from

3.2. Data

1224 nine different regions of the mouse brain. These measurements induced a weighted undi-
1225 rected graph or network where each neuron is represented by a node, and the strength of
1226 the connection between these nodes/neurons is the strength of the correlation between their
1227 spike counts. We then applied newly invented network methods (Humphries et al., 2019)
1228 to this network to find any community structure, and place the neurons in these correlation
1229 based communities. Finally, we compared these functional communities to the anatomical
1230 membership of the neurons.

1231 To investigate the functional communities and their relationship with anatomy at different
1232 time scales, we repeated these analyses using different length bin widths when binning spike
1233 times.

1234 To find and analyse functional networks while controlling for the subject’s behaviour, we
1235 conditioned the binned spike counts on data from a video of the subject’s face, and repeated
1236 our analysis for spike count correlations (or noise correlations) and signal correlations.

1237 3.2 Data

1238 The data that we used in this project were collected by Nick Steinmetz and his lab members
1239 (Stringer et al., 2019; Steinmetz et al., 2019).

1240 3.2.1 Brain regions

1241 Neuropixels probes were used to collect extracellular recordings (Jun et al., 2017) from three
1242 different mice. The mice were awake, headfixed, and engaging in spontaneous behaviour.
1243 The mice were of different sexes and different ages. One mouse was ‘wild-type’, the others
1244 were mutants. Details as follows:

- 1245 1. male, wild type, P73.
1246 2. female, TetO-GCaMP6s, Camk2a-tTa, P113
1247 3. male, Ai32, Pvalb-Cre, P99

1248 Eight probes were used to collect readings from 2296, 2668, and 1462 cells respectively.
1249 Data were collected from nine brain regions in each mouse:

- 1250 • Caudate Putamen (CP)
1251 • Frontal Motor Cortex (Frmoctx)
1252 • Hippocampal formation (Hpf)

- 1253 ● Lateral Septum (Ls)
- 1254 ● Midbrain (Mb)
- 1255 ● Superior Colliculus (Sc)
- 1256 ● Somatomotor cortex (Sommotcx)
- 1257 ● Thalamus (Th)
- 1258 ● Primary visual cortex (V1)

1259 Readings were continuous and lasted for about 1 hour (Stringer et al., 2019; Steinmetz et al.,
1260 2019). Locations of each of the probes can be seen in figure 3.1.

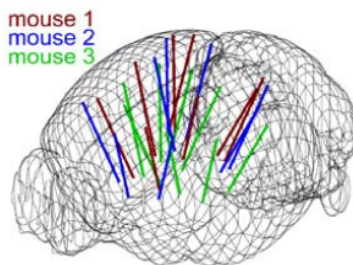


FIGURE 3.1: **Probe Locations:** The locations of the probes in each of the three mouse brains (Stringer et al., 2019).

1261 3.2.2 Video recordings

1262 Video recordings of the mouse's face were taken during the spontaneous behaviour. We
1263 had access to the top 500 principle components and top 500 eigenvectors of the processed
1264 videos. The frequency of recording was slightly less than 40Hz. Each frame contained
1265 327×561 pixels (Stringer et al., 2019; Steinmetz, Carandini, and Harris, 2019). These
1266 principal components were used as behavioural data. We controlled for these components
1267 when taking measurements conditioned on behaviour.

1268 3.3 Methods

1269 3.3.1 Binning data

1270 We transformed the spike timing data into binned spike count data by dividing the experi-
1271 mental period into time bins and counting the spikes fired by each cell within the time period
1272 covered by each of those bins. The data were divided into time bins of various widths ranging
1273 from 0.005s to 4s.

3.3. Methods

If the total length of the recording period was not an integer multiple of the time bin width, we cut off the remaining time at the end of the recording period. This period was at most 3.99s. This is far less than the total recording time of around 1 hour. So, this detail would not affect our results.

3.3.2 Correlation coefficients

We calculated Pearson's correlation coefficient for pairs of spike counts from pairs of neurons. For jointly distributed random variables X and Y , Pearson's correlation coefficient is defined as:

$$\rho_{XY} = \frac{\text{cov}(X, Y)}{\sigma_X \sigma_Y} \quad (3.1)$$

$$= \frac{E[(X - \mu_X)(Y - \mu_Y)]}{\sigma_X \sigma_Y} \quad (3.2)$$

where E denotes the expected value, μ denotes the mean, and σ denotes the standard deviation. The correlation coefficient is a normalised measure of the covariance. It can take values between 1 (completely correlated) and -1 (completely anti-correlated). Two independent variables will have a correlation coefficient of 0. But, having 0 correlation does not imply independence.

If we do not know the means and standard deviations required for equation 3.1, but we have samples from X and Y , Pearson's sample correlation coefficient is defined as:

$$r_{XY} = \frac{\sum_{i=1}^n (x_i - \bar{x})(y_i - \bar{y})}{\sqrt{\sum_{i=1}^n (x_i - \bar{x})^2} \sqrt{\sum_{i=1}^n (y_i - \bar{y})^2}} \quad (3.3)$$

where $\{(x_i, y_i)\}$ for $i \in \{1, \dots, n\}$ are the paired samples from X and Y , and $\bar{x} = \frac{1}{n} \sum_{i=1}^n x_i$, and $\bar{y} = \frac{1}{n} \sum_{i=1}^n y_i$ are the sample means.

In practice we used the python function `scipy.stats.pearsonr` to calculate the correlation coefficients.

1288 Total correlations, r_{SC}

In this context, we defined the total correlation (r_{SC}) of two cells to be the correlation between the spike counts of those cells across the entire period of spontaneous behaviour.

1291 **Shuffled total correlations**

1292 We measured the shuffled total correlations between two neurons by randomly permuting one
 1293 of the neuron's spike counts and measuring the total correlations. These shuffled correlations
 1294 were useful when measuring the effect of time bin width on correlations, and when decid-
 1295 ing which correlations should be preserved when creating correlation networks (see section
 1296 3.3.5).

1297 **Separating Correlations & Anti-correlations**

1298 In order to compare the effect of bin width on measures of negative r_{SC} (anti-correlation) and
 1299 positive r_{SC} separately, we had to separate correlated and anti-correlated pairs. To do this, we
 1300 simply measured the mean r_{SC} , taking the mean across all the bin widths. If this quantity was
 1301 positive or zero we regarded the pair as positively correlated. If this quantity was negative
 1302 we regarded the pair as anti-correlated.

1303 **3.3.3 Conditioning on behavioural data**

Our behavioural data consisted of the top 500 principal components (PCs) of a processed video recording of the mouse's face (see section 3.2.2). Denoting the spike count of a given cell by X , and the PCs by Z_1, \dots, Z_{500} , we wanted to model X as a function of Z_1, \dots, Z_{500} in order to estimate

$$E[X|Z_1, \dots, Z_{500}] = \int_{x \in X} x P(X = x|Z_1, \dots, Z_{500}) dx \quad (3.4)$$

$$= \int_{x \in X} x \frac{P(X = x, Z_1, \dots, Z_{500})}{P(Z_1, \dots, Z_{500})} dx \quad (3.5)$$

1304 Given the 500 components, a naïve estimation of $P(Z_1, \dots, Z_{500})$ or $P(X, Z_1, \dots, Z_{500})$ by
 1305 histogramming was impossible. Therefore we modelled X as a linear combination of the
 1306 PCs.

1307 **Linear regression**

1308 We modelled the spike count of a given cell, X , as a linear combination of the PCs of the
 1309 video of the mouse's face, $\mathbf{Z} = Z_1, \dots, Z_{500}$. We tried three different types of regularization

1310 • L1 or 'Lasso'

1311 • L2 or 'Ridge regression'

3.3. Methods

- 1312 • ‘Elastic net’ regularisation (a linear combination of both $L1$ and $L2$ regularisation
1313 penalties)

1314 The elastic net regularisation performed the best, so we stuck with that.

1315 **Elastic net regularisation**

Suppose we wish to model n observations of a random variable X , $\mathbf{x} = (x_1, \dots, x_n)$ using n instances of m predictors $\mathbf{Z} = (Z_1, \dots, Z_m)$. The naïve elastic net criterion is

$$L(\lambda_1, \lambda_2, \boldsymbol{\beta}) = |\mathbf{x} - \mathbf{Z}\boldsymbol{\beta}|^2 + \lambda_2|\boldsymbol{\beta}|_2 + \lambda_1|\boldsymbol{\beta}|_1 \quad (3.6)$$

where

$$|\boldsymbol{\beta}|_2 = \sum_{j=1}^m \beta_j^2 \quad (3.7)$$

$$|\boldsymbol{\beta}|_1 = \sum_{j=1}^m |\beta_j| \quad (3.8)$$

The naïve elastic net estimator $\hat{\boldsymbol{\beta}}$ is the minimiser of the system of equations 3.6 (Zou and Hastie, 2005)

$$\hat{\boldsymbol{\beta}} = \arg \min_{\boldsymbol{\beta}} L(\lambda_1, \lambda_2, \boldsymbol{\beta}) \quad (3.9)$$

1316 We implemented the model using the `ElasticNetCV` method of Python’s
1317 `sklearn.linear_models` package.

1318 As well as using the PCs, we also tried fitting the models using the raw video data recon-
1319 structed from the PCs and eigenvectors. These models performed worse than those using the
1320 PCs. We expected this because each representation contains the same amount of information,
1321 but the raw video representation spreads this information across many more components.
1322 This requires more parameter fitting, but given the same information.

1323 **Conditional covariance**

We calculated the expected value of the conditional covariance using the law of total covariance.

$$\text{cov}(X, Y) = E[\text{cov}(X, Y|Z)] + \text{cov}(E[X|Z], E[Y|Z]) \quad (3.10)$$

1324 where these expected values are calculated with respect to the distribution of Z as a random
 1325 variable.

1326 The law of total covariance breaks the covariance into two components. The first com-
 1327 ponent $E[\text{cov}(X, Y|Z)]$ is the expected value, under the distribution of Z , of the conditional
 1328 covariance $\text{cov}(X, Y|Z)$. This covariance could be interpreted as the unnormalised version
 1329 of what Cohen et al. (2011) call the spike count correlation (Cohen and Kohn, 2011), aka.
 1330 the noise correlation. In particular, this is the covariance of the spike counts in response to
 1331 repeated presentation of identical stimuli.

1322 The second component is analogous to what Cohn et al. (2011) call the *signal correlation*
 1323 (Cohen and Kohn, 2011). In particular, $\text{cov}(E[X|Z], E[Y|Z])$ is the covariance between
 1334 spike counts in response to different stimuli.

Using our linear model, we calculated $E[X|Z_1, \dots, Z_{500}]$ for each cell X . Then we pro-
 ceeded to calculate

$$E[\text{cov}(X, Y|Z_1, \dots, Z_{500})] = \text{cov}(X, Y) - \quad (3.11)$$

$$\text{cov}(E[X|Z_1, \dots, Z_{500}], E[Y|Z_1, \dots, Z_{500}]) \quad (3.12)$$

1335 **Measures of conditional correlation**

As a measure of expected correlation, we measured the ‘event conditional correlation’ (Maugis,
 2014)

$$\rho_{XY|Z} = \frac{E[\text{cov}(X, Y|Z)]}{\sqrt{E[\text{var}(X|Z)]E[\text{var}(Y|Z)]}} \quad (3.13)$$

1336 Although this is not an actual correlation, it is an intuitive analogue to the correlation as a
 1337 normalised version of the covariance.

For comparison, we also measured the ‘signal correlation’

$$\rho_{\text{signal}} = \frac{\text{cov}(E[X|Z], E[Y|Z])}{\sqrt{\text{var}(E[X|Z])\text{var}(E[Y|Z])}} \quad (3.14)$$

1338 this is an actual correlation.

3.3.4 Information Theory

Entropy $H(X)$

The entropy of a random variable X , with outcomes x_1, \dots, x_N , and corresponding probabilities p_1, \dots, p_N is defined as

$$H(X) = - \sum_{n=1}^N p_n \log_2 p_n \quad (3.15)$$

This quantity is also known as the information entropy or the ‘surprise’. It measures the amount of uncertainty in a random variable. For example, a variable with a probability of 1 for one outcome, and 0 for all other outcomes will have 0 bits entropy, because it contains no uncertainty. But a variable with a uniform distribution will have maximal entropy as it is the least predictable. This quantity is analogous to the entropy of a physical system (Shannon, 1948). Note that any base may be used for the logarithm in equation 3.15, but using base 2 means that the quantity will be measured in ‘bits’.

The joint entropy of two jointly distributed random variables X and Y , where Y has outcomes y_1, \dots, y_M , is defined as

$$H(X, Y) = - \sum_{n=1}^N \sum_{m=1}^M P(X = x_n, Y = y_m) \log_2 P(X = x_n, Y = y_m) \quad (3.16)$$

If X and Y are independent then $H(X, Y) = H(X) + H(Y)$. Otherwise $H(X, Y) < H(X) + H(Y)$. When X and Y are completely dependent $H(X, Y) = H(X) = H(Y)$.

The conditional entropy of Y conditioned on X is defined as

$$H(Y|X) = - \sum_{n=1}^N \sum_{m=1}^M P(X = x_n, Y = y_m) \log_2 \frac{P(X = x_n, Y = y_m)}{P(X = x_n)} \quad (3.17)$$

When X and Y are independent $H(Y|X) = H(Y)$. Intuitively, we learn nothing of Y by knowing X , so Y is equally uncertain whether we know X or not. If Y is totally dependent on X , then the fraction in the logarithm is 1, which gives $H(Y|X) = 0$.

These entropy measures are the basis of the mutual information measure.

Maximum entropy limit

When spiking data is binned into spike counts there is an upper limit on the entropy of these data. The maximum entropy discrete distribution is the discrete uniform distribution. A

random variable with this distribution will take values from some finite set with equal probabilities. Binned spike count data will take values between 0 and some maximum observed spike count n_{\max} . A neuron with responses that maximises entropy will take these values with equal probability, i.e. if $i \in \{0, \dots, n_{\max}\}$ then $P(X = i) = \frac{1}{n_{\max} + 1}$. The entropy of this neuron will be

$$\begin{aligned} H(X) &= - \sum_{i=0}^{n_{\max}} P(X = i) \log_2 P(X = i) \\ &= - \sum_{i=0}^{n_{\max}} \frac{1}{n_{\max} + 1} \log_2 \left(\frac{1}{n_{\max} + 1} \right) \\ &= - \log_2 \left(\frac{1}{n_{\max} + 1} \right) \\ &= \log_2 (n_{\max} + 1) \end{aligned}$$

1355 Therefore, the maximum entropy of the binned spike counts of a neuron is $\log_2 (n_{\max} + 1)$.
 1356 Of course, it would be very unusual for a neuron to fire in accordance with the discrete
 1357 uniform distribution. Most measurements of entropy taken on binned spiking data will be
 1358 much lower than the maximum. See figure 3.2 to see the maximum entropy as a function of
 1359 the maximum observed spike count.

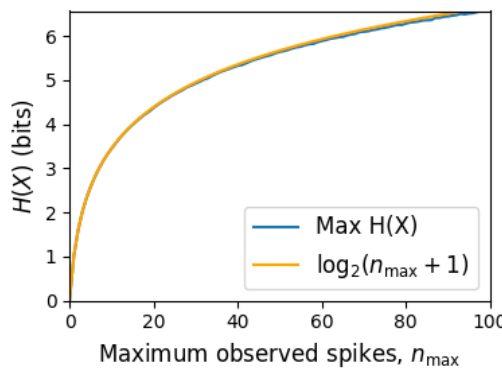


FIGURE 3.2: **Entropy Limit:** The upper limit on entropy of binned spike count data as a function of the maximum observed spike count. The orange line is the analytical maximum. The blue line is the entropy of samples with $N = 1000$ data points taken from the discrete uniform distribution.

1360 **Mutual Information** $I(X; Y)$

1361 The mutual information can be defined mathematically in a number of ways, all of which are
 1362 equivalent. These definitions illustrate the different ways of interpreting the mutual informa-
 1363 tion.

3.3. Methods

For two jointly distributed random variables X and Y , the mutual information $I(X;Y)$ is defined as

$$I(X;Y) = H(Y) - H(Y|X) \quad (3.18)$$

$$= H(X) - H(X|Y) \quad (3.19)$$

1364 Equation 3.18 fits with the following intuition: The mutual information between X and Y is
1365 the reduction in uncertainty about X gained by knowing Y , or vice versa. We could also say
1366 the mutual information is the amount of information gained about X by knowing Y , or vice
1367 versa.

Another useful entropy based definition for the mutual information is

$$I(X;Y) = H(X) + H(Y) - H(X,Y) \quad (3.20)$$

1368 This definition is useful because it does not require the calculation of conditional probabili-
1369 ties.

The mutual information can also be defined in terms of marginal, joint, and conditional distributions. For example,

$$I(X;Y) = - \sum_{n=1}^N \sum_{m=1}^M P(X = x_n, Y = y_m) \log_2 \frac{P(X = x_n, Y = y_m)}{P(X = x_n)P(Y = y_m)} \quad (3.21)$$

Notice that this can be rewritten as a Kullback–Leibler divergence.

$$I(X;Y) = D_{KL}(P(X,Y) || P(X)P(Y)) \quad (3.22)$$

1370 So, we can also think of the mutual information as a measure of the difference between
1371 the joint distribution of X and Y , and the product of their marginal distributions. Since the
1372 product of the marginal distributions is the joint distribution for independent variables, we
1373 can think of the mutual information as a measure of the variables’ dependence on one another.

1374 The minimum value that $I(X;Y)$ can take is 0. This occurs when the random variables
1375 X and Y are independent. Then we have $H(X|Y) = H(X)$, and $H(Y|X) = H(Y)$, which
1376 according to equation 3.18, gives $I(X;Y) = 0$. We also have that $H(X,Y) = H(X) +$
1377 $H(Y)$ in this case, which according equation 3.20, gives $I(X;Y) = 0$. Finally, we also have
1378 $P(X,Y) = P(X)P(Y)$, which leaves us with 1 in the argument for the logarithm in equation
1379 3.21, which again gives $I(X;Y) = 0$.

1380 The mutual information reaches its maximum value when one of the variables X and
1381 Y is completely determined by knowing the value of the other. In that case $I(X; Y) =$
1382 $\min\{H(X), H(Y)\}$.

1383 **Variation of Information** $VI(X, Y)$

The variation of information is another information theoretical quantity based on the mutual information. It is defined as

$$VI(X; Y) = H(X) + H(Y) - 2I(X; Y) \quad (3.23)$$

We can rewrite this as the summation of two positive quantities

$$VI(X; Y) = [H(X) - I(X; Y)] + [H(Y) - I(X; Y)] \quad (3.24)$$

1384 In English, the variation of information is the summation of the uncertainty in the random
1385 variables X and Y excluding the uncertainty shared by those variables.

1386 This measure will become more relevant when we go on to talk about clusterings because
1387 $VI(X; Y)$ forms a metric on the space of clusterings.

1388 **Measuring entropies & mutual information**

1389 In practice, we measured the mutual information between spike counts using Python and the
1390 python package `pyitlib`. We used the PT-bias correction technique to estimate the bias of
1391 our measurements when measuring the mutual information between the spike counts of two
1392 cells (Treves and Panzeri, 1995).

1393 When measuring the mutual information between clusterings we used Python, but we
1394 used the `mutual_info_score`, `adjusted_mutual_info_score`, and
1395 `normalized_mutual_info_score` functions from the `sklearn.metrics` part of
1396 the `sklearn` package.

1397 **3.3.5 Network analysis**

1398 **Correlation networks**

1399 In order to analyse functional networks created by the neurons in our ensemble, we mea-
1400 sured the total correlation between each pair of neurons. These measurements induced an

3.3. Methods

1401 undirected weighted graph/network between the neurons. The weight of each connection
1402 was equal to the total correlation between each pair of neurons.

1403 We followed the same procedure for total correlations 3.3.2, spike count correlations, and
1404 signal correlations 3.3.3.

1405 **Rectified correlations**

1406 At the time of writing, the community detection method outlined in (Humphries et al., 2019)
1407 could only be applied to networks with positively weighted connections. But many neuron
1408 pairs were negatively correlated. To apply the community detection method, we *rectified* the
1409 network, by setting all the negative weights to zero.

1410 We also looked for structure in the network created by negative correlations by reversing
1411 the signs of the correlations, and rectifying these correlations before applying our network
1412 analysis.

1413 Finally, we used the absolute value of the correlations as the weights for the graph/network.
1414 By doing this, we hoped to identify both correlated and anti-correlated functional communi-
1415 ties of neurons.

1416 **Sparsifying data networks**

1417 When creating our correlation networks, we wanted to exclude any correlations that could
1418 be judged to exist ‘by chance’. To do this, we measured the 5th and 95th percentile of
1419 the shuffled correlations (see section 3.3.2) for the given mouse and time bin width. We
1420 then set all the data correlations between these two values to 0. This excluded any ‘chance’
1421 correlations from our network, and created a sparser network. This allowed us to make use
1422 of the ‘sparse weighted configuration model’ as described in section 3.3.5.

1423 **Communities**

1424 Given some network represented by an adjacency matrix \mathbf{A} , a community within that net-
1425 work is defined as a collection of nodes where the number of connections within these nodes
1426 is higher than the expected number of connections between these nodes. In order to quan-
1427 tify the ‘expected’ number of connections, we need a model of expected networks. This is
1428 analogous to a ‘null model’ in traditional hypothesis testing. We test the hypothesis that our
1429 data network departs from the null network model to a statistically significant degree. For
1430 undirected unweighted networks, the canonical model of a null network is the configuration

1431 model (Fosdick et al., 2016). Since we are working with weighted sparse networks, we used
1432 more suitable null models, described below.

1433 **Weighted configuration model**

1434 The *weighted configuration model* is a canonical null network model for weighted networks.
1435 Given some data network, the weighted configuration model null network will preserve the
1436 degree sequence and weight sequence of each node in the data network. But the edges will
1437 be distributed randomly (Fosdick et al., 2016). Any structure in the data network beyond
1438 its degree sequence and weight sequence will not be captured in the weighted configuration
1439 model. So, this model can be used in testing the hypothesis that this extra structure exists.

1440 **Sparse weighted configuration model**

1441 The *sparse weighted configuration model* is another null network model. Similar in nature to
1442 the weighted configuration model (see section 3.3.5), but the sparsity of the data network is
1443 preserved in the null network. This is achieved by sampling from a probability distribution
1444 for the creation or non-creation of each possible connection, then distributing the weight of
1445 the data network randomly in this sparse network (Humphries et al., 2019). This is the null
1446 network that we used when searching for additional structure in our data networks.

1447 **Spectral rejection**

1448 We made use of the spectral rejection algorithm as outlined in (Humphries et al., 2019). The
1449 spectral rejection algorithm is a method for finding structure in a network not captured by a
1450 supposed null model, if such structure exists.

To describe the method, we denote our data network matrix \mathbf{W} , we denote the expected network of our null network model as $\langle \mathbf{P} \rangle$. Then the departure of our data network from the null network can be described by the matrix

$$\mathbf{B} = \mathbf{W} - \langle \mathbf{P} \rangle \quad (3.25)$$

1451 a common choice for $\langle \mathbf{P} \rangle$ in community detection is the ‘configuration model’ (Fosdick et
1452 al., 2016; Humphries, 2011). The matrix \mathbf{B} is often called the configuration matrix, in this
1453 context we will use the term ‘deviation matrix’ as it captures the deviation of \mathbf{W} from the
1454 null model.

3.3. Methods

1455 To test for structure in the network represented by \mathbf{W} , we examine the eigenspectrum of \mathbf{B}
1456 and compare it to the eigenspectrum of our null model. Firstly, note that since our data model
1457 doesn't allow self loops, and is not directed, the matrix representing the network will be
1458 symmetric and positive semi-definite, and will therefore be invertible with real eigenvalues.
1459 We selected a null model with the same characteristics.

1460 To find the eigenspectrum of the null model, we generated N samples from our null
1461 model P_1, \dots, P_N , and we measured their deviation matrices B_1, \dots, B_N . We then calculated
1462 the eigenspectrum of each of those samples. We calculated the upper bound of the null model
1463 eigenspectrum by taking the mean of the largest eigenvalues of B_1, \dots, B_N . We calculated a
1464 lower bound on the null model eigenspectrum by taking the mean of the smallest eigenvalues
1465 of B_1, \dots, B_N .

1466 We then calculated the eigenspectrum of \mathbf{B} , our data network deviation matrix. If any of
1467 those eigenvalues lay outside of the upper or lower bounds of the null model eigenspectrum,
1468 this is evidence of additional structure not captured by the null model. If we chose the sparse
1469 weighted configuration model (see section 3.3.5) as our null network model, then eigenvalues
1470 lying below the lower bound indicate k -partite structure in the network. For example, if one
1471 eigenvalue lay below the lower bound, this would indicate some bipartite structure in the data
1472 network. If any eigenvalues lay above the upper bound of the null model eigenspectrum, this
1473 is evidence of community structure in the data network. For example, one eigenvalue of \mathbf{B}
1474 lying above the upper bound of the null model eigenspectrum indicates the presence of two
1475 communities in the network (Humphries, 2011).

1476 Node rejection

1477 If there are d data eigenvalues lying outside of the null network eigenspectrum, the d eigen-
1478 vectors corresponding to these eigenvalues will form a vector space. If we project the nodes
1479 of our network into this vector space, by projecting either rows or columns of the data ma-
1480 trix, we can see how strongly each node contributes to the vector space. Nodes that contribute
1481 strongly to the additional structure will project far away from the origin, nodes that do not
1482 contribute to the additional structure will project close to the origin. We want to use this
1483 information to discard those nodes that do not contribute.

1484 We can test whether a node projects *far* away from the origin or *close* to the origin
1485 using the eigenvalues and eigenvectors of B_1, \dots, B_N . The j th eigenvector and eigenvalue
1486 of B_i gives a value for a null network's projection into the j th dimension of the additional
1487 structure vector space. The matrices B_1, \dots, B_N give N projections into that dimension.

1488 These projections are a distribution of the null networks' projections. If the data node's
1489 projection exceeds that of the null network projections this node is judged to project *far* from
1490 the origin, and therefore contribute to the additional structure. Otherwise, the node is judged
1491 to project *close* to the origin, and is therefore rejected (Humphries et al., 2019).

1492 **Community detection**

1493 Another application for this d dimensional space is community detection. We first project
1494 all of the nodes into this d -dimensional space, then perform the clustering in this space. The
1495 clustering and community detection procedure is described in (Humphries, 2011).

1496 In practice, the procedure is carried out n times (we chose $n = 100$ times), this returns n
1497 clusterings. We resolve these n clusterings to one final clustering using *consensus clustering*.
1498 We used the consensus clustering method that uses an explicit null model for the consensus
1499 matrix, as outlined in (Humphries et al., 2019).

1500 **3.3.6 Clustering Comparison**

A clustering \mathcal{C} is a partition of a set D into sets C_1, C_2, \dots, C_K , called clusters, that satisfy the following for all $k, l \in \{1, \dots, K\}$:

$$C_k \cap C_l = \emptyset \quad (3.26)$$

$$\bigcup_{k=1}^K C_k = D \quad (3.27)$$

1501 If we consider two clusterings, \mathcal{C} with clusters C_1, C_2, \dots, C_K and \mathcal{C}' with clusters
1502 C'_1, C'_2, \dots, C'_K . There are a number of measurements we can use to compare \mathcal{C} and \mathcal{C}' . In
1503 the following, the number of elements in D is denoted by n , and the number of elements in
1504 cluster C_k is n_k .

1505 **Adjusted Rand Index**

1506 The *adjusted Rand Index* is a normalised similarity measure for clusterings based on pair
1507 counting.

1508 If we consider the clusterings \mathcal{C} and \mathcal{C}' , and denote

1509 • the number of pairs in the same cluster in \mathcal{C} and \mathcal{C}' by N_{11}

1510 • the number of pairs in different clusters in \mathcal{C} and \mathcal{C}' by N_{00}

3.3. Methods

- 1511 • the number of pairs in the same cluster in \mathcal{C} and different clusters in \mathcal{C}' by N_{10}

- 1512 • the number of pairs in different clusters in \mathcal{C} and the same cluster in \mathcal{C}' by N_{01}

then the *Rand Index* is defined as

$$RI = \frac{N_{11} + N_{00}}{N_{11} + N_{00} + N_{10} + N_{01}} = \frac{N_{11} + N_{00}}{\binom{n}{2}} \quad (3.28)$$

1513 The Rand Index is 1 when the clusterings are identical, and 0 when the clusterings are com-

1514 pletely different.

The *adjusted Rand Index* intends on correcting the Rand Index for chance matching pairs.

This is defined as

$$ARI = \frac{2(N_{00}N_{11} - N_{01}N_{10})}{(N_{00} + N_{01})(N_{01} + N_{11}) + (N_{00} + N_{10})(N_{10} + N_{11})} \quad (3.29)$$

1515 The adjusted Rand Index is 1 when the clusterings are identical, and 0 when the Rand Index

1516 is equal to its expected value.

1517 Clusterings as random variables

If we take any random element of D , the probability that this element is in cluster C_k of clustering \mathcal{C} is

$$P(K = k) = \frac{n_k}{n} \quad (3.30)$$

1518 this defines a probability distribution, which makes the clustering a random variable. Any

1519 clustering can be considered as a random variable this way.

This means that we can measure any of the information theoretic quantities defined in section 3.3.4 with respect to clusterings. For example, the entropy of a clustering is

$$H(\mathcal{C}) = - \sum_{k=1}^K \frac{n_k}{n} \log \frac{n_k}{n} \quad (3.31)$$

If we have two clusterings, the joint probability distribution of these clusterings is defined as

$$P(K = k, K' = k') = \frac{|C_k \cap C'_{k'}|}{n} \quad (3.32)$$

1520 The joint distribution allows us to define the mutual information between two clusterings,

1521 $I(\mathcal{C}; \mathcal{C}')$ (Meilă, 2007).

1522 **Information based similarity measures**

The mutual information between two clusterings is a similarity measure, with $I(\mathcal{C}; \mathcal{C}') = 0$ if \mathcal{C} and \mathcal{C}' are completely different, and $I(\mathcal{C}; \mathcal{C}') = H(\mathcal{C}) = H(\mathcal{C}')$ if \mathcal{C} and \mathcal{C}' are identical. This can be normalised in a number of different ways to make more similarity measures (Vinh, Epps, and Bailey, 2010)

$$NMI_{joint} = \frac{I(\mathcal{C}; \mathcal{C}')}{H(\mathcal{C}, \mathcal{C}')} \quad (3.33)$$

$$NMI_{max} = \frac{I(\mathcal{C}; \mathcal{C}')}{\max\{H(\mathcal{C}), H(\mathcal{C}')\}} \quad (3.34)$$

$$NMI_{sum} = \frac{2I(\mathcal{C}; \mathcal{C}')}{H(\mathcal{C}) + H(\mathcal{C}')} \quad (3.35)$$

$$NMI_{sqrt} = \frac{I(\mathcal{C}; \mathcal{C}')}{\sqrt{H(\mathcal{C})H(\mathcal{C}')}} \quad (3.36)$$

$$NMI_{min} = \frac{I(\mathcal{C}; \mathcal{C}')}{\min\{H(\mathcal{C}), H(\mathcal{C}')\}} \quad (3.37)$$

We can control for chance similarities between the two clusterings by measuring the *adjusted mutual information* between the clusterings. This is defined as

$$AMI_{sum} = \frac{I(\mathcal{C}; \mathcal{C}') - E\{I(\mathcal{C}; \mathcal{C}')\}}{\frac{1}{2}[H(\mathcal{C}) + H(\mathcal{C}')] - E\{I(\mathcal{C}; \mathcal{C}')\}} \quad (3.38)$$

1523 The first term in the denominator, taking the average of the marginal entropies, can be re-
1524 placed by taking the maximum, minimum, or the geometric mean (Vinh, Epps, and Bailey,
1525 2010).

1526 **Information based metrics**

The variation of information between two clusterings $VI(\mathcal{C}; \mathcal{C}')$ (see section 3.3.4) is a metric on the space of clusterings (Meilă, 2007). That is,

$$VI(\mathcal{C}; \mathcal{C}') \geq 0 \quad (3.39)$$

$$VI(\mathcal{C}; \mathcal{C}') = 0 \iff \mathcal{C} = \mathcal{C}' \quad (3.40)$$

$$VI(\mathcal{C}; \mathcal{C}') = VI(\mathcal{C}'; \mathcal{C}) \quad (3.41)$$

$$VI(\mathcal{C}; \mathcal{C}'') \leq VI(\mathcal{C}; \mathcal{C}') + VI(\mathcal{C}'; \mathcal{C}'') \quad (3.42)$$

3.4. Results

Another metric is the *information distance* (Vinh, Epps, and Bailey, 2010)

$$D_{max} = \max\{H(\mathcal{C}), H(\mathcal{C}')\} - I(\mathcal{C}; \mathcal{C}') \quad (3.43)$$

Both of these can be normalised

$$NVI(\mathcal{C}; \mathcal{C}') = 1 - \frac{I(\mathcal{C}; \mathcal{C}')}{H(\mathcal{C}, \mathcal{C}')} \quad (3.44)$$

$$d_{max} = 1 - \frac{I(\mathcal{C}; \mathcal{C}')}{\max\{H(\mathcal{C}), H(\mathcal{C}')\}} \quad (3.45)$$

1527 Comparing detected communities and anatomical divisions

1528 In order to quantify the difference or similarity between the communities detected in our
1529 correlation network and the anatomical classification of the cells in that network, we considered
1530 the communities and the anatomical regions as clusters in two different clusterings, \mathcal{C}_{comm}
1531 and \mathcal{C}_{anat} , respectively. We then measured the similarity between the clusterings using the
1532 mutual information, the adjusted mutual information, and the normalised mutual informa-
1533 tion. We measured the difference between, or the distance between, the clusterings using the
1534 variation of information, the normalised variation of information, and the normalised infor-
1535 mation distance. We also measured the difference between the clusterings using the adjusted
1536 Rand Index, just to use a non-information based measure.

1537 We took all of these measures for communities detected using different time bin widths.
1538 This gave us an idea of the effect of time bin width on correlation networks in neural ensem-
1539 bles relative to anatomical regions within those ensembles.

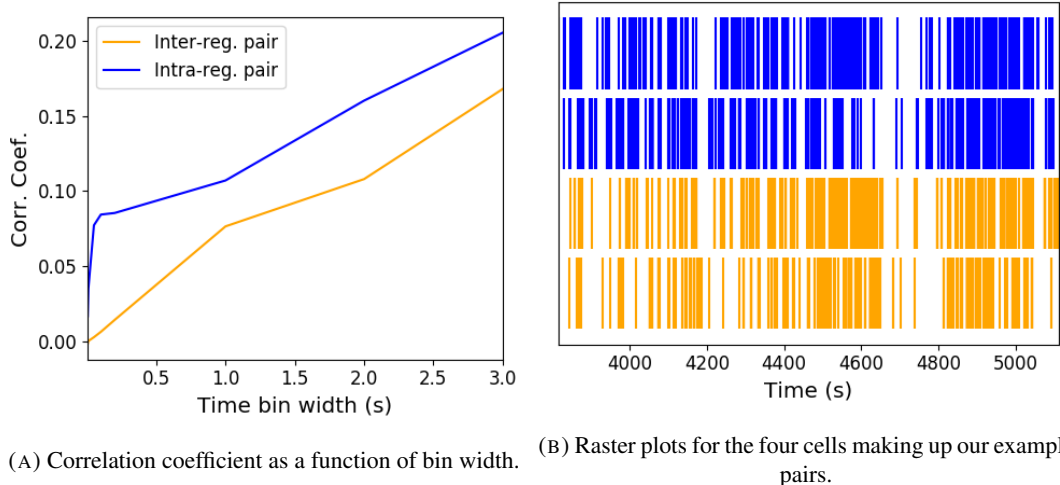
1540 3.4 Results

1541 Note that in the following text, we refer to the correlation coefficient between two sequences
1542 of spike counts from two different cells as the *total correlation*. We refer to the correlation
1543 between spike counts in response to a certain stimulus as the *spike count correlation* aka
1544 *noise correlation*, and we refer to the correlation between mean or expected responses to
1545 different stimuli as the *signal correlation* (Cohen and Kohn, 2011).

1546 The nine different brain regions from which we had data were the caudate putamen (CP),
1547 frontal motor cortex (FrMoCtx), hippocampus (HPF), lateral septum (LS), midbrain (MB),
1548 primary visual cortex (V1), superior colliculus (SC), somatomotor cortex (SomMoCtx), and
1549 thalamus (TH).

1550 **3.4.1 Average correlation size increases with increasing time bin width**

1551 First we inspected the affect of time bin width on total correlations. We know that using short
 1552 time bins results in artificially small correlation measurements (Cohen and Kohn, 2011), so
 1553 we expected to see an increase in correlation amplitude with increasing time bin width. That
 1554 is exactly what we observed. Taking 50 cells at random, we calculated the total correla-
 1555 tion between every possible pair of these cells, using different time bin widths ranging from
 1556 0.005s to 3s. We found that the longer the time bin width, the greater the correlations (see
 1557 figure 3.4a).



(A) Correlation coefficient as a function of bin width. (B) Raster plots for the four cells making up our example pairs.

FIGURE 3.3: (A) An example of the correlation coefficients between two different pairs of cells, one where both cells are in the same brain region (intra-regional pair), and one where both cells are in different brain regions (inter-regional pair). The correlation coefficients have been measured using different time bin widths, ranging from 5ms to 3s. Note the increasing amplitude of the correlations with increasing bin width. (B) A raster plot showing the spike times of each pair of cells.

1558 We also separated the positively correlated pairs from the negatively correlated pairs
 1559 using the mean correlation of each pair across all bin widths (see section 3.3.2). We found
 1560 that the positively correlated pairs become more positively correlated with increasing time bin
 1561 width, and the negatively correlated pairs become more negatively correlated with increasing
 1562 time bin width (see figures 3.4b and 3.4c).

1563 In figure 3.3a we plot correlations from two example pairs, one pair from within a region,
 1564 and one pair between regions. It can be seen that the correlation coefficient increases with
 1565 bin width. The correlations can be observed by eye in the raster plot for these cells in figure
 1566 3.3b.

1567 When taking the mean across all pairs, the positively correlated pairs dominate in terms
 1568 of both number of pairs, and amplitude of correlations. Therefore the mean across all pairs

3.4. Results

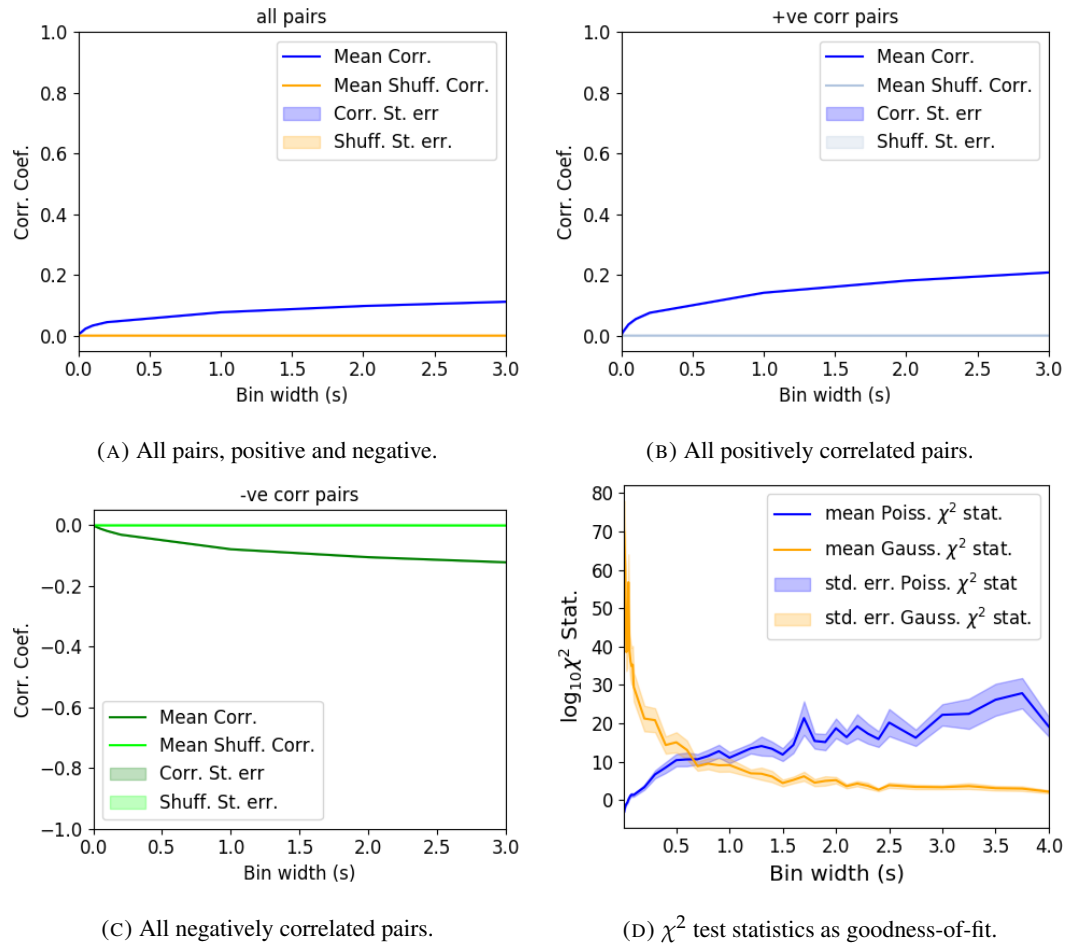


FIGURE 3.4: Mean correlation coefficients measured from pairs of 50 randomly chosen neurons. (A) All possible pairs, (B) positively correlated pairs, and (C) negatively correlated pairs. (D) Mean and standard error of χ^2 test statistics for Poisson and Gaussian distributions fitted to neuron spike counts.

1569 is positive.

1570 These results were observed in each of the three mouse subjects from which we had data.

1571 **3.4.2 Goodness-of-fit for Poisson and Gaussian distributions across increasing
1572 time bin widths**

1573 We wanted to investigate if the width of the time bin used to bin spike times into spike counts
1574 had an effect on the distribution of spike counts. We used the χ^2 statistic as a goodness-of-fit
1575 measure for Poisson and Gaussian (normal) distributions to the spike count of 100 randomly
1576 chosen neurons for a number of bin widths ranging from 0.01s to 4s. For the χ^2 statistic, the
1577 higher the value, the worse the fit.

1578 We expected a Poisson distribution to be a better fit for shorter time bin widths because
1579 spike counts must be non-negative, therefore any distribution of spike counts with mass dis-
1580 tributed at or close to 0 will be skewed. The distribution of spike counts is more likely to be
1581 distributed close to 0 when the time bin widths used to bin spike times into spike counts are
1582 small relative to the amount of time it takes for a neuron to fire an action potential ($\sim 1\text{ms}$ in
1583 the case of non-burst firing neurons).

1584 We expected a Gaussian distribution to be a better fit for longer time bin widths, because
1585 a Poisson distribution with a large rate is well approximated by a Gaussian distribution with
1586 mean and variance equal to the Poisson rate. Therefore, a Gaussian distribution would ap-
1587 proximate the mean of a collection of large spike counts, and have more flexibility than a
1588 Poisson distribution to fit the variance.

1589 We found that that a Poisson distribution is the best fit for shorter time bins less than 0.7s
1590 in length. Then a Gaussian distribution is a better fit for time bins greater than 0.7s in length
1591 (see figure 3.4d).

1592 **3.4.3 Differences between and inter- and intra- regional correlations decrease
1593 with increasing bin width**

1594 We investigated the differences in distribution between inter-regional correlations, i.e. corre-
1595 lations between neurons in different brain regions, and intra-regional correlations, i.e. corre-
1596 lations between neurons in the same brain region.

1597 Firstly, we investigated these quantities for all possible pairs of ~ 500 neurons taken
1598 from across all the 9 brain regions from which we had data. We distributed these neurons as
1599 evenly as possible across all of the regions, so that cells from one region would not dominate
1600 our data. We observed that the mean intra-regional correlations were always higher than the

3.4. Results

mean inter-regional correlations for every value of time bin width used. We also observed that as the time bin width increased these mean correlations increased and the difference between the mean inter-regional and intra-regional correlations grew (see figure 3.5 (Left)).

Stringer et al. (2019) had a similar finding using the same data. They used only one value for the time bin width, 1.2s. Using this time bin width to bin spike times and measure total correlations, they found that the mean ‘within-region’ correlations were always greater than the ‘out-of-region’ correlations (Stringer et al., 2019). The figure from their paper showing this result can be seen in figure 3.5 (Right).

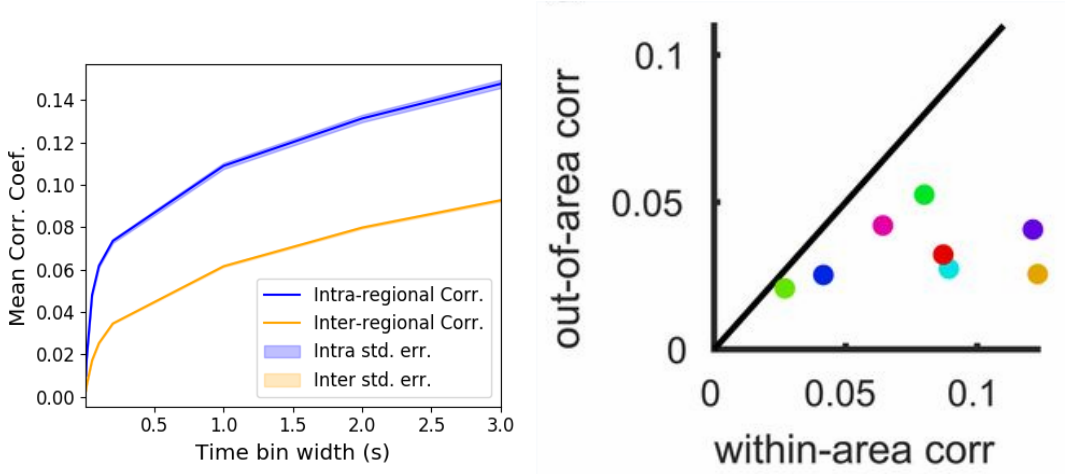
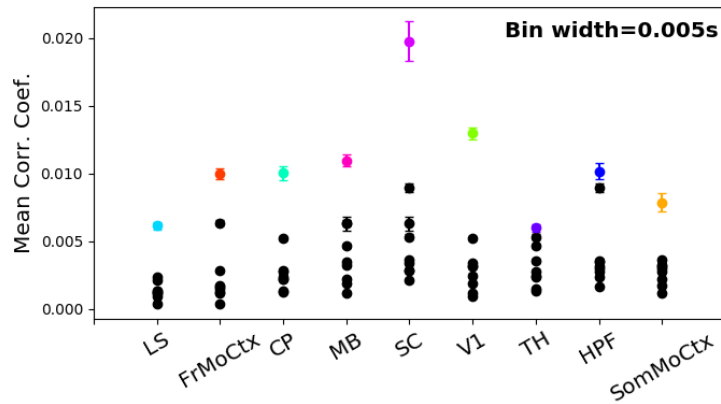


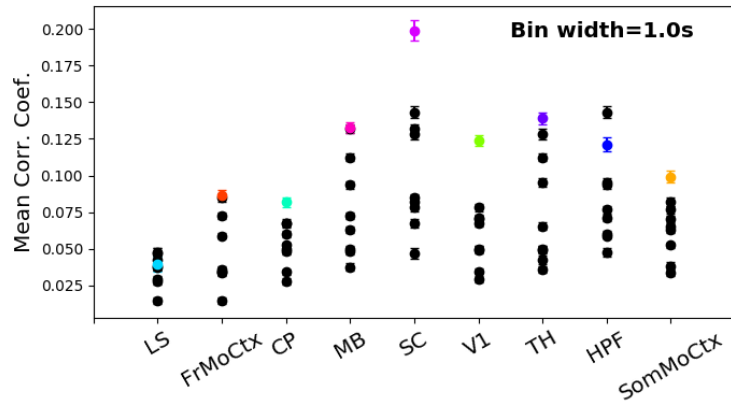
FIGURE 3.5: (Left)The mean intra-region and inter-region correlations using all possible pairs of ~ 500 neurons, spread across 9 different brain regions. (Right) Courtesy of Stringer et al. (2019), mean inter-regional (out-of-area) correlation coefficients vs mean intra-regional (within-area) correlation coefficients for a bin width of 1.2s. Note that the intra-regional coefficients are higher in each case.

Examples of the correlations of one intra-regional pair and one inter-regional pair can be seen in figure 3.3.

Secondly, we separated those pairs into intra-regional and inter-regional groups. We noted that the mean intra-regional correlations (coloured dots in figures 3.6a and 3.6b) for a given region tended to be higher than the mean inter-regional correlations (black dots in figures 3.6a and 3.6b) involving cells from that region. However, in contrast with our previous result, we noted that the difference between the mean intra-regional correlations and most highly correlated inter-regional correlations reduced as we increased the time bin width (see figures 3.6a and 3.6b). This shows that the mean correlations shown in figure 3.5 are not distributed evenly across all region pair combinations.



(A) Mean inter-regional and intra-regional correlations using a time bin width of 5ms.



(B) Mean inter-regional and intra-regional correlations using a time bin width of 1s.

FIGURE 3.6: The mean intra-regional correlations (coloured dots) and mean inter-regional correlations (black dots) for a given region, indicated on the x-axis, for different time bin widths. Each black dot represents the mean inter-regional correlations between the region indicated on the x-axis and one other region. (A) shows these measurements when we used a time bin width of 5ms. (B) shows these measurements when we used a time bin width of 1s. Note that the difference between the mean inter-regional correlations and mean intra-regional correlations is smaller for 1s bins.

3.4. Results

Finally, to see these regional mean correlations in a bit more detail, to examine the individual pair combinations in particular, we displayed these data in a matrix of mean correlations (see figure 3.7), showing the mean intra-regional correlations on the main diagonal, and the mean inter-regional correlations off diagonal. Comparing a version of this figure created using a short time bin width of 5ms (figure 3.7a) and a version using a longer time bin width of 1s (figure 3.7b) we observed that the mean intra-regional correlations are always relatively high in comparison to the mean inter-regional correlations, but the mean correlations in some inter-regional pairs are relatively much higher when using the longer time bin width.

This could indicate information being processed quickly at a local or within-region level, and the local representations of this information spreading between regions at longer timescales.

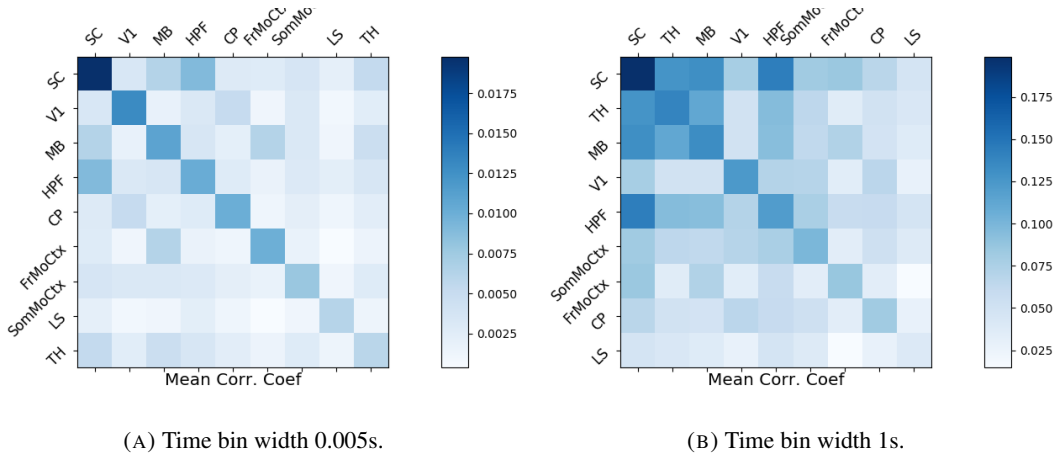


FIGURE 3.7: Mean inter-regional (main diagonal) and intra-regional (off diagonal) correlation coefficients. (A) Shows these measurements when spike times were binned using 5ms time bins. (B) Shows the same, using 1s time bins. Note that the matrices are ordered according to the main diagonal values, therefore the ordering is different in each subfigure.

These results were consistent across the three mouse subjects. But, the relative magnitudes of the mean intra-regional and inter-regional correlations were not consistent. For example, the region with the highest mean intra-regional correlations when using 1s bin widths for subject one is the superior colliculus (SC), but for subject two it is the midbrain (MB).

3.4.4 Connected and divided structure in correlation based networks reduces in dimension with increasing bin width

We used the correlation measurements to create weighted undirected graphs/networks where each node represents a neuron, and the weight of each edge is the pairwise correlation between those neurons represented by the nodes at either end of that edge. We aimed to find

1638 communities of neurons within these networks, and compare the structure of these commu-
1639 nities to the anatomical division of those neurons. The first step of this process involved
1640 applying the ‘spectral rejection’ technique developed by Humphries et al (2019) (Humphries
1641 et al., 2019). This technique compares our data network to a chosen null network model, and
1642 finds any additional structure in the data network beyond that which is captured in the null
1643 network model (if there is any such structure).

1644 By comparing the eigenspectrum of the data network to the eigenspectrum of many sam-
1645 ples from the null network model, this technique allows us to estimate the dimensionality of
1646 the additional structure in the data network, and gives us a basis for that vector space. It also
1647 divides the additional structure into connected structure, and k -partite (or divided) structure.
1648 For example, if our algorithm found two dimensions of additional connected structure, and
1649 one dimension of additional divided structure. We might expect to find three communities,
1650 that is groups more strongly connected within group than without, and we might expect to
1651 find bi-partite structure, that is two sets that are more strongly connected between groups
1652 than within groups.

1653 The technique also finds which nodes contribute to this additional structure, and divides
1654 our data network into signal and noise networks. The details of spectral rejection and node
1655 rejection can be found in sections 3.3.5 and 3.3.5 respectively, and a full overview can be
1656 found in (Humphries et al., 2019).

1657 We chose the sparse weighted configuration model (see section 3.3.5) as our null network
1658 model. This model matches the sparsity and the total weight of the original network but
1659 distributes the weight at random across the sparse network.

1660 We applied the spectral rejection method to our networks based on total correlations using
1661 different values for the time bin width. We observed that for smaller time bin widths, our data
1662 networks had both k -partite structure, and community structure. As the width of the time bin
1663 increased, we found that the k -partite structure disappeared from our data networks, and the
1664 dimension of the community structure reduced in two of the three mice from which we had
1665 data (see figure 3.8).

1666 3.4.5 Detecting communities in correlation based networks

1667 We applied the community detection procedure described in section 3.3.5 to our signal net-
1668 works for our various time bin widths. We detected a greater number of smaller communities
1669 at shorter time bin widths, and a smaller number of larger communities for longer time bin
1670 widths (see figure 3.9). This was expected after the results found in section 3.4.4. We found

3.4. Results

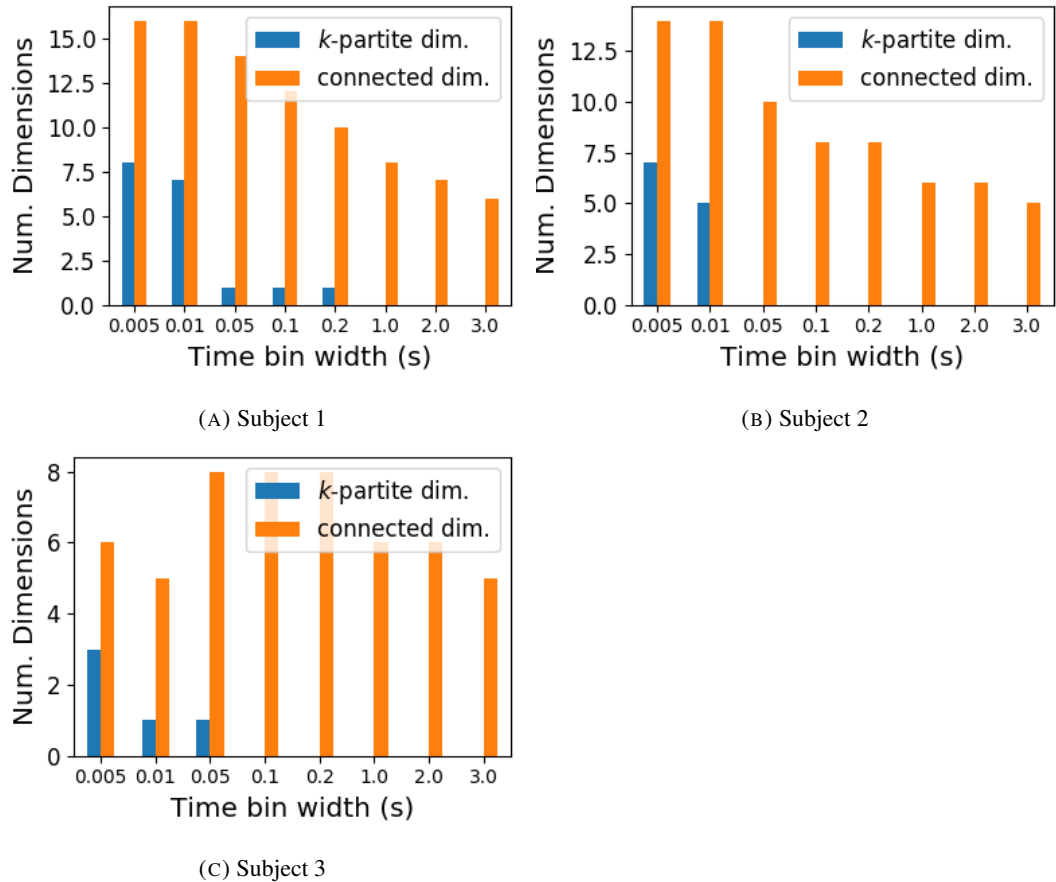


FIGURE 3.8: The number of dimensions in the *k*-partite and connected structure in the correlation based networks beyond the structure captured by a sparse weighted configuration null network model (see section 3.3.5), shown for different time bin widths. Note that the *k*-partite structure disappears for time bin width greater than 200ms for all three subjects. The dimension of the connected structure reduces with increasing bin width for 2 of the 3 subjects (top row).

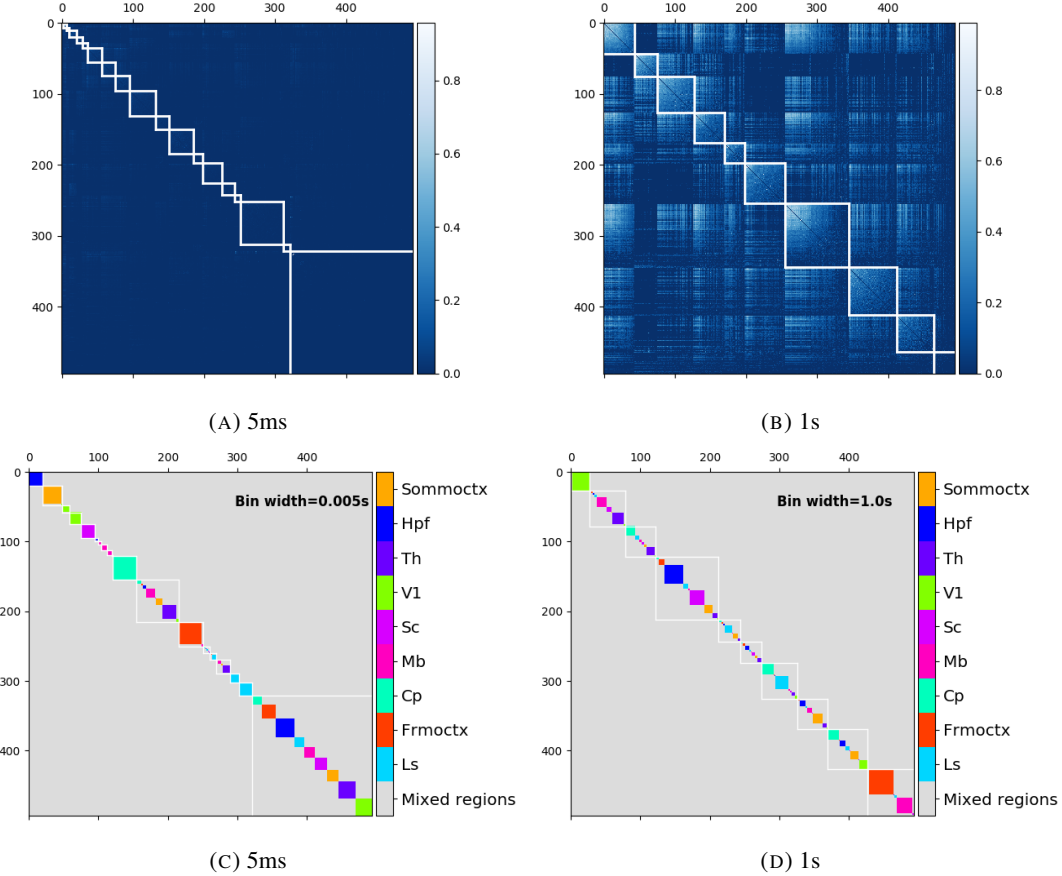


FIGURE 3.9: (A-B) Correlation matrices with detected communities indicated by white lines. Each off main diagonal entry in the matrix represents a pair of neurons. Those entries within a white square indicate that both of those neurons are in the same community as detected by our community detection procedure. Matrices shown are for 5ms and 1s time bin widths respectively. Main diagonal entries were set to 0. (C-D) Matrices showing the anatomical distribution of pairs along with their community membership. Entries where both cells are in the same region are given a colour indicated by the colour bar. Entries where cells are in different regions are given the grey colour also indicated by the colour bar.

3.4. Results

more dimensions of additional structure at shorter time bin widths, therefore we found more communities at shorter time bin widths.

We also noticed that at short time bin widths the communities detected tended to be dominated by cells from one region. Whereas communities existing in networks created using wider time bin widths tended to contain cells from many different brain regions. More on this in the next section.

3.4.6 Functional communities resemble anatomical division at short timescales

In order to quantify the similarity of the communities detected to the anatomical division of the cells. We treated both the anatomical division and the communities as clusterings of these cells. We then used measures for quantifying the difference or similarity between clusterings to quantify the difference or similarity between the detected communities and the anatomical division. Details of these measures can be found in section 3.3.6 or in (Vinh, Epps, and Bailey, 2010).

We used two different types of measures for clustering comparison; information based measures (see section 3.3.6) and pair counting based measures (see section 3.3.6). We include one example of each in figure 3.10.

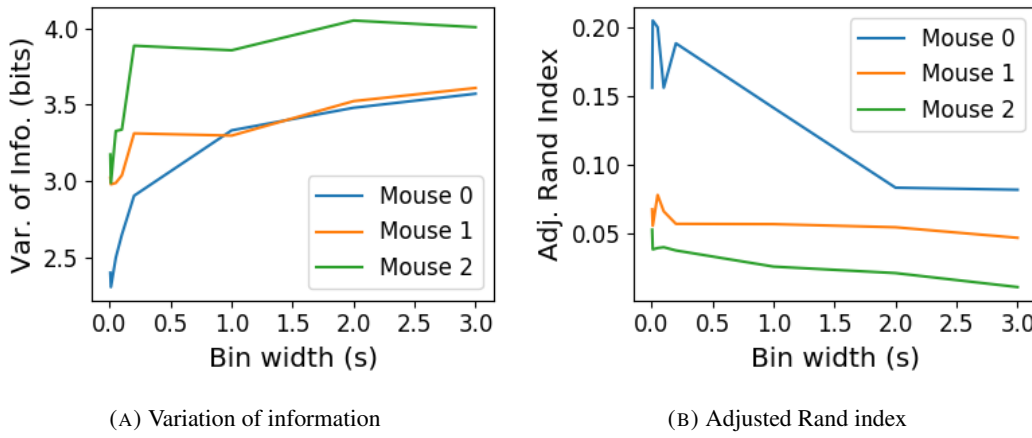
The variation of information is the information based measure included in figure 3.10a. This measure forms a metric on the space of clusterings. The larger the value for the variation of information, the more different the clusterings.

The adjusted Rand index is the pair counting based measure included in figure 3.10b. In contrast with the variation of information, the adjusted Rand index is a normalised similarity measure. The adjusted Rand index takes value 1 when the clusterings are identical, and takes value 0 when the clusterings are no more similar than chance.

Both measures indicated that the detected communities and the anatomical division of the cells were more similar when we used shorter time bins widths (see figure 3.10). This indicates that correlated behaviour in neuronal ensembles is more restricted to individual brain regions at short timescales (< 250ms), and the correlated activity spreads out across brain regions over longer time scales.

3.4.7 Conditional correlations & signal correlations

In light of the excellent research of Stringer et al (2019) showing that spontaneous behaviours can drive activity in neuronal ensembles across the visual cortex and midbrain (Stringer et al., 2019), we decided to control for the mouse's behaviour when performing our analyses.



(A) Variation of information

(B) Adjusted Rand index

FIGURE 3.10: (A) The variation of information is a measure of distance between clusterings. The distance between the anatomical ‘clustering’ and community detection ‘clustering’ increases with increasing time bin width. (B) The adjusted Rand index is a normalised similarity measure between clusterings. The anatomical and community detection clusterings become less similar as the time bin width increases.

1703 It is possible that our community detection process may be detecting communities across
 1704 multiple brain regions at longer time scales due to aggregating neuronal activity driven by
 1705 several spontaneous behaviours occurring during the time interval covered by a given time
 1706 bin. A time bin of 1s, for example, could contain a spike count where those spikes were driven
 1707 by different spontaneous behaviours. We aimed to investigate this possibility by applying our
 1708 community detection analysis to conditional correlation measures.

1709 We used the top 500 principal components of a video of the mouse’s face as a measure of
 1710 the mouse’s behaviour (see section 3.2.2). We modelled the spike counts as a linear combi-
 1711 nation of the principal components using linear regression with ElasticNet regularisation (see
 1712 section 3.3.3). Using this model, we quantified the expected spike count given the mouse’s
 1713 behaviour $E[X|Z_1, \dots, Z_{500}]$.

1714 We used these expected values to measure $\text{cov}(E[X|Z], E[Y|Z])$, and we used that value,
 1715 the covariance $\text{cov}(X, Y)$, and the *law of total covariance* (see section 3.3.3) to measure
 1716 $E[\text{cov}(X, Y|Z)]$. Here X and Y represent spike counts from individual cells, and Z is short-
 1717 hand for the 500 principal components mentioned above. The two components of the co-
 1718 variance, $\text{cov}(E[X|Z], E[Y|Z])$ and $E[\text{cov}(X, Y|Z)]$, represent a ‘signal covariance’ and ex-
 1719 pected value of a ‘spike count covariance’ respectively, analogous to the signal correlation
 1720 and spike count correlation (Cohen and Kohn, 2011).

1721 We examined the means of these components for different values of the time bin width
 1722 (see figure 3.11). We observed a consistent increase in $E[\text{cov}(X, Y|Z)]$ as the time bin width
 1723 increased. But we saw different trends for $\text{cov}(E[X|Z], E[Y|Z])$ for each mouse.

3.4. Results

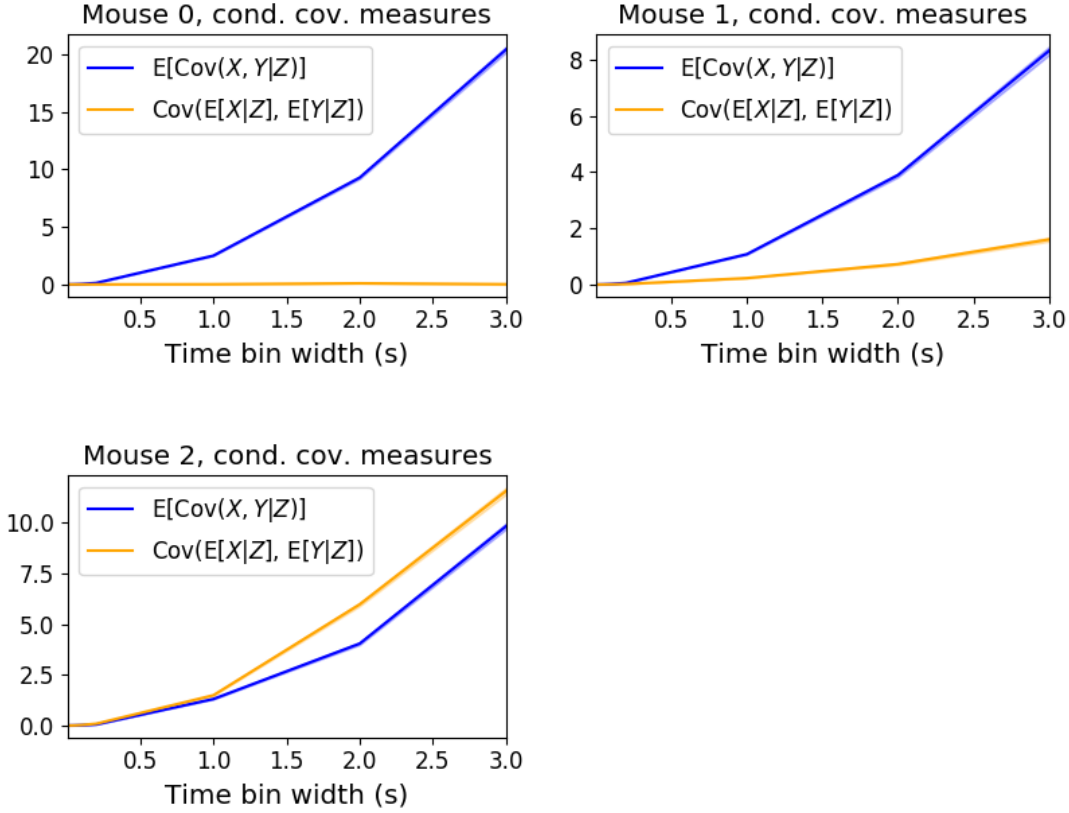


FIGURE 3.11: Comparing the components of the total covariance across different values for the time bin width. We observed a consistent increase in $E[\text{cov}(X, Y|Z)]$ as the time bin width increased. But we saw different trends for $\text{cov}(E[X|Z], E[Y|Z])$ for each mouse.

1724 Using $\text{cov}(E[X|Z], E[Y|Z])$ we measured the signal correlation, ρ_{signal} , and using $E[\text{cov}(X, Y|Z)]$
 1725 we measured the event conditional correlation, $\rho_{X,Y|Z}$ (see section 3.3.3 for more details).
 1726 We saw a consistent increase in $\rho_{X,Y|Z}$ as the time bin width increased, this corresponds to
 1727 the result for $E[\text{cov}(X, Y|Z)]$. We observed different trends for ρ_{signal} for each mouse, this
 1728 corresponds to the result for $\text{cov}(E[X|Z], E[Y|Z])$.

1729 We applied our network noise rejection and community detection process to networks
 1730 based on the spike count correlations $\rho_{X,Y|Z}$ and the signal correlations ρ_{signal} . We noted that
 1731 the community detection on $\rho_{X,Y|Z}$ behaved similarly to the community detection on the total
 1732 correlation. We can see this in figures 3.13a and 3.13b. At very short time bin widths, we
 1733 detect more communities, and those communities often contain cells from one brain region
 1734 only. At longer time bin widths, we detect fewer communities, and those communities tend
 1735 to contain cells from multiple brain regions. When we examine the distance between (or
 1736 similarity between) the anatomical division of the cells, and the detected communities we
 1737 notice that the two clusterings are more similar at shorter time bin widths (see figure 3.14).

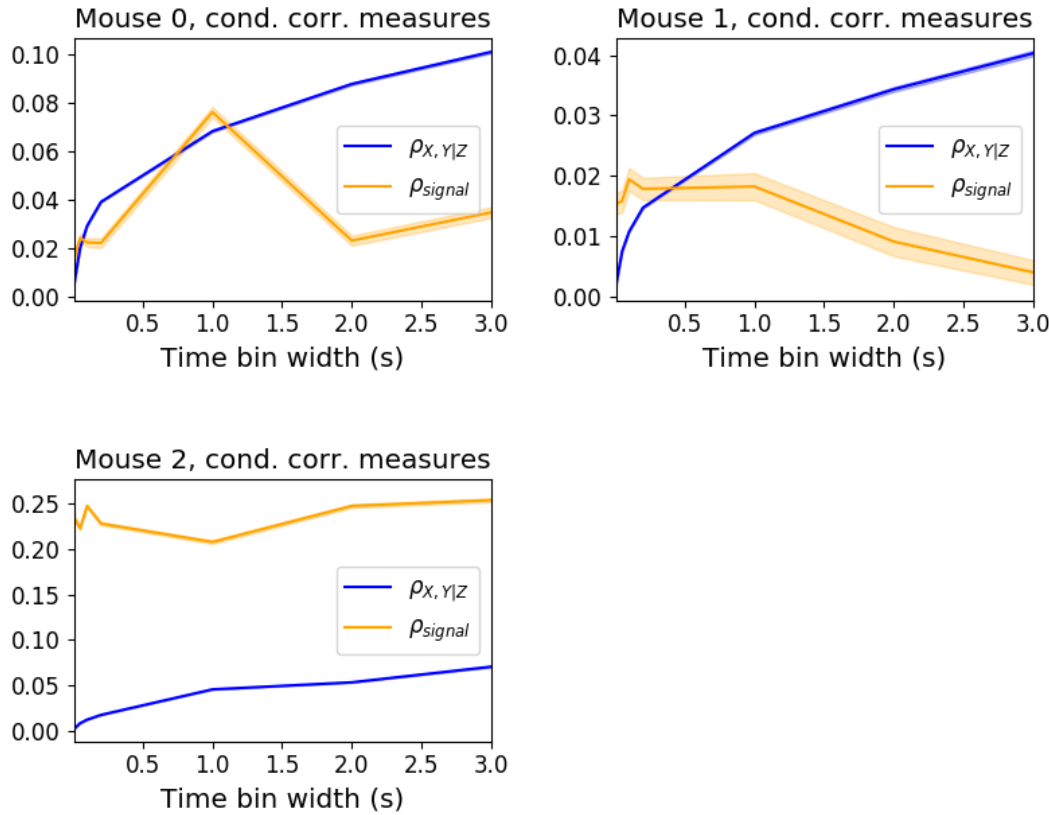


FIGURE 3.12: Comparing the components of the total covariance across different values for the time bin width. We saw a consistent increase in $\rho_{X,Y|Z}$ as the time bin width increased in all three subjects. But we saw different trends in ρ_{signal} for each of the subjects.

When we applied the network noise rejection and community detection process to the networks based on the signal correlations ρ_{signal} we found the number of communities we detected reduced with increasing time bin width. But the number of communities detected was less than that for the total correlations or the spike count correlations. The communities detected always tended to contain cells from multiple regions at both short and long timescales (see figures 3.13c and 3.13d). The communities detected bore very little relation to the anatomical division of the cells. The adjusted Rand index between the community clustering and the anatomical ‘clustering’ is close to zero for every time bin width (see figure 3.15b). This indicates that the similarity between the clusterings is close to chance. We did observe a slight downward trend in the variation of information with increasing bin width (see figure 3.15a), but this is more likely due to a decrease in the number of communities detected rather than any relationship with anatomy.

We also observed that the network noise rejection process rejected some of the cells when applied to the network based on the signal correlations. This means that those cells

3.4. Results

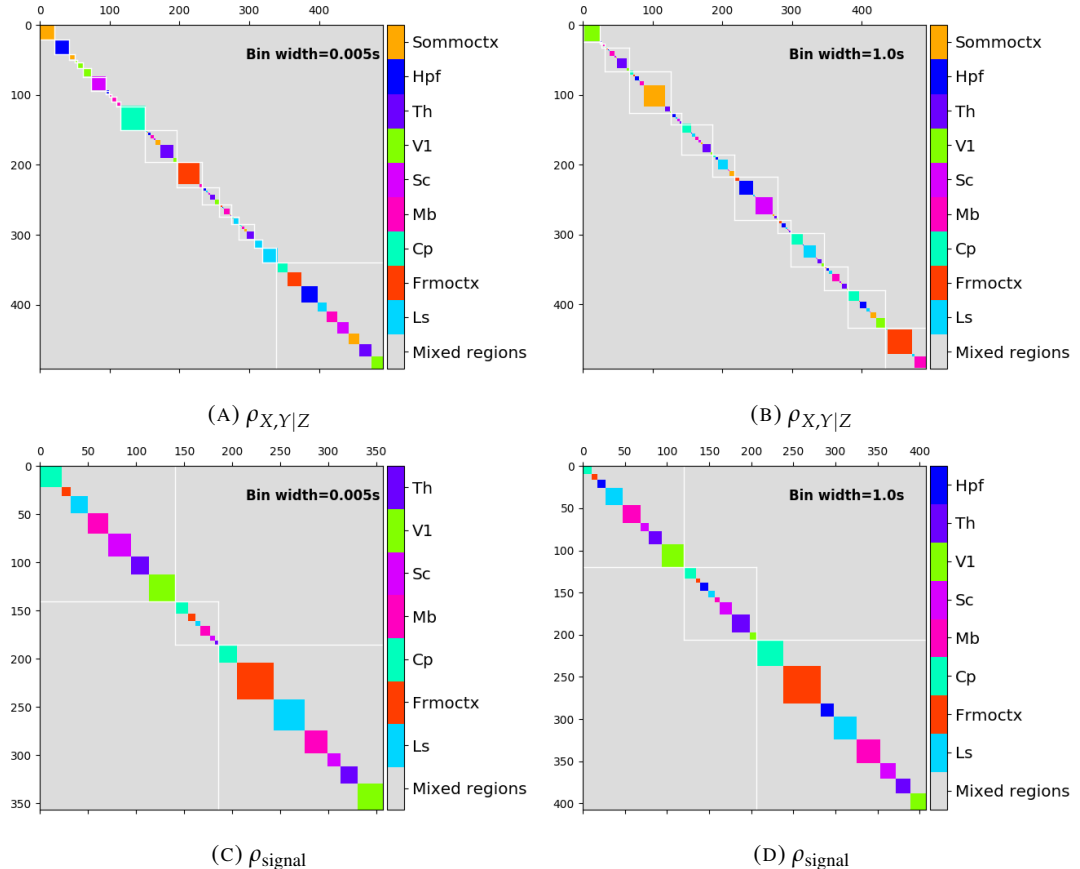


FIGURE 3.13: Matrices showing the regional membership of pairs by colour, and the communities in which those pairs lie. (A-B) Detected communities and regional membership matrix for network based on rectified spike count correlation $\rho_{X,Y|Z}$, using time bin widths of 0.005s and 1s respectively. (C-D) Detected communities and regional membership matrix for network based on rectified signal correlation ρ_{signal} , using time bin widths of 0.005s and 1s respectively.

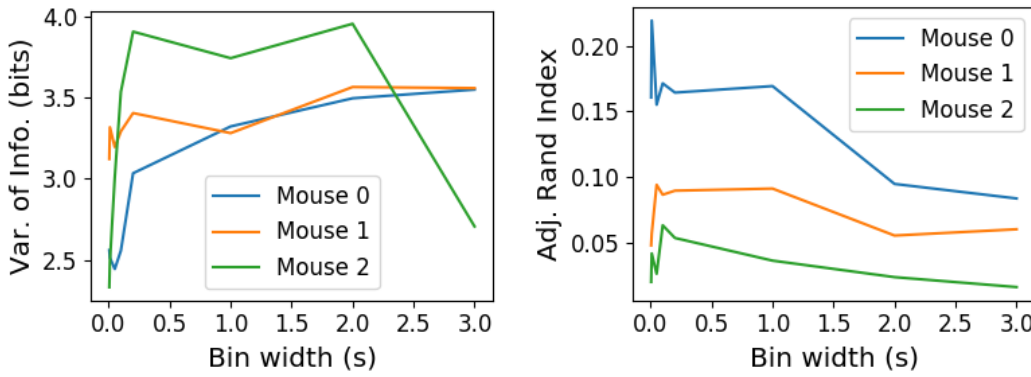
(A) $\rho_{X,Y|Z}$ Variation of information.(B) $\rho_{X,Y|Z}$ Adjusted Rand Index.

FIGURE 3.14: Distance and similarity measures between the anatomical division of the neurons, and the communities detected in the network based on the spike count correlations $\rho_{X,Y|Z}$. (A) The variation of information is a ‘distance’ measure between clusterings. The distance between the anatomical ‘clustering’ and the community clustering increases as the time bin width increases. (B) The adjusted Rand index is a similarity measure between clusterings. The detected communities become less similar to the anatomical division of the cells as the time bin width increases.

1752 did not contribute to the additional structure of the network beyond that captured by the
 1753 sparse weighted configuration model. This is why the matrices in figures 3.13c and 3.13d are
 1754 smaller than their analogues in figures 3.13a and 3.13b.

1755 3.4.8 Absolute correlations and negative rectified correlations

1756 At the moment, the network noise rejection protocol can only be applied to weighted undi-
 1757 rected graphs with non-negative weights. This meant that we had to rectify our correlated
 1758 networks before applying the network noise rejection and community detection process. We
 1759 wanted to investigate what would happen if instead of rectifying the correlations, we used the
 1760 absolute value, or reversed the signs of the correlations and then rectified.

1761 When we used the absolute value of the correlations, we found very similar results to
 1762 those shown above for the rectified total correlations and the rectified spike count corre-
 1763 lations. We detected more communities using shorter bin widths, and these communities
 1764 were more similar to the brain’s anatomy than those communities detected using a longer bin
 1765 width (see figure 3.16). The only exception being that we detected more communities. This
 1766 could indicate that we detected both positively and negatively correlated communities, but
 1767 we haven’t done any further investigation so we cannot say for sure.

1768 When we used the sign reversed rectified correlated networks, we tended to find fewer
 1769 communities. Each community contained cells from many different anatomical regions, at

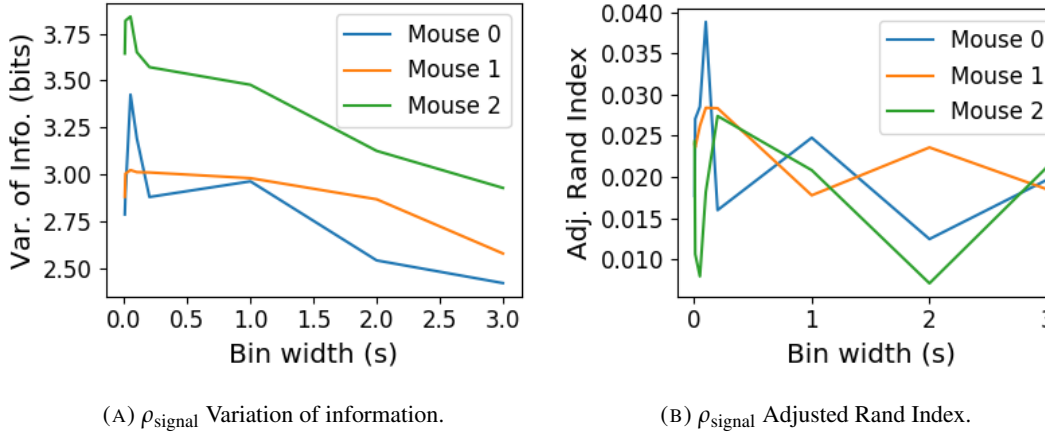


FIGURE 3.15: Distance and similarity measures between the anatomical division of the neurons, and the communities detected in the network based on the signal correlations ρ_{signal} . (A) The variation of information is a ‘distance’ measure between clusterings. The distance between the anatomical ‘clustering’ and the community clustering increases as the time bin width increases. (B) The adjusted Rand index is a similarity measure between clusterings. The detected communities become less similar to the anatomical division of the cells as the time bin width increases.

1770 both long and short bin widths (see figures 3.17a, 3.17b, 3.17c, 3.17d). The communities
 1771 bore little relation to the anatomical distribution of the cells, this can be seen in figure 3.17f,
 1772 the values close to zero indicate that the similarity between the two clusterings are around
 1773 chance level. This indicates that there was not much structure in the negatively correlated
 1774 networks beyond that captured by the sparse weighted configuration model.

3.5 Discussion

1776 It is well established that the brain uses correlated behaviour in neuronal ensembles to repre-
 1777 sent the information taken in through sensation (Cohen and Maunsell, 2009; Litwin-Kumar,
 1778 Chacron, and Doiron, 2012; deCharms and Merzenich, 1996). However, most studies that
 1779 examine the nature of these correlations in-vivo, study an ensemble of cells from only one
 1780 or two brain regions (Cohen and Kohn, 2011; Wierzynski et al., 2009; Patterson et al., 2014;
 1781 Girard, Hupé, and Bullier, 2001). Furthermore, recent results have shown that behaviour can
 1782 drive correlated activity in multiple brain regions, including those not normally associated
 1783 with motor control (Stringer et al., 2019; Gründemann et al., 2019; Allen et al., 2019). In this
 1784 study, we utilised one of the newly recorded large datasets containing electrophysiological
 1785 recordings from multiple brain regions simultaneously. We investigated correlated behaviour
 1786 in these different brain regions and we investigated correlated behaviour between neurons in
 1787 different regions, during spontaneous behaviour.

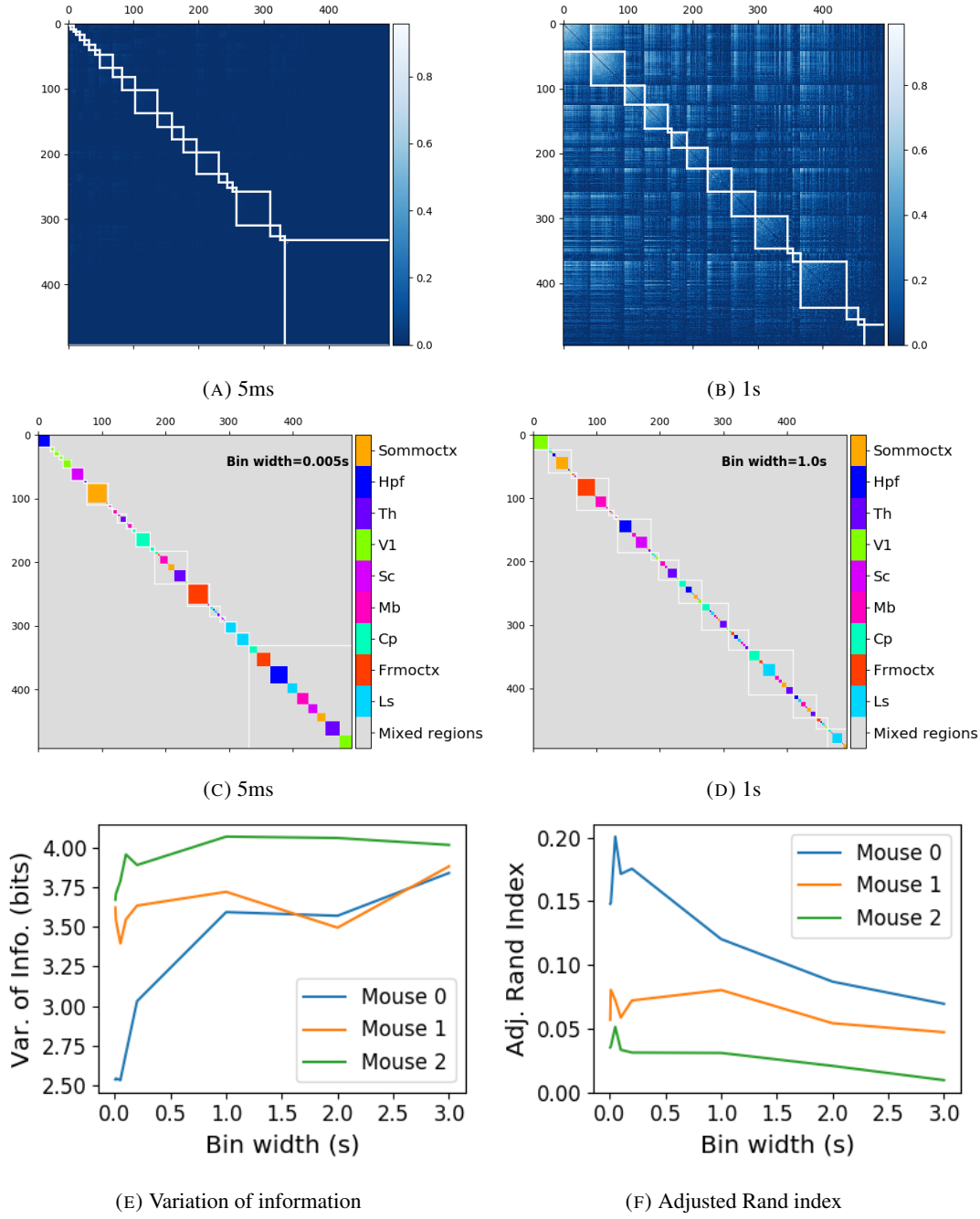


FIGURE 3.16: (A-B) Absolute correlation matrices with detected communities indicated by white lines. These communities are based on the absolute value of the total correlation between each pair of cells. Those entries within a white square indicate that both of those neurons are in the same community. Matrices shown are for 5ms and 1s time bin widths respectively. Main diagonal entries were set to 0. (C-D) Matrices showing the anatomical distribution of pairs along with their community membership. Regional membership is indicated by the colour bar. (E) Variation of information between the anatomical division of the cells, and the detected communities. (F) Adjusted Rand index between the anatomical division, and the detected communities.

3.5. Discussion

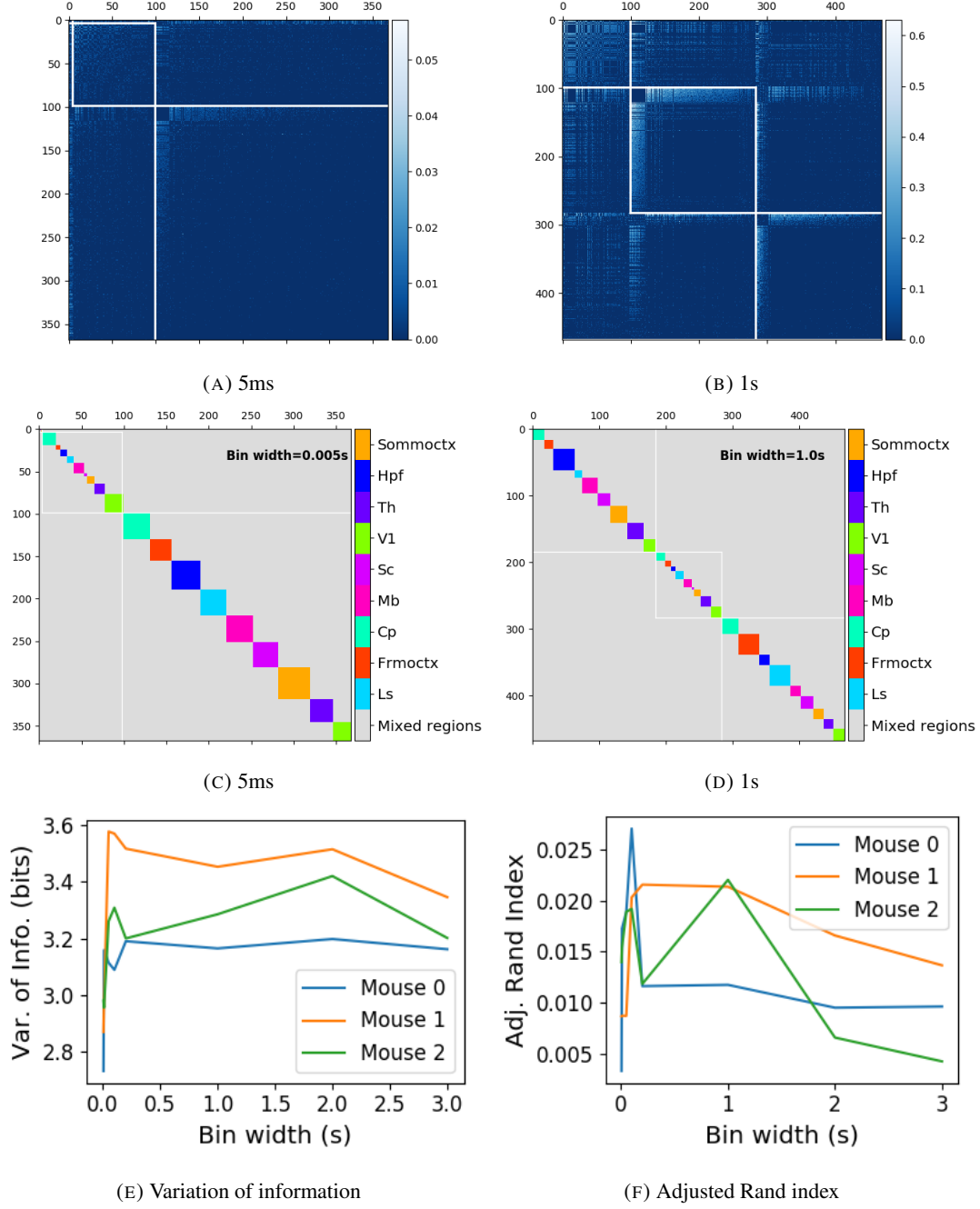


FIGURE 3.17: (A-B) Sign reversed rectified correlation matrices with detected communities indicated by white lines. Those entries within a white square indicate that both of those neurons are in the same community. Matrices shown are for 5ms and 1s time bin widths respectively. Main diagonal entries were set to 0. (C-D) Matrices showing the anatomical distribution of pairs along with their community membership. Regional membership is indicated by the colour bar. (E) Variation of information between the anatomical division of the cells, and the detected communities. (F) Adjusted Rand index between the anatomical division, and the detected communities.

1788 A number of studies have found that the timescale of correlated behaviour induced by a
1789 stimulus can be modulated by the stimulus structure and behavioural context. For example,
1790 the spike train correlations between cells in weakly electric fish are modulated by the spa-
1791 tial extent of the stimulus (Litwin-Kumar, Chacron, and Doiron, 2012), and neurons in the
1792 marmoset primary auditory cortex modulate their spike timing (and therefore correlation) in
1793 response to stimulus features without modulating their firing rate (deCharms and Merzenich,
1794 1996). Furthermore, the width of the time bins over which spike counts are measured has
1795 been shown to have an effect on the magnitude of those correlations (Cohen and Kohn, 2011).
1796 Despite this, very little research has been done comparing correlation measures from the same
1797 dataset at different timescales. We investigated this by varying the time bin width used to bin
1798 spike times into spike counts from as short as 5ms up to 3s.

1799 In order to further investigate the effect of these correlations at different timescales, we
1800 regarded our neuronal ensemble as a weighted undirected graph, where each neuron is rep-
1801 resented by a node, and the weight on each edge is the correlation between the neurons
1802 connected by that edge. We then applied a novel clustering method from network science
1803 (Humphries et al., 2019) to identify communities in these networks. Communities in a net-
1804 work graph refer to sets of nodes that are more strongly connected to each other than the
1805 nodes outside of their set. Another way to put this is to say that the nodes in a community
1806 are more strongly connected than *expected*. What connection strength might be expected is
1807 defined by a null network model. We chose a null network model that matched the sparsity
1808 and total strength of our correlation based data networks. So, if two cells were in the same
1809 community, those cells were more correlated than would be expected given the correlation
1810 strength of their ensemble.

1811 These networks, and the community detection process, were completely agnostic of the
1812 anatomical division of the cells in our ensemble. When we compared the detected commu-
1813 nities with the anatomical division of the cells using distance and similarity measures for
1814 clusterings, we found that the detected communities were more similar to the anatomical
1815 division at shorter timescales. That is, when we used a wider time bin to count spikes, and
1816 computed pairwise correlations with these spike counts, the correlated communities tended to
1817 exist within anatomical regions at shorter timescales, and tended to span anatomical regions
1818 at longer timescales. This could reflect localised functional correlations at short time scales
1819 rippling outwards across brain regions at longer timescales. The brain may be processing
1820 some information quickly locally, and carrying out further, perhaps more detailed, represen-
1821 tation over a longer timescale across many regions using the representations that were just

3.5. Discussion

1822 built locally.

1823 These changes in communities across timescales could also be driven by the anatomy
1824 of the individual cells. For example, it may simply take longer to transmit action potentials
1825 over longer distances, hence correlated activity over longer timescales will exist between
1826 anatomical regions, rather than within. However, the switch to almost exclusively multi-
1827 regional functional networks at 1s bin widths, rather than a mixture of multi-region, and
1828 single-region suggests that the inter-regional correlations either overpower, or inhibit the
1829 local correlations. So there may be more at play than just timescales.

1830 We acknowledged that the region spanning correlated communities that we detected at
1831 longer time scales could exist due to collating activity driven by distinct spontaneous activi-
1832 ties. In order to account for this, we modelled the spike counts as a linear function of the
1833 top 500 principal components of a video of the mouse's face filmed simultaneously with the
1834 electrophysiological readings. We applied our network noise rejection and community de-
1835 tection process to the weighted undirected networks formed by the spike count correlations
1836 (or noise correlations) and the signal correlations that we calculated using our model. For the
1837 spike count correlation networks, we found much the same results as for the total correlations
1838 as described above. For the signal correlations, the communities detected in these networks
1839 bore little relation to the anatomical division of the cells. Recent findings have shown that
1840 behavioural data accounts for correlations in many brain regions that would otherwise be
1841 dismissed as noise (Stringer et al., 2019), our finding to shows that these correlations are still
1842 governed by the timescale division between local communication and across-region commu-
1843 nication.

1844 There is a lot of room for further investigation based on this research. For a start, the
1845 data that we used here were collected from nine different regions in the mouse brain, but
1846 none of these regions were part of the somatosensory cortex. Given that a mouse experiences
1847 so much of its environment through its sense of smell, some data from this region would be
1848 interesting to investigate. On the same theme, the mice in the experiment from which the
1849 data were collected were headfixed and placed on a rotating ball, but were otherwise behav-
1850 ing spontaneously. Had these mice been exposed to a visual, aural, or olfactory stimulus,
1851 we could have examined the responses of the cells in the brain regions corresponding to vi-
1852 sion, hearing, and olfaction, and compared these responses to the responses from the other
1853 brain regions. Furthermore, we could have investigated the interaction between the sets of
1854 responses.

1855 Another space for further investigation is the community detection. The algorithm that we

1856 used here never detects overlapping communities. But functional communities could indeed
1857 have overlaps. Clustering methods that detect overlapping clusters do exist (Baadel, Thabtah,
1858 and Lu, 2016). Applying one of those algorithms could yield some interesting results. Also,
1859 the community detection algorithm that we used here cannot process graphs with negative
1860 weights, this forced us to separate positive and negative correlations before applying our
1861 network noise rejection and community detections process, or use the absolute value of our
1862 correlations. A community detection algorithm that can work on weighted undirected graphs
1863 with negative weights could yield some interesting results here.

1864 **Chapter 4**

1865 **A simple two parameter distribution
1866 for modelling neuronal activity and
1867 capturing neuronal association**

1868 *Abstract*

1869 Recent developments in electrophysiological technology have lead to an increase in the size
1870 of electrophysiology datasets. Consequently, there is a requirement for new analysis tech-
1871 niques that can make use of these new datasets, while remaining easy to use in practice. In
1872 this work, we fit some one or two parameter probability distributions to spiking data collected
1873 from a mouse exposed to visual stimuli. We show that the Conway-Maxwell-binomial dis-
1874 tribution is a suitable model for the number of active neurons in a neuronal ensemble at any
1875 given moment. This distribution fits these data better than binomial or beta-binomial distribu-
1876 tions. It also captures the correlated activity in the primary visual cortex induced by stimulus
1877 onset more effectively than simply measuring the correlations, at short timescales (< 10ms).
1878 We also replicate the finding of Churchland et al (2010) relating to stimulus onset quenching
1879 neural variability in cortical areas, and we show a correspondence between this quenching
1880 and changes in one of the parameters of the fitted Conway-Maxwell-binomial distributions.

1881 **4.1 Introduction**

1882 Recent advances in electrophysiological technology, such as ‘Neuropixels’ probes (Jun et al.,
1883 2017) have allowed extracellular voltage measurements to be collected from larger numbers
1884 of cells than traditional methods, in multiple brain regions simultaneously, and routinely.
1885 These larger datasets require innovative methods to extract information from the data in a
1886 reasonable amount of time, ‘reasonable’ being subjective in this case.

1887 Theoretically, all the information at any given moment in an electrophysiological dataset
1888 with n neurons could be captured by calculating the probability distribution for every possi-
1889 ble spiking pattern. This would require defining a random variable with 2^n possible values, a
1890 task that quickly becomes impossible as n increases. Attempts at approximating this random
1891 variable often involve measuring pairwise or higher order correlations (Schneidman et al.,
1892 2006; Flach, 2013; Ganmor, Segev, and Schneidman, 2011). But pairwise correlations may
1893 not be enough to characterise instantaneous neural activity (Tkačik et al., 2014). Further-
1894 more, these kinds of models tend to ignore the temporal structure of neuronal data, in favour
1895 of smaller model size, and scalability.

1896 Higher order correlations would be helpful here, but defining and quantifying these cor-
1897 relations can be tricky (Staude, Grün, and Rotter, 2010). If we use the interaction parameters
1898 arising from the exponential family model as measures of higher order correlations, mea-
1899 suring these correlations becomes computationally impractical quite quickly (the number
1900 of ‘three neuron correlations’ to measure scales with $(^n_3)$). In this work, we dispense with
1901 measuring correlations directly, and we attempt to characterise correlated behaviour using a
1902 parameter in statistical model.

1903 In this work, we examined the ability of simple distributions to model the number of
1904 active (spiking) neurons in a neuronal ensemble at any given timepoint. We compared a
1905 little-known distribution named the Conway-Maxwell-binomial distribution to the binomial
1906 distribution and the beta-binomial distribution. The binomial distribution is a probability dis-
1907 tribution over the number of successes in a sequence of independent and identical Bernoulli
1908 trials. The beta-binomial distribution is similar, but allows for a bit more flexibility while still
1909 being a model for heterogeneity. Similar to the binomial and beta-binomial, the Conway-
1910 Maxwell-binomial distribution is a probability distribution over the number of successes in a
1911 series of Bernoulli trials, but allows over- and under-dispersion relative to the binomial dis-
1912 tribution. This distribution should therefore be a good candidate for our purposes. We found
1913 that Conway-Maxwell-binomial distribution was usually the best candidate of the three that

4.2. Data

1914 we examined.

1915 We also observed some interesting changes in the number of active neurons in the primary
1916 visual cortex and hippocampus at stimulus onset and some changes in this activity in the
1917 thalamus which were sustained for the full duration of the stimulus presentation. This let us
1918 know that there were some responses to model.

1919 We found that fitting a Conway-Maxwell-binomial distribution was a better method of
1920 capturing association between neurons than measuring the spike count correlation for the
1921 short time bins that we used (< 10ms).

1922 Finally, we also wanted to investigate parallels between the parameters of the Conway-
1923 Maxwell-binomial distribution and quantities that have been established as relevant to sen-
1924 sory processing. So, we replicated the findings made by Churchland et al. (2010) relating
1925 to a reduction in neural variability at stimulus onset in the macaque cortical regions, but for
1926 data taken from the mouse primary visual cortex. We compared these findings to the values
1927 of the fitted Conway-Maxwell-binomial distribution parameters.

1928 4.2 Data

1929 We used data collected by Nick Steinmetz and his lab ‘CortexLab at UCL’ (Steinmetz, Caran-
1930 dini, and Harris, 2019). The data can be found online ¹ and are free to use for research
1931 purposes.

1932 Two ‘Phase3’ Neuropixels (Jun et al., 2017) electrode arrays were inserted into the brain
1933 of an awake, head-fixed mouse for about an hour and a half. These electrode arrays recorded
1934 384 channels of neural data each at 30kHz and less than $7\mu\text{V}$ RMS noise levels. The sites
1935 are densely spaced in a ‘continuous tetrode’-like arrangement, and a whole array records
1936 from a 3.8mm span of the brain. One array recorded from visual cortex, hippocampus, and
1937 thalamus, the other array recorded from motor cortex and striatum. The data were spike-
1938 sorted automatically by Kilosort and manually by Nick Steinmetz using Phy. In total 831
1939 well-isolated individual neurons were identified.

1940 4.2.1 Experimental protocol

1941 The mouse was shown a visual stimulus on three monitors placed around the mouse at right
1942 angles to each other, covering about ± 135 degrees azimuth and ± 35 degrees elevation.

¹<http://data.cortexlab.net/dualPhase3/>

1943 The stimulus consisted of sine-wave modulated full-field drifting gratings of 16 drift di-
1944 rections ($0^\circ, 22.5^\circ, \dots, 337.5^\circ$) with 2Hz temporal frequency and 0.08 cycles/degree spatial
1945 frequency displayed for 2 seconds plus a blank condition. Each of these 17 conditions were
1946 presented 10 times in a random order across 170 different trials. There were therefore 160
1947 trials with a drifting-grating visual stimulus present, and 10 trials with a blank stimulus.

1948 **4.3 Methods**

1949 **4.3.1 Binning data**

1950 We converted the spike times for each cell into spike counts by putting the spike times into
1951 time bins of a given ‘width’ (in milliseconds). We used time bins of 1ms, 5ms, and 10ms.
1952 We used different time bin widths to assess the impact of choosing a bin width.

1953 **4.3.2 Number of *active* neurons**

1954 To count the number of active neurons in each neuronal ensemble, we split the time interval
1955 for each trial into bins of a given width. We counted the number of spikes fired by each cell
1956 in each bin. If a cell fired *at least* one spike in a given bin, we regarded that cell as active in
1957 that bin. We recorded the number of active cells in every bin, and for the purposes of further
1958 analysis, we recorded each cell’s individual spike counts.

1959 It should be noted that when we used a bin width of 1ms, the maximum number of
1960 spikes in any bin was 1. For the wider time bins, some bins had spike counts greater than
1961 1. Consequently when using a bin width of 1ms, the number of active neurons and the total
1962 spike count of a given bin were identical. But for wider bin widths, the total spike count was
1963 greater than the number of active neurons.

1964 So for the 1ms bin width, the activity of a neuron and the number of spikes fired by that
1965 neuron in any bin can be modelled as a Bernoulli variable. But for wider time bins, only the
1966 activity can be modelled in this way.

1967 **4.3.3 Moving windows for measurements**

1968 When taking measurements (e.g. moving average over the number of active neurons) or
1969 fitting distributions (eg. the beta binomial distribution) we slid a window containing a certain
1970 number of bins across the data, and made our measurements at each window position. For
1971 example, when analysing 1ms bin data, we used a window containing 100 bins, and we slid

4.3. Methods

Bin width (ms)	Window size (bins)	Window size (ms)	Windows per trial
1ms	100	100ms	296
5ms	40	200ms	286
10ms	40	400ms	266

TABLE 4.1: Details of the different bin width and analysis window sizes used when binning spike times, and analysing those data.

1972 the window across the time interval for each trial moving 10 bins at a time. So that for
 1973 3060ms of data, we made 296 measurements.

1974 For the 5ms bin width data, we used windows containing 40 bins, and slid the window 2
 1975 bins at a time when taking measurements.

1976 For the 10ms bin width data, we used windows containing 40 bins, and slid the window
 1977 1 bin at a time when taking measurements (see table 4.1 for concise details).

1978 By continuing to use windows containing 40 bins, we retained statistical power but sac-
 1979 rificed the number of measurements taken.

1980 There was an interval between each trial with a grey image in place of the moving of
 1981 the moving bar stimulus. This interval varied in time. But we included some of this interval
 1982 when recording the data for each trial. We started recording the number of active neurons,
 1983 and the number of spikes from each neuron from 530ms before each trial until 1030ms after
 1984 each trial. This way, we could see the change in our measurements at the onset of a stimulus
 1985 and the end of stimulus presentation.

1986 As mentioned in section 4.3.2, we recorded the number of active neurons in each bin, and
 1987 the spike count for each neuron in each bin. The actual measurements we took using these
 1988 data in each window were as follows:

1989 **Moving average** The average number of active cells in each window.

1990 **Moving variance** The variance of the number of active cells in each window.

1991 **Average correlation** We measured the correlation between the spike counts of each pair of
 1992 cells in the ensemble, and took the average of these measurements.

1993 **Binomial p** We fitted a binomial distribution to the data in each window and recorded the
 1994 fitted probability of success, p in each case.

1995 **Beta-binomial α, β** We fitted a beta-binomial distribution to the data in each window, and
 1996 recorded the values of the fitted shape parameters, α and β , of each distribution.

1997 **Conway-Maxwell-binomial distribution p, ν** We fitted a Conway-Maxwell-binomial dis-
1998 tribution to the data in each window, and recorded the fitted values of p and ν for each
1999 distribution.

2000 **Log-likelihoods** We also recorded the log-likelihood of each of the fitted distributions for
2001 each window.

2002 **4.3.4 Fano factor**

The *Fano factor* of a random variable is defined as the ratio of the variable's variance to its mean.

$$F = \frac{\sigma^2}{\mu} \quad (4.1)$$

2003 We measured the Fano factor of the spike count of a given cell by measuring the mean and
2004 variance of the spike count across trials, and taking the ratio of those two quantities. When
2005 calculated in this way the Fano factor can be used as a measure of neural variability that
2006 controls for changes in the firing rate. This is similar to the calculation used in (Churchland
2007 et al., 2010).

2008 **4.3.5 Probability Distributions suitable for modelling ensemble activity**

2009 We present here three different probability distributions that could be suitable to model the
2010 number of active neurons in an ensemble. Each distribution has the set $\{0, \dots, n\}$ as its sup-
2011 port, where n is the number of neurons in the ensemble. These are simple distributions with
2012 either two or three parameters each. However, we regard n as known when using these dis-
2013 tributions for modelling, so in effect each distribution has either one or two free parameters.

2014 **Association**

2015 *Association* between random variables is similar to the correlation between random variables
2016 but is more general in concept. The correlation coefficient is a measure of association; and
2017 association doesn't necessarily have a mathematical definition like correlation does. Essen-
2018 tially, an association between two random variables is a dependency of any kind. Positively
2019 associated variables tend to take the same value, and negatively associated variables tend to
2020 take different values. In this research, we work with probability distributions of the num-
2021 ber of successes in a set of Bernoulli trials. These Bernoulli variables may or may not be
2022 associated.

4.3. Methods

2023 A probability distribution over the number of successes in n Bernoulli trials, where the
2024 Bernoulli variables may be associated, could constitute a good model for the number of active
2025 neurons in an ensemble of n neurons. As long as the observation period is divided into time
2026 bins short enough so that any neuron is unlikely to fire more than spike in any time bin.

2027 **Binomial distribution**

The binomial distribution is a two parameter discrete probability distribution that can be thought of as a probability distribution the number of successes from n independent Bernoulli trials, each with the same probability of success. The parameters of the binomial distribution are n the number of trials, and $0 \leq p \leq 1$, the probability of success for each of these trials. A random variable with the binomial distribution can take values from $\{0, \dots, n\}$.

The probability mass function of the distribution is

$$P(k; n, p) = \binom{n}{k} p^k (1-p)^{n-k} \quad (4.2)$$

2028 As a model for the activity of a neuronal ensemble, the main problem with the binomial
2029 distribution is that it treats each neuron, represented as a Bernoulli trial, as independent. It is
2030 well known that neurons are not independent, and that correlated behaviour between neurons
2031 is vital for representing sensory information (Cohen and Maunsell, 2009). The binomial dis-
2032 tribution falls short in this regard, but it is useful as performance benchmark when assessing
2033 the performance of other models.

2034 **Beta-binomial distribution**

2035 The beta distribution is the conjugate distribution of the binomial distribution. The beta-
2036 binomial distribution is the combination of the beta distribution and the binomial distribution,
2037 in that the probability of success for the binomial distribution is sampled from the beta dis-
2038 tribution. This allows the beta-binomial distribution to capture some over dispersion relative
2039 to the binomial distribution.

The beta-binomial distribution is a three parameter distribution, n the number of Bernoulli trials, and $\alpha \in \mathbb{R}_{>0}$ and $\beta \in \mathbb{R}_{>0}$ the shape parameters of the beta distribution. The probability mass function for the beta-binomial distribution is

$$P(k; n, \alpha, \beta) = \binom{n}{k} \frac{B(k + \alpha, n - k + \beta)}{B(\alpha, \beta)} \quad (4.3)$$

2040 where $B(\alpha, \beta)$ is the beta function.

This probability distribution can be reparametrised in a number of ways. One of which defines new parameters π and ρ by

$$\pi = \frac{\alpha}{\alpha + \beta} \quad (4.4)$$

$$\rho = \frac{1}{\alpha + \beta + 1} \quad (4.5)$$

2041 This reparametrisation is useful because π acts as a location parameter analogous to the p
2042 parameter of a binomial distribution. A value of $\rho > 0$ indicates over-dispersion relative to a
2043 binomial distribution.

2044 As a model for the activity of a neuronal ensemble, the beta-binomial distribution is
2045 more suitable than a binomial distribution because the over-dispersion of the beta-binomial
2046 distribution can be used to model positive association between the neurons. An extreme
2047 example of this over-dispersion/positive association can be seen in figure 4.1b. In this figure,
2048 the neurons are positively associated and so tend to take the same value, consequently the
2049 probability mass of the beta-binomial distribution builds up close to $k = 0$ and $k = n$. It is
2050 worth noting that the location parameter for each distribution has the same value, $p = \pi =$
2051 0.5.

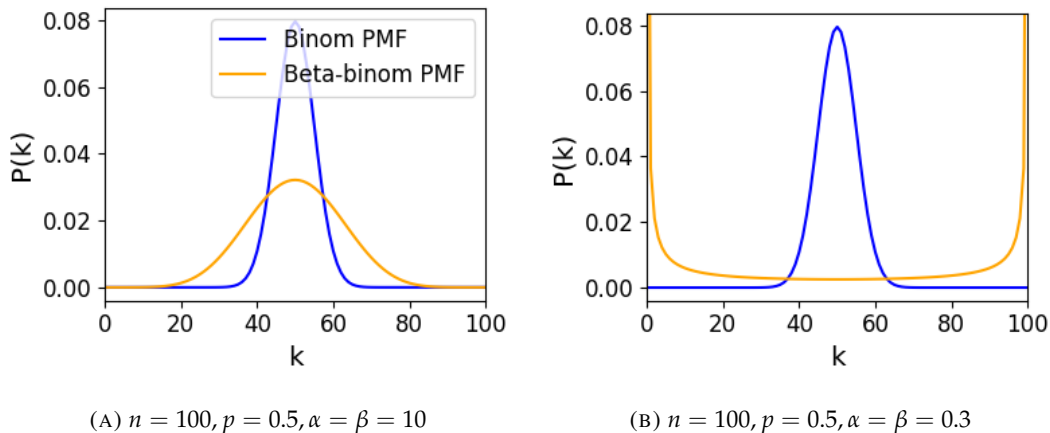


FIGURE 4.1: Figures showing the over-dispersion possible for a beta-binomial distribution relative to a binomial distribution. Parameters are shown in the captions.

2052 **Conway-Maxwell-binomial distribution**

2053 The Conway-Maxwell-binomial distribution (COMb distribution) is a three parameter generalisation of the binomial distribution that allows for over dispersion and under dispersion

4.3. Methods

relative to the binomial distribution. The parameters of the distribution are n the number of Bernoulli trials, and two shape parameters $0 \leq p \leq 1$, and $\nu \in \mathbb{R}$.

The probability mass function of the COMb distribution is

$$P(k; n, p, \nu) = \frac{1}{S(n, p, \nu)} \binom{n}{k}^{\nu} p^k (1-p)^{n-k} \quad (4.6)$$

where

$$S(n, p, \nu) = \sum_{j=0}^n \binom{n}{j}^{\nu} p^j (1-p)^{n-j} \quad (4.7)$$

The only difference between this PMF and the PMF for the standard binomial is the introduction of ν and the consequent introduction of the normalising function $S(n, p, \nu)$.

Indeed, if $\nu = 1$ the COMb distribution is identical to the binomial distribution with the same values for n and p . We can see in figure 4.2d that the KL-divergence $D_{KL}(P_{COMb}(n, p, \nu) || P_{Bin}(n, p)) = 0$ along the line where $\nu = 1$. The analytical expression for the divergence is

$$D_{KL}(P_{COMb}(k; n, p, \nu) || P_{Bin}(k; n, p)) = (\nu - 1) E_{P_{COMb}(k; n, p, \nu)} \left[\log \binom{n}{k} \right] \quad (4.8)$$

$$- \log S(n, p, \nu) \quad (4.9)$$

At $\nu = 1$, we have $S(n, p, 1)$ which is just the sum over the binomial PMF, so $S(n, p, 1) = 1$ and therefore $D_{KL}(P_{COMb}(n, p, \nu) || P_{Bin}(n, p)) = 0$.

If $\nu < 1$ the COMb distribution will exhibit over-dispersion relative to the binomial distribution. If $p = 0.5$ and $\nu = 0$ the COMb distribution is the discrete uniform distribution, and if $\nu < 0$ the mass of the COMb distribution will tend to build up near $k = 0$ and $k = n$. This over-dispersion represents positive association in the Bernoulli variables. An example of this over-dispersion can be seen in figure 4.2b.

If $\nu > 1$ the COMb distribution will exhibit under-dispersion relative to the binomial distribution. The larger the value of ν the more probability mass will build up at $n/2$ for even n , or at $\lfloor n/2 \rfloor$ and $\lceil n/2 \rceil$ for odd n . This under-dispersion represents negative association in the Bernoulli variables. An example of this under-dispersion can be seen in figure 4.2a.

It should be noted that the p parameter of the COMb distribution does not correspond to the mean of the distribution, as is the case for the binomial p parameter, and beta-binomial π parameter. That is, the COMb p parameter is not a location parameter. An illustration of this can be seen in figure 4.2c. This is because an interaction between the p and ν parameters skews the mean. There is no analytical expression for the mean of the COMb distribution.

ν	Relative dispersion	Association between neurons/variables
< 1	over	positive
1	none	none
> 1	under	negative

TABLE 4.2: Relative dispersion of the COMb distribution, and association between Bernoulli variables as represented by the value of the ν parameter.

2075 Since the COMb distribution has the potential to capture positive and negative associa-
2076 tions between the neurons/Bernoulli variables, it should be an excellent candidate for mod-
2077 elling the number of active neurons in a neuronal ensemble.

2078 We wrote a dedicated Python package to enable easy creation and fitting of COMb dis-
2079 tribution objects. The format of the package imitates the format of other distribution objects
2080 from the `scipy.stats` Python package. The COMb package can be found here:

2081 https://github.com/thomasjdelaney/Conway_Maxwell_Binomial_Distribution

2082 4.3.6 Fitting

2083 We fitted binomial, beta-binomial, and Conway-Maxwell-binomial (COMb) distributions to
2084 the neural activity in each of the overlapping windows covering each trial. To fit the distribu-
2085 tions we minimised the appropriate negative log likelihood function using the data from the
2086 window.

There is an analytical solution for maximum likelihood estimate of the binomial distribu-
tion's p parameter.

$$\hat{p} = \frac{1}{n} \sum_{i=1}^N k_i \quad (4.10)$$

2087 We minimised the negative log likelihood function of the beta-binomial distribution nu-
2088 merically. We calculated the negative log likelihood for a sample directly, by taking the sum
2089 of the log of the probability mass function for each value in the sample. We minimised the
2090 negation of that function using the `minimise` function of the `scipy.optimize` Python
2091 package.

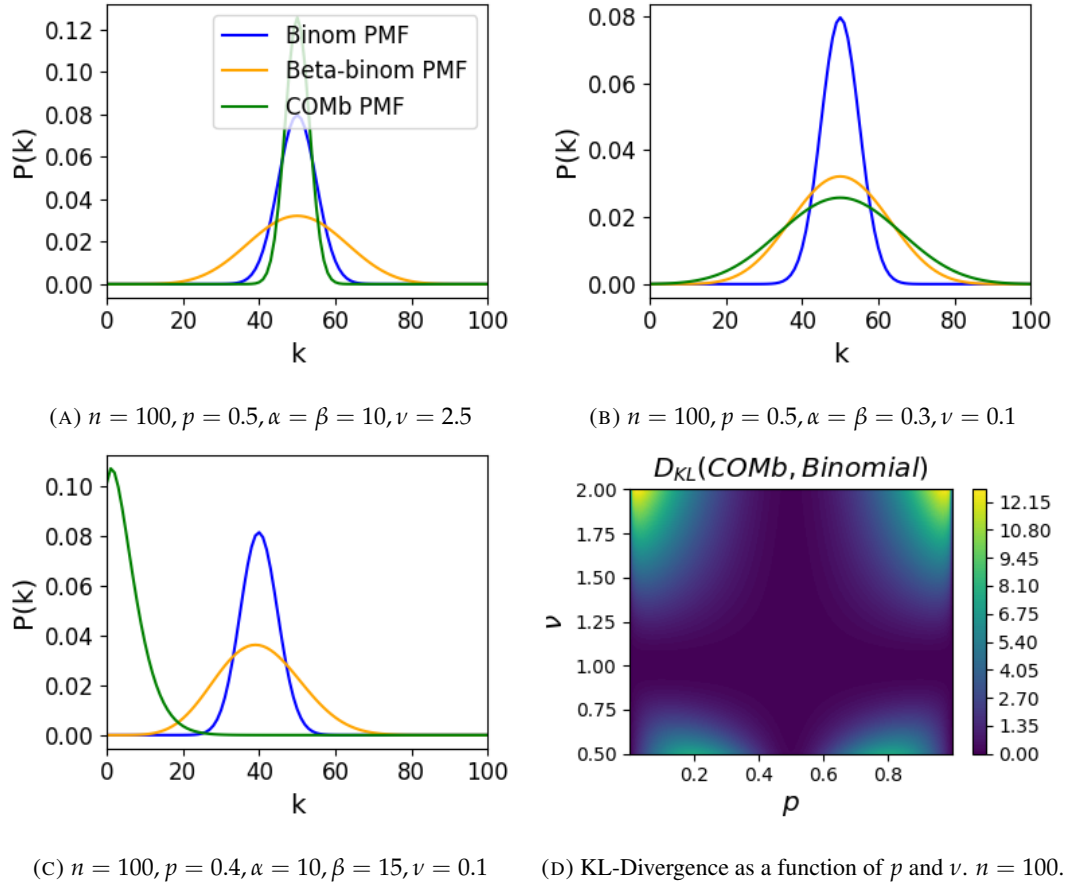


FIGURE 4.2: Figures showing (A) the under-dispersion and (B) over-dispersion permitted by the COMb distribution relative to a binomial distribution. (C) illustrates that the p parameter of the COMb distribution does not correspond to the mean of the distribution, as it does for the binomial and beta-binomial distributions. (D) shows a heatmap for the value of the Kullback-Liebler divergence between the COMb distribution and the standard binomial distribution with same value for n , as a function of p and ν . Parameters are shown in the captions.

The log likelihood function of the COMb distribution given some sample $\{k_1, \dots, k_N\}$ is

$$\ell(p, \nu | k_1, \dots, k_N) = N [n \log(1 - p) - \log S(n, p, \nu)] \quad (4.11)$$

$$+ \log \frac{p}{1 - p} \sum_{i=1}^N k_i \quad (4.12)$$

$$+ \nu \sum_{i=1}^N \log \binom{n}{k_i} \quad (4.13)$$

2092 We minimised the negation of this function using numerical methods. More specifically, we
2093 used the `minimise` function of the `scipy.optimize` Python package.

2094 **4.3.7 Goodness-of-fit**

2095 After fitting, we measured the goodness-of-fit of each model/distribution with their log like-
2096 lihood. We calculated this directly using the `logpmf` functions of the distribution objects in
2097 Python.

2098 **4.4 Results**

2099 We defined a neuron as *active* in a time bin if it fires at least one spike during the time interval
2100 covered by that bin. We measured the number of active neurons in the primary visual cortex
2101 of a mouse in 1ms bins across 160 trials of a moving bar visual stimulus. We then slid a
2102 100ms window across these 1ms bins taking measurements, and fitting distributions along
2103 the way. We did the same for neurons in the thalamus, hippocampus, striatum, and motor
2104 cortex. We repeated the analysis for 5ms time bins with 40 bin windows, and 10ms time bins
2105 with 40 bin windows.

2106 **4.4.1 Increases in mean number of active neurons and variance in number of
2107 active neurons at stimulus onset in some regions**

2108 We measured the average number of active neurons, and the variance of the number of active
2109 neurons in a 100ms sliding window starting 500ms before stimulus onset until 1000ms after
2110 stimulus onset. We found differences in the response across regions. There were no observed
2111 changes in response to the stimulus in the motor cortex or the striatum. The changes in the
2112 other regions are detailed below.

4.4. Results

2113 Primary visual cortex

2114 We found a transient increase in both the average and variance of the number of active neu-
2115 rons at stimulus onset, followed by a fall to pre-stimulus levels, followed by another transient
2116 increase (see figure 4.3). The oscillation in both of these measurements appear to reflect the
2117 frequency of the stimulus (see Data section 4.2.1), and it is known that stimulus structure can
2118 influence response structure(Litwin-Kumar, Chacron, and Doiron, 2012). We see a similar
2119 but lower amplitude oscillation at the end of the stimulus presentation.

2120 Hippocampus

2121 In the hippocampus we observed a transient increase in the average number of active neurons
2122 and in the variance of the number of active neurons at stimulus onset (see figure 4.4). The
2123 increase lasted about 125ms, and the subsequent fall to baseline took the a similar amount of
2124 time.

2125 Thalamus

2126 In the thalamus we observed a transient increase in the both the average and variance of
2127 the number of active neurons on stimulus onset, followed by a fall to pre-stimulus levels,
2128 followed by a sustained increase until the stimulus presentation ends.

2129 As one you might expect for a visual stimulus, the change in the average number of active
2130 neurons was greatest in the primary visual cortex. In this region, this quantity doubled on
2131 stimulus onset. In contrast, in the hippocampus and the thalamus, the average number of
2132 active neurons only increased by a fraction of the unstimulated baseline value. The duration
2133 of the response in V1 and the hippocampus at stimulus onset was 300 – 400ms, but the
2134 response in the thalamus appeared to last for the duration of stimulus presentation. The V1
2135 also showed a change in the average number of active neurons at stimulus end. The change
2136 was similar to that observed at stimulus onset, but smaller in magnitude (see figures 4.3, 4.4,
2137 and 4.5)

2138 4.4.2 Conway-Maxwell-binomial distribution is usually a better fit than bino- 2139 mial or beta-binomial

2140 Since the Conway-Maxwell-binomial distribution has not been fitted to neuronal data before,
2141 it is not clear that it would be a better fit than the binomial or beta-binomial distributions.
2142 In order to find out which parametric distribution was the best fit for the largest proportion

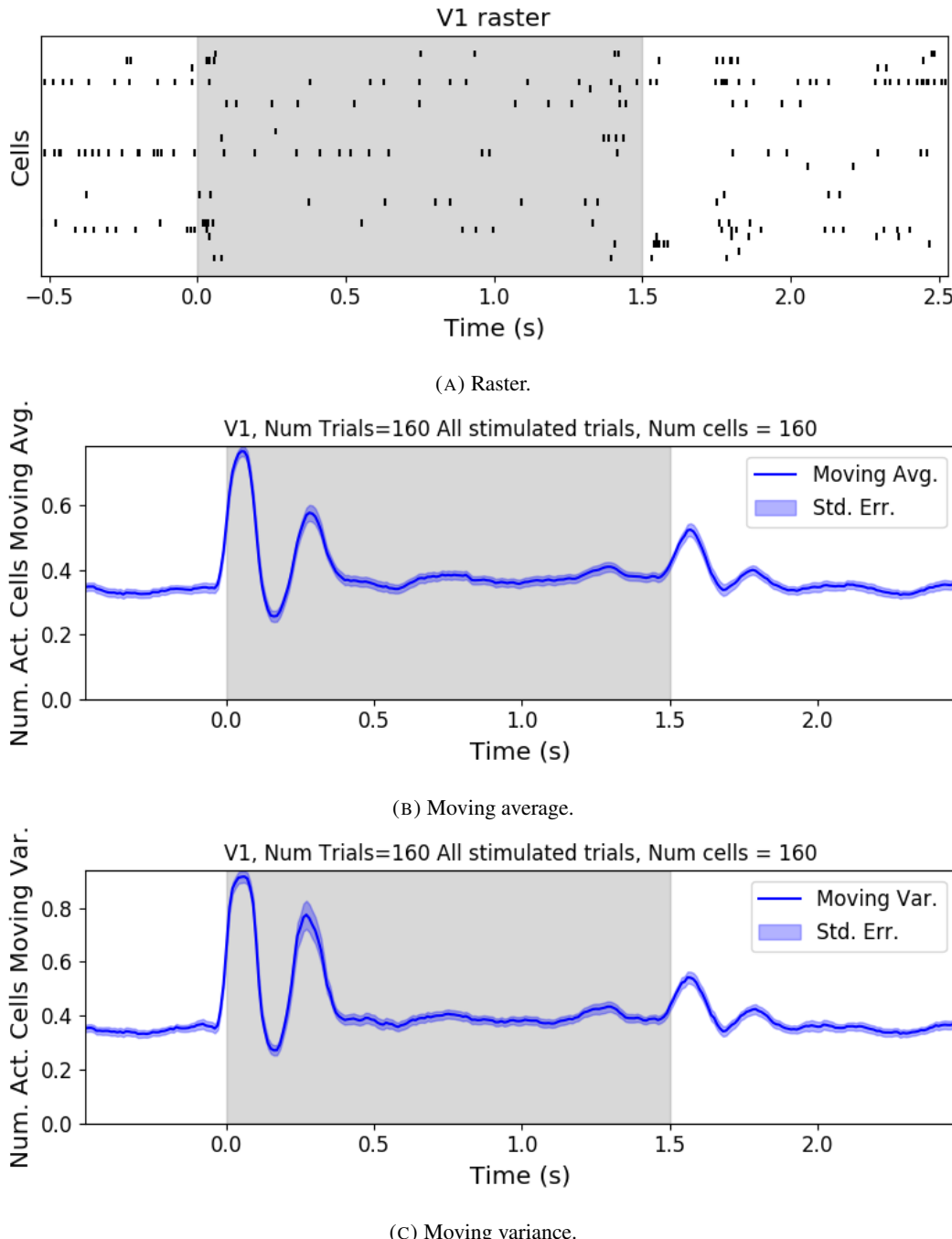


FIGURE 4.3: (A) Raster plot showing the spikes fired by 33 randomly chosen neurons in the primary visual cortex. (B-C) (B) average and (C) variance of the number of active neurons, measured using a sliding window 100ms wide, split into 100 bins. The midpoint of the time interval for each window is used as the timepoint (x-axis point) for the measurements using that window. The grey shaded area indicates the presence of a visual stimulus. The opaque line is an average across the 160 trials that included a visual stimulus of any kind. We can see a transient increase in the average number of active neurons and the variance of this number, followed by a fluctuation and another increase.

4.4. Results

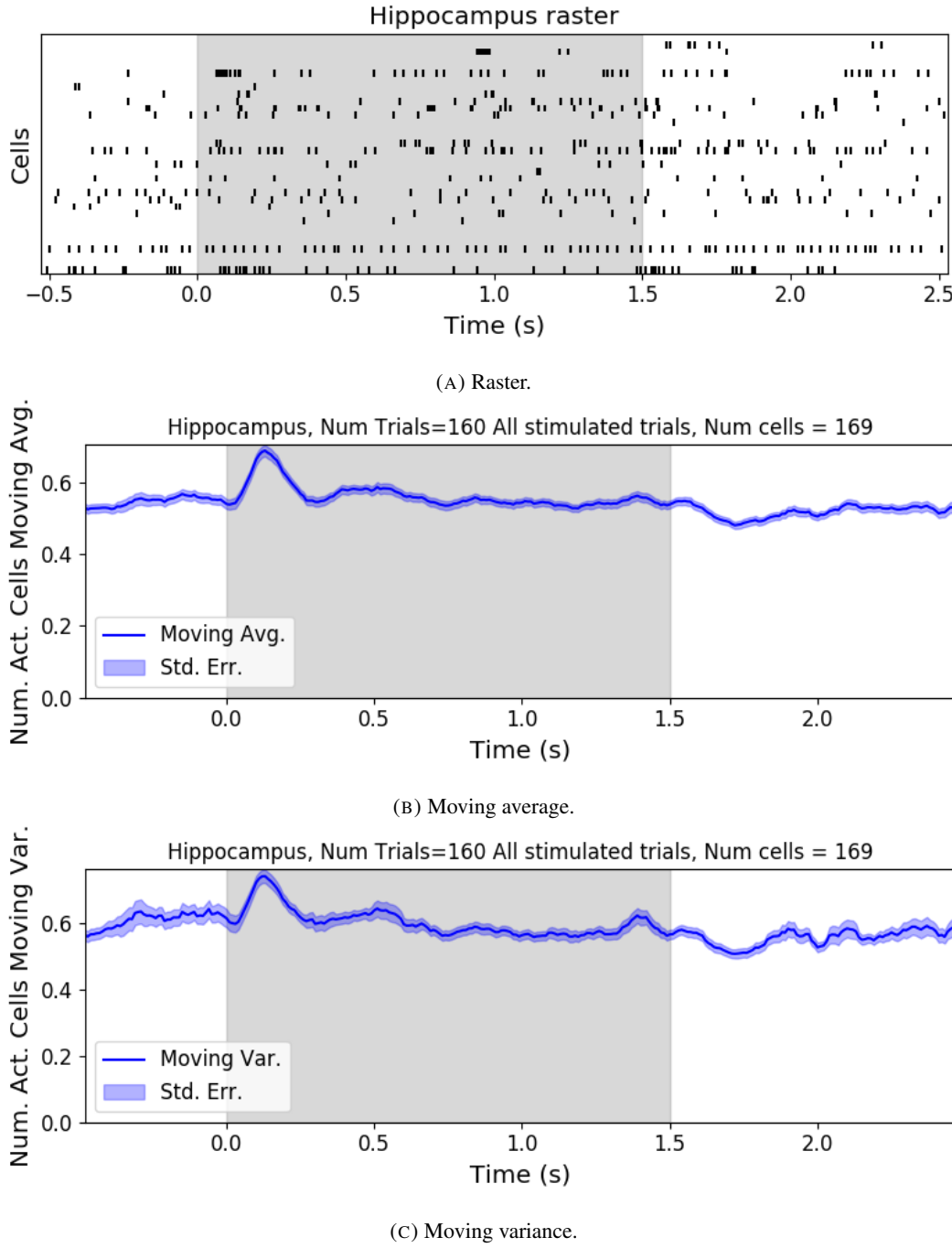


FIGURE 4.4: (A) Raster plot showing the spikes fired by 33 randomly chosen neurons in the hippocampus. (B-C) (B) average and (C) variance of the number of active neurons, measured using a sliding window 100ms wide, split into 100 bins. The midpoint of the time interval for each window is used as the timepoint (x-axis point) for the measurements using that window. The grey shaded area indicates the presence of a visual stimulus. The opaque line is an average across the 160 trials that included a visual stimulus of any kind. We can see a transient increase in the average number of active neurons and the variance of this number at stimulus onset.

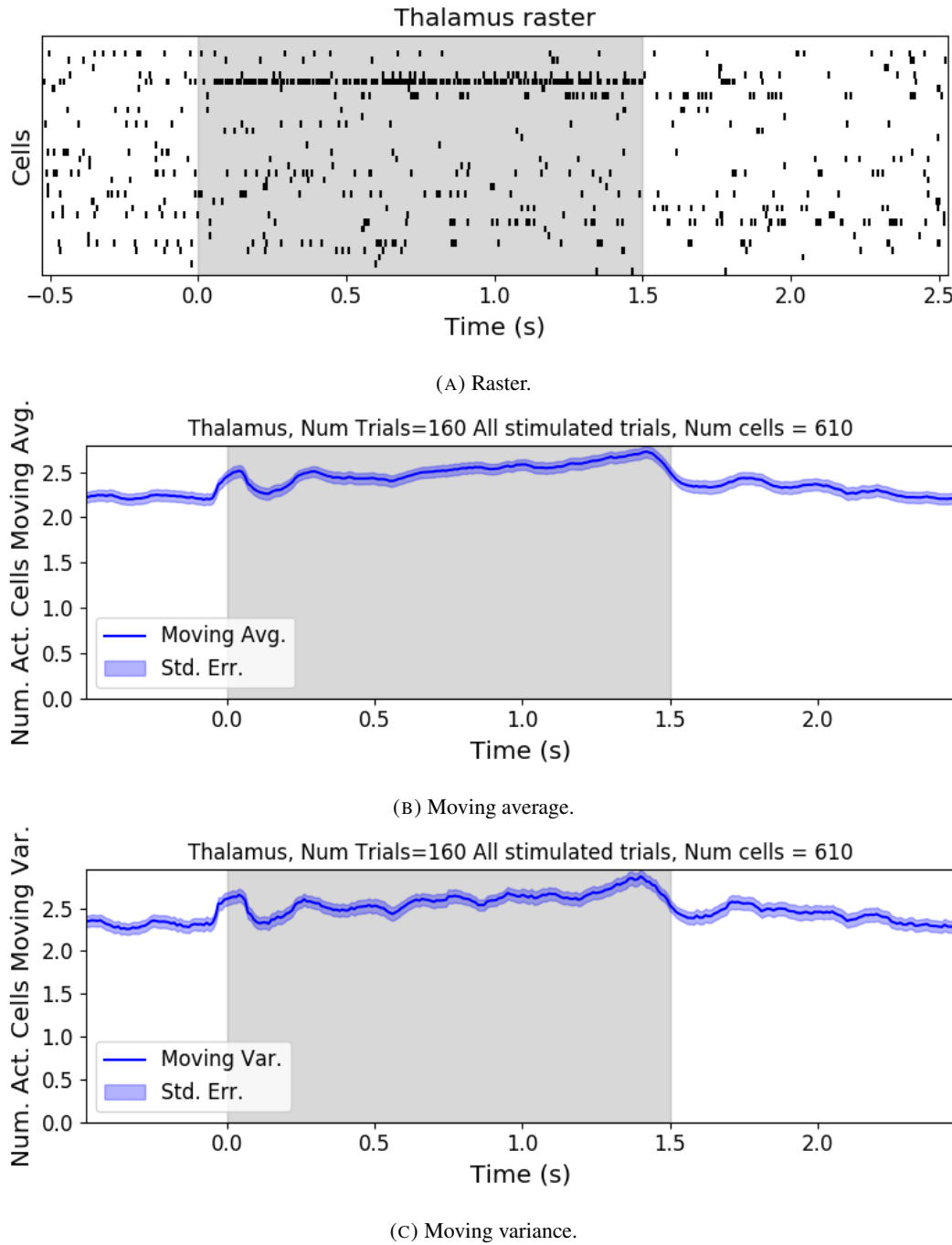
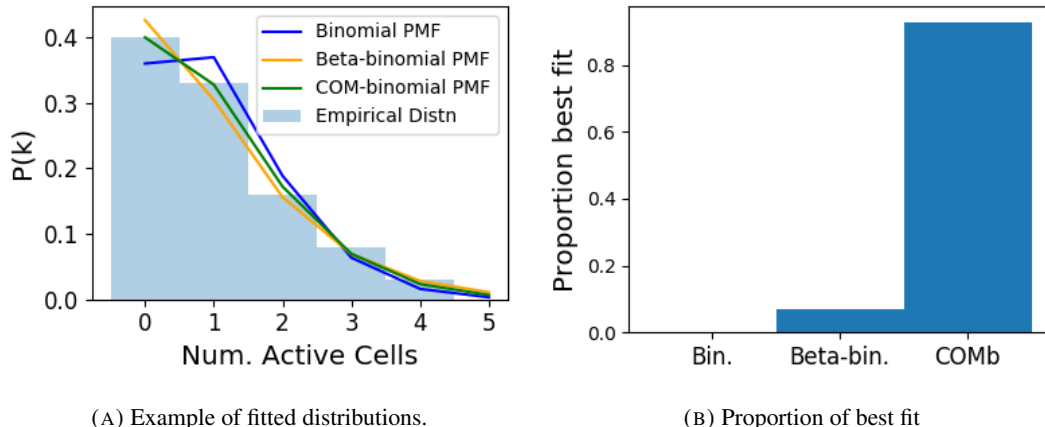


FIGURE 4.5: (A) Raster plot showing the spikes fired by 33 randomly chosen neurons in the thalamus. (B-C) (B) average and (C) variance of the number of active neurons, measured using a sliding window 100ms wide, split into 100 bins. The midpoint of the time interval for each window is used as the timepoint (x-axis point) for the measurements using that window. The grey shaded area indicates the presence of a visual stimulus. The opaque line is an average across the 160 trials that included a visual stimulus of any kind. We can see an immediate increase at stimulus onset, a subsequent fall, and another sustained increased until the stimulus presentation ends.

4.4. Results

of our data, we fit a binomial, a beta-binomial, and a Conway-Maxwell-binomial (COMb) distribution to each window for each bin width, and each region. Then we assessed the goodness-of-fit of each distribution by calculating the log-likelihood of each fitted distribution using the associated sample. We measured the proportion of samples for which each distribution was the best fit, for each bin width value and each region.

We found that the COMb distribution was the best fit for most of the samples regardless of bin width or region. The bin width had an effect on the number of samples for which the COMb distribution was the best fit. The results are summarised in table 4.3. For a bin width of 1ms, the COMb distribution was the best fit for over 90% of samples, the beta-binomial distribution was the best fit for less than 10% of samples, and the binomial distribution was the best fit for less than 1% of samples, across regions. For 5ms bins, the COMb distribution was the best fit for 70 – 80% of samples, the beta-binomial distribution was the best fit for 20 – 30% of the samples, and again the binomial distribution was the best fit for less than 1% of samples, across regions. Finally, for 10ms bins, the COMb distribution was the best fit for 53 – 80% of samples, the beta-binomial distribution was the best fit for 20 – 47% of the samples, and the binomial distribution was the best fit for less than 0.1% of samples, across regions.



(A) Example of fitted distributions.

(B) Proportion of best fit

FIGURE 4.6: (A) An example of the binomial, beta-binomial, and Conway-Maxwell-binomial distributions fitted to a sample of neural activity. The Conway-Maxwell-binomial distribution is the best fit in this case. The histogram shows the empirical distribution of the sample. The probability mass function of each distribution is indicated by a different coloured line. (B) Across all samples in all trials, the proportion of samples for which each fitted distribution was the best fit. The Conway-Maxwell-binomial distribution was the best fit for 93% of the samples taken from V1 using a bin width of 1ms.

Bin Width (ms)	Binomial	Beta-binomial	COMb
1ms	< 1%	< 10%	> 90%
5ms	< 0.1%	20 – 30%	70 – 80%
10ms	< 0.1%	20 – 47%	53 – 80%

TABLE 4.3: Proportion of samples for which each distribution was the best fit, grouped by bin width. The COMb distribution is the best fit most of the time.

2160 **4.4.3 Conway-Maxwell-binomial distribution captures changes in association
2161 at stimulus onset**

2162 We fit a Conway-Maxwell-binomial (COMb) distribution to the number of active neurons in
2163 the 1ms time bins in a 100ms sliding window. We also measured the correlation coefficient
2164 between the spike counts of all possible pairs of neurons, and took the average of these
2165 coefficients. We did this for all the trials with a visual stimulus. We observed a reduction in
2166 the COMb distribution's ν parameter at stimulus onset from around 1 to between 0 and 1 (see
2167 figure 4.7a). A value of ν less than 1 indicates positive association between the neurons (see
2168 section 4.3.5). We might expect to see this positive association reflected in the correlation
2169 coefficients, but this is not the case. We see no change in the time series of average correlation
2170 measures at stimulus onset.

2171 This may be due to the very short time bin we used in this case. We know that using small
2172 time bins can artificially reduce correlation measurements (Cohen and Kohn, 2011). In this
2173 case, fitting the COMb distribution may be a useful way to measure association in a neuronal
2174 ensemble over very short timescales (< 10ms).

2175 **4.4.4 Replicating stimulus related quenching of neural variability**

2176 Churchland et al. (2010) inspected the effect of a stimulus on neural variability. One of the
2177 measures of neural variability that they employed was the Fano factor of the spike counts of
2178 individual cells (see section 4.3.4). They found a reduction in neural variability as measured
2179 by the Fano factor in various cortical areas in a macaque at the onset of various visual stimuli,
2180 or a juice reward (Churchland et al., 2010).

2181 We measured the Fano factor of the spike count of each cell in each brain region, during
2182 each trial. We measured the mean and standard error of these Fano factors from 500ms
2183 before stimulus onset until 1000ms after stimulus end. For the primary visual cortex, we
2184 found a transient reduction in the Fano factor immediately after stimulus onset. We used
2185 a Mann-Whitney U test to check that the Fano factors measured in a window starting at

4.4. Results

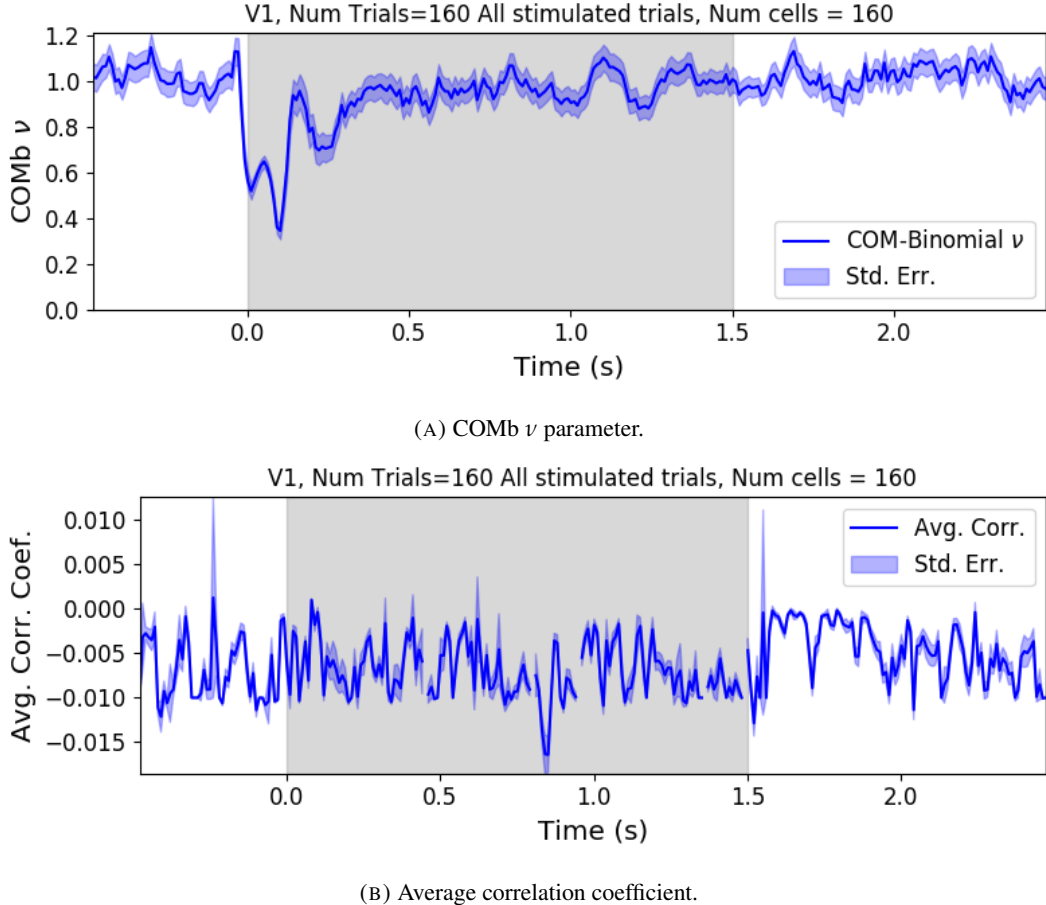


FIGURE 4.7: (A) We fit a Conway-Maxwell-binomial distribution to the number of active neurons in 1ms time bins of a 100ms sliding window. We did this for all trials with a visual stimulus and took the average across those trials. We see a transient drop in value for the distribution's ν parameter at stimulus onset. This shows an increase in positive association between the neurons. (B) We measured the correlation coefficient between the spike counts of all possible pairs of neurons in the same sliding window. The took the average of those coefficients. We also did this for every visually stimulated trial, and took the average across trials. The increase in positive association is not reflected with an increase in average correlation.

stimulus onset and ending 100ms later were significantly lower than the factors measured in a window ending at stimulus onset ($p < 0.001$, see figure 4.8a). We did not get this statistically significant result in any other region.

Our findings agree with those of Churchland et al. for the primary visual cortex. However Churchland also found a reduction in the Fano factor in the dorsal premotor cortex (PMd) at stimulus onset. Our measurements from the mouse motor cortex show no change at stimulus onset (see figure 4.8b). This could indicate some difference in the functionality of the motor cortex in a macaque and the motor cortex of a mouse.

Similar to these findings in the Fano factor, we found a reduction in the ν parameter of the COMB distribution on stimulus onset in V1 (figure 4.7a) and in no other region from

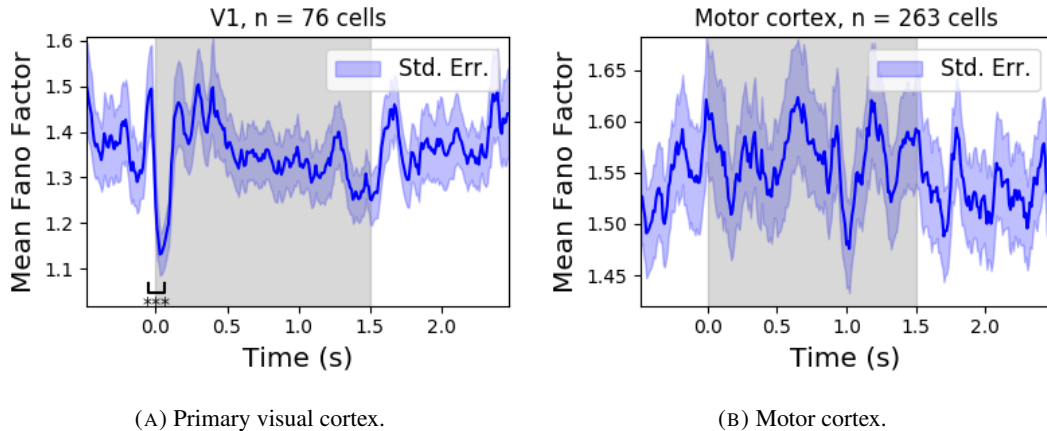


FIGURE 4.8: (A) The mean Fano factor of the spike counts of the cells in the primary visual cortex. Means were taken across cells first, then across trials. There was a significant decrease in the Fano factors immediately after stimulus onset. (B) The mean Fano factor of the spike counts of the cells in the motor cortex. No significant change in measurements at any point.

2196 which we had data. Specifically, the ν parameter reduced from around 1, to between 1 and 0.
 2197 This represents a change from no association between the neurons, to a positive association.
 2198 It is possible that this positive association may be responsible for the reduction in the Fano
 2199 factor.

2200 4.5 Discussion

2201 Our aim in this research was to develop a new statistical method for analysing the activity
 2202 of a neuronal ensemble at very short timescales. We wanted our method to use information
 2203 taken from the whole ensemble, but we also wanted the method to be quick and easy to
 2204 implement. It is likely that analysis methods with these characteristics will become valuable
 2205 as electrophysiological datasets include readings from more cells over longer time periods. In
 2206 this case, we used the number of active, or spiking, neurons in a very short time bin ($< 10\text{ms}$)
 2207 as a measure of ensemble activity.

2208 First of all, we showed that there were changes in response that we could model at these
 2209 very short time scales in some of the brain regions from which we had recordings. We ob-
 2210 served changes in the average number of active neurons, and the variance of the number of
 2211 active neurons in three different brain regions in response to visual stimuli. Since we know
 2212 that correlated behaviour is associated with sensory perception (deCharms and Merzenich,
 2213 1996), we might hope to measure the pairwise correlations within the neuronal population
 2214 in order to further investigate these responses. But, using such short time bins can produce

4.5. Discussion

artificially small spike count correlation measurements (Cohen and Maunsell, 2009). Overcoming this limitation was one of our objectives for our new method. In order to do this, we abandoned the idea of measuring the correlations directly and embraced the concept of *association*. In order to quantify the association between neurons, we used the Conway-Maxwell-binomial distribution to model the number of active (spiking) neurons in an ensemble as a sum of possibly associated Bernoulli random variables.

We showed that the Conway-Maxwell-binomial distribution performed better than the more common options of the binomial and beta-binomial distributions. Furthermore, we showed that the positively associated behaviour between neurons in the primary visual cortex could be captured by fitting a Conway-Maxwell-binomial distribution, but was not captured by the more standard approach of measuring the spike count correlation. The associated behaviour could not be measured using spike count correlations, because of the very short bins required to capture short timescale behaviour.

We replicated a famous result from Churchland et al (2010) relating to the quenching of neural variability in cortical areas at stimulus onset, and in doing so, we established a correspondence between the association quantifying parameter of the Conway-Maxwell-binomial (COMb) distribution and the neural variability as measured by the Fano factor. We found a reduction in the ν parameter of the COMB distribution at stimulus onset, indicating a change from no association to positive association between neurons in V1. We found a corresponding reduction in the Fano factor of the individual cells in V1. The positive association between neurons induced by the stimulus would constrain the neurons to fire at the same time. The stimulus also induced a larger number of neurons to spike. These two actions combined could cause an increase in the firing rate of individual cells that is greater in magnitude than the increase in firing rate variability. If this is indeed the case, then the association as captured by the COMB distribution could be regarded as one of the ‘natural parameters’ of the ensemble response for short timescales. That is, a quantity that directly measures some aspect of the behaviour of the ensemble. In this case, it the correlated behaviour of the individual neurons is captured.

This work could be just a first step in creating analysis methods based on the Conway-Maxwell-binomial distribution, or similar statistical models. One way to extend the method would be to pair it up with the ‘Population Tracking model’ (O’Donnell et al., 2017). This model attempts to characterise the interaction between an ensemble and each member of the ensemble by quantifying the probability of spiking for a given a cell, given the number of active cells in the whole population. Combining this model with the COMB distribution

2249 would give us a model that could accurately fit the number of active neurons at any moment,
2250 and that gives a probability of firing for each cell, and therefore probabilities for full spiking
2251 patterns, without adding a huge number of parameters to fit.

2252 A more complex way to extend the model would be to fit a Conway-Maxwell-binomial
2253 distribution to data recorded from multiple brain regions simultaneously, with a different fit
2254 for each region, then to analyse the temporal relationship between the fitted parameters of
2255 each region. If we analysed the time series of the COMB distribution parameters from the
2256 different regions, looking at cross-correlations between regions, this may give some results
2257 relating to the timescales in which information is processed in different brain regions.

2258 **Chapter 5**

2259 **Studies with practical limitations &**
2260 **negative results**

2261 *Abstract*

2262 Here I will present some details on research topics that I started, but that unfortunately did not
2263 lead anywhere useful. There are two pieces of research, based on two papers. Each paper is
2264 related to the overall theme of my PhD of analysing and modelling behaviours of populations
2265 of neurons. The first part is based on a model of parallel spike trains including higher order
2266 interactions by Shimazaki et al (2012). The second part is based on a multiscale model for
2267 making inferences on hierarchical data.

2268 **5.1 Dynamic state space model of pairwise and higher order neu-**
2269 **ronal correlations**

2270 In their paper Shimazaki et al (2012) aimed to model spike trains from populations of neurons
2271 in parallel, with pairwise and higher order dynamic interactions between the trains. They
2272 modelled the spike trains as multi-variate binary processes using a log-linear model, and they
2273 extracted spike interaction parameters using a Bayesian filter/EM-algorithm. They developed
2274 a goodness-of-fit measure for the model to test if including these higher order correlations
2275 is necessary for an accurate model. Their measure was based on the Bayes factor but they
2276 also assessed the suitability of higher order models using the AIC and BIC. So the increase
2277 in the number of parameters associated with fitting higher order interactions was taken into
2278 account. They tested the performance of the model on synthetic data with known higher
2279 order correlations. They used the model to look for higher order correlations in data from
2280 awake behaving animals. They use the model to demonstrate dynamic appearance of higher
2281 order correlations in the monkey motor cortex (Shimazaki et al., 2012).

2282 We used the available Python repository to implement the model, and we successfully
2283 worked through the tutorial provided. But we found that the model did not scale well to
2284 larger populations. We attempted to fit the model to a population of 10 neurons and found we
2285 didn't manage to finish the process. Since, our goal was to find a model to scale to hundreds
2286 or thousands of neurons, we decided that this model was no longer worth pursuing.

2287 **5.2 A multiscale model for hierarchical data applied to**
2288 **neuronal data**

2289 In their paper Kolaczyk et al (2001) developed a framework for a modelling hierarchically
2290 aggregated data, and making inferences based on a model arising from this framework. They
2291 assumed that a hierarchical aggregation existed on the data in question, where each element at
2292 each level of the hierarchy had some associated measurements, an associated mean process,
2293 which was the expected value of these measurements. They also assumed that the measure-
2294 ments of each parent were equal to the sum of the measurements from all of its children.
2295 They showed that these assumptions gave rise to a relationship between parent and child
2296 measurements across all levels of the hierarchy, where the product of the likelihood of the
2297 parameters of the lowest level of the hierarchy can be expressed as products of conditional
2298 likelihoods of the elements of higher levels of the hierarchy (Kolaczyk and Huang, 2010).

2299 They gave examples of these expressions for measurements sampled from Gaussian dis-
2300 tributions, and Poisson distributions, and showed the definitions of the hierarchical param-
2301 eters which reparametrise the distribution of these data taking the hierarchy into account.
2302 They go on to suggest prior distributions for this multiscale model, and integrate these priors
2303 to give posterior distributions for the measurements from each element at each level in the hi-
2304 erarchy, and expressions for the MAP estimated parameters of each the associated processes
2305 (Kolaczyk and Huang, 2010).

2306 We implemented their model in Python by creating some synthetic data from Poisson
2307 distributions, and defining a hierarchy by agglomerating these data. We calculated the MAP
2308 estimates using our knowledge of the hierarchy, and using the expressions given in the paper.
2309 We found that the MAP estimates were far less accurate than would be achieved by simply
2310 ignoring the hierarchy during estimation, and using a maximum likelihood approach. After
2311 that, we decided to move on.

2312 **Chapter 6**

2313 **Discussion**

2314 In this project, we attempted to address some of the challenges in data collection from
2315 large neuronal ensembles (specifically with calcium imaging) and some of the problems in
2316 analysing the data collected from large neuronal ensembles.

2317 Firstly, we investigated the relationship between cell biochemistry, action potentials and
2318 the fluorescence traces produced by fluorescent calcium indicators. We did this by building
2319 a biophysical model that takes in a spike train and returns the fluorescence trace that that
2320 spike would induce. The model included mechanics for the binding of calcium to fluorescent
2321 and endogenous mobile and immobile buffers, and the consequent changes in concentration
2322 of free and bounded calcium. The model consisted of 17 parameters, 13 of which were
2323 set according to data from the literature, and 4 of which were free parameters. We trained
2324 the model using simultaneously collected spiking and calcium imaging data (Berens et al.,
2325 2018). We fitted the model by matching the $\Delta F/F_0$ in response to an action potential, and
2326 by matching the power spectrum of the actual fluorescence trace. This meant that our model
2327 would include the correct amount of noise as well as return the correct change in amplitude
2328 in response to an action potential.

2329 Since our model produced fluorescence traces, we could apply spike inference algorithms
2330 to the modelled fluorescence traces that our model produced after training, and compare the
2331 performance of the algorithms on the modelled traces to their performance on the real traces.
2332 We used three spike inference algorithms, two of which were based on modelling the cal-
2333 cium trace as an autoregression (Friedrich and Paninski, 2016; Pnevmatikakis et al., 2016),
2334 and another inference algorithm that was a little more biologically inspired, but amounted to
2335 a very similar algorithm (Deneux et al., 2016). We compared the performance of the algo-
2336 rithms by using them to infer spikes from 20 real and modelled fluorescence traces induced
2337 by 20 corresponding real spike trains. We then used several binary classification measures
2338 (true positive rate, accuracy etc.) to asses the quality of the spike inference for the real and

2339 modelled fluorescence traces. We found that the spike inference algorithms performed sim-
2340 ilarly on real and modelled traces, showing that our model is capturing at least some of the
2341 characteristics of the real fluorescence traces.

2342 In order to investigate the effect of indicator characteristics on the modelled fluorescence
2343 trace and spike inference quality, we perturbed the indicator's affinity and dissociation rate
2344 in parallel, keeping the ratio of the two the same for all perturbations. We measured the SNR
2345 of the trace, and the true positive rate of the spike inference algorithms at each perturbed
2346 value pair. We found that perturbing the values lower caused in decrease in SNR and spike
2347 inference quality. This shows that our model could be used to test theoretical fluorescent cal-
2348 cium indicators without having to actually manufacture them. Experimental neuroscientists
2349 could also use our model to judge which indicator characteristics are most influential in their
2350 experimental context.

2351 We then investigated the effect of perturbing buffer concentration, and indicator concen-
2352 tration, on the signal-to-noise ratio of the modelled fluorescence trace and spike inference
2353 quality. This was a worthwhile experiment because endogenous buffer concentrations vary
2354 from cell to cell (Bartol et al., 2015; Maravall et al., 2000; Neher and Augustine, 1992), as
2355 does indicator expression (Chen et al., 2013). We found that extreme perturbations away
2356 from the indicator concentration taken from the literature lowered the SNR of the trace, and
2357 the spike inference quality. We also found that increases in the concentration of endogenous
2358 buffer above the value taken from the literature caused a decrease in the SNR and spike infer-
2359 ence quality. This reiterates that the indicator and endogenous buffers compete to bind with
2360 free calcium molecules, and this has an effect on fluorescence and consequently on spike
2361 inference.

2362 We then created some synthetic spike trains with controlled mean firing rates sampled
2363 the rates from an Ornstein-Uhlenbeck process. We found that the higher the firing rate, the
2364 lower the accuracy of the spike inference algorithms. But the mean firing could perhaps be
2365 inferred from the amplitude of the fluorescence traces. The higher firing rate, the higher the
2366 amplitude. Calibrating the model to facilitate and accurate measurement would require some
2367 kind of ground truth, but relative comparisons could be made without any other knowledge
2368 of the underlying spiking process.

2369 One obvious limitation to our model is the lack of binding mechanics for both the indi-
2370 cator and endogenous buffers. Greenberg et al included these mechanics in their successful
2371 spike inference model. We felt that the timescale of these binding mechanics was so small in
2372 comparison to the fluorescence dynamics that omitting them would make no difference. But

2373 it is possible that their inclusion would improve our model.

2374 After investigating the difficulties with inferring spiking data from calcium imaging data,
2375 we moved from data collection to analysis and we decided to implement a new network anal-
2376 ysis method on data from a neuronal ensemble. Using an electrophysiological dataset with
2377 spike sorted data from 9 different brain regions in 3 mice (Steinmetz, Carandini, and Harris,
2378 2019), we binned the spike times for each cell into spike counts for each cell and measured
2379 the correlation coefficients between these spike counts for a selection of cells evenly dis-
2380 tributed across the 9 regions. We repeated these measurements for time bin widths ranging
2381 from 5ms to 3s. We rectified these measurements and, for a given time bin width, used them
2382 as weights for a weighted undirected graph where each node represents a neuron, and the
2383 weight of each edge is the correlation between the neurons represented by the nodes on that
2384 edge. We applied a novel spectral analysis and community detection method (Humphries
2385 et al., 2019) to this network. This clustered the nodes in our ensemble into communities
2386 whose behaviour was more correlated than expected. Our measure of 'expected correlation
2387 strength' were based on a random network that matched our data network's sparsity and total
2388 weight. We compared the detected communities to the anatomical division of our cells using
2389 clustering comparison measures. We then conditioned the binned spike counts on the be-
2390 haviour of the mouse using the principal components of a video of the mouses face recorded
2391 simultaneously with the electrophysiology. We broke the total covariance down into 'spike
2392 count covariance' and 'signal covariance' components conditioning on the behavioural data
2393 and using the law of total covariance. We then repeated our analysis for spike count corre-
2394 lations, and signal correlation. Finally, since our community detection method was only valid
2395 on graphs with non-negative weights, we used different methods for creating a non-negative
2396 graph from our total correlations, and we repeated our analysis on those graphs.

2397 Our first finding was that the time bin width used to bin spike times into spike counts had
2398 a effect on the mean magnitude of the correlations measured. The wider the bin, the higher
2399 the correlations. Not only that, we separated the pairs into positively and negative correlated
2400 pairs, and we found that positively correlated pairs have greater correlation coefficients when
2401 using a wider bin, and negatively correlated pairs have more negative correlation coefficients
2402 when using a wider bin. We also found that the width of the bin used had an effect on the
2403 distribution of the spike counts. For smaller bin widths, the distribution of spike counts was
2404 better represented by a skewed distribution like the Poisson distribution. For wider bins, the
2405 spike counts were better represented by a Gaussian distribution.

2406 Next we investigated the differences between correlations within regions and between

regions. When we divided the pairs according to those two groups, we found that the mean within-region correlations were higher at every bin width, and the difference between the two means grew with increasing bin width. When we split the pairs of cells according to their regions, we found that the mean within-region correlations in any given region were usually greater than the mean between-region correlations for any region pair involving that region. The difference between the mean within-region correlation and the highest between-region correlations involving that region grew smaller with increasing bin width. To investigate this further, we plotted these mean correlations in matrices. Although the mean within-region correlations were usually the highest value in their row or column, as the bin width increased, the mean between-region correlations grew in magnitude relative to the within-region figure.

Next we chose a null network model, and we used the ‘Network Noise Rejection’ process (Humphries et al., 2019) to check for additional structure in our correlation based data network that was not captured by the null model. We found additional structure for any bin width that we used. We also found that the dimensionality of the additional structure reduced as we increased the bin width. This could mean that the processes or representations that take place over longer timescales within the brain also take place in a lower dimensional space.

We applied a community detection method (Humphries, 2011) to the signal correlation networks arising from the network noise rejection. We found that the number of communities detected decreased with increasing bin width. We also noticed that at shorter bin widths, the detected communities were more likely to consist of cells from one brain region only. We investigated this further by using clustering comparison methods to compare the detected communities with the anatomical division of the cells. We found that for short timescales $< 50\text{ms}$ correlated communities tended to exist within anatomical regions, and for longer timescales $> 100\text{ms}$, the correlated communities tended to exist across anatomical regions. This is broadly in agreement with a similar finding for EEG data from humans performing semantic or memory tasks (Stein and Sarnthein, 2000). Von Stein et al. (2000) found that visual processing taking place locally in the visual system was captured in the gamma frequency range (25 – 70Hz), while semantic processing was captured in the beta range (12 – 18Hz), and tasks involving mental imagery and working memory retention were captured in the theta and alpha ranges (4 – 8Hz, and 8 – 12Hz respectively).

We then conditioned our correlation measures on the the mouse’s behaviour. This allowed us to create spike count correlation (or noise correlation) networks, and signal correlation networks (Cohen and Kohn, 2011). We applied our analysis to these networks. For the

spike count correlation networks we found very similar results to the total correlation networks. More communities at smaller bin widths, and communities resembled the anatomical division at smaller bin widths. Given that recent findings show that behaviour can account for correlated spiking in many areas of the brain (Stringer et al., 2019), these results for the spike count correlation show that this correlated behaviour is still processed locally at short timescales, while processes and representations that take more time make use of correlated activity across multiple regions.

For the signal correlations, we still found additional structure in these networks. But we always detected a smaller number of communities. These communities also had no relation to the anatomical division of the cells. This result shows that there are groups of cells across multiple brain regions that are activated similarly by certain behaviours.

All of the networks so far were based on rectified correlation measures, because the network noise rejection and community detection processing is (currently) only valid for networks with non-negative weights. For the final part of our analysis, we tried different ways of transforming our total correlations into non-negative quantities before applying our analysis. First of all we took the absolute value of our correlation measures. Our results were very similar to those for the rectified correlations with the exception that we detected more communities consistently. It is possible that using this method detects both positively and negatively correlated communities.

We also tried reversing the sign of all the correlations, then rectifying the network. We hope that this would allow us to detect the negatively correlated communities. We did detect communities in these networks, but never more than three, and these communities bore no relationship with the anatomical distribution of the cells.

There is a lot of potential for network science applications in computational neuroscience. For example, some pairwise measure other than correlation coefficients could be used as the weights of the graph. A directed measure like synaptic connectivity could be used as the basis for directed graphs. The analysis methods applicable to directed graphs could give insights about the formation of synaptic connections, or the dynamic changes in these connections over time. Other methods of community detection could be used on directed or undirected graphs. We used a ‘hard’ clustering method in our research, that is, each neuron could be a member of one cluster/community only. ‘Fuzzy-clustering’ methods do exist, where each element of the set to be clustered could be a member of more than one cluster (Baadel, Thabtah, and Lu, 2016).

Having spent much time investigating correlated behaviour using coefficients of spike

counts, we decided to try another method for capturing correlated behaviour in neuronal ensembles. We used electrophysiological data taken from 5 brain regions of an awake mouse exposed to visual stimuli (Steinmetz et al., 2019). We modelled the number of active neurons in a given brain region as the number of successes in a collection of dependent Bernoulli random variables using the Conway-Maxwell-binomial distribution. To avoid violating the Bernoulli assumption, we binned the spike times using 1ms bins. The Conway-Maxwell-binomial distribution is a two parameter extension of the standard binomial distribution. The extra parameter allows the distribution to capture possible positive or negative association between the Bernoulli trials (Kadane, 2016). This means that we are assuming that all the neurons are dependent in the same way. This is not an accurate assumption, but it allows us model the data in a simple way.

First of all we established that there were changes in the number of active neurons in response to the visual stimuli. This was the case in the hippocampus, thalamus, and primary visual cortex. Each region had its own signature response. We measured the mean and variance of the number of active neurons in a sliding window starting before stimulus onset, and finishing after the end of stimulus presentation.

As well as the Conway-Maxwell-binomial distribution, we also fitted binomial, and beta-binomial distributions to the number of active neurons in a sliding window. We found that the Conway-Maxwell-binomial distribution was the best fit for over 90% of the samples. This means that the COMb distribution is capturing some dependency between the neurons, because the binomial distribution assumes independence. Also the COMb distribution captures this dependence more accurately than the beta-binomial distribution, which does have some capacity for over dispersion.

Next we showed that the Conway-Maxwell-binomial distribution captured the change in association at stimulus onset better than the correlation coefficient. The extremely small bin width artificially shrunk the correlation coefficient to the point where this measurement didn't detect any correlated activity. But the association parameter of the COMb distribution detected some positive association between the neurons at stimulus onset. So, for particularly short time bins, where neurons can be treated as Bernoulli random variables, the Conway-Maxwell-binomial distribution is a good way to capture correlated behaviour. There are other measurements for capturing association to which this distribution should be compared. Cross-correlograms could be used for some measure of synchrony, for example.

Finally, we replicated a famous finding of Churchland et al. (2010) relating to the quenching of neural variability at stimulus onset, thereby finding a parallel between this reduction

2508 in the Fano factor and a reduction in the association parameter of the COMb distribution.

2509 We showed that computational neuroscientists can make progress by being inventive with
2510 their statistical models. A similar distribution to investigate would be the Conway-Maxwell-
2511 Poisson distribution. This is similar to the standard Poisson distribution, but with an addi-
2512 tional parameter that allows for over- or under- dispersion relative to a Poisson distribution.
2513 This might be ideal for modelling firing rates of individual neurons. Some interaction be-
2514 tween the fitted parameters could capture the association between neurons.

2515 There is one technology that has the potential to take over from both electrophysiology
2516 and calcium imaging. The technique of voltage imaging has become more useful in recent
2517 years. The aim for neuroscience would be to develop a voltage imaging dye or protein that
2518 images the membrane potential of a neuron with enough spatial and temporal resolution to
2519 detect action potentials. Genetically encoded voltage indicators have been developed, and
2520 enable targeting of specific neuronal ensembles. But their spatial resolution is not yet high
2521 enough to single out individual cells (Bando et al., 2019). These indicators have the potential
2522 to take over from calcium imaging, and if imaging deep within the brain becomes possible,
2523 electrophysiology could also be replaced. This is speculation, but the potential is there.

²⁵²⁴ Bibliography

- ²⁵²⁵ Allen, William E. et al. (2019). “Thirst regulates motivated behavior through modulation of
²⁵²⁶ brainwide neural population dynamics”. In: *Science* 364.6437.
- ²⁵²⁷ Baadel, S., F. Thabtah, and J. Lu (2016). “Overlapping clustering: A review”. In: *2016 SAI*
²⁵²⁸ *Computing Conference (SAI)*, pp. 233–237.
- ²⁵²⁹ Baldassano, Christopher et al. (2017). “Discovering Event Structure in Continuous Narrative
²⁵³⁰ Perception and Memory”. In: *Neuron* 95.3, 709 –721.e5.
- ²⁵³¹ Bando, Yuki et al. (2019). “Genetic voltage indicators”. In: *BMC Biology* 17.1, p. 71.
- ²⁵³² Bartol, Thomas M. et al. (2015). “Computational reconstitution of spine calcium transients
²⁵³³ from individual proteins”. In: *Frontiers in Synaptic Neuroscience* 7, p. 17.
- ²⁵³⁴ Berens, Philipp et al. (May 2018). “Community-based benchmarking improves spike rate in-
²⁵³⁵ ference from two-photon calcium imaging data”. In: *PLOS Computational Biology* 14.5,
²⁵³⁶ pp. 1–13.
- ²⁵³⁷ Bezanson, Jeff et al. (Sept. 2012). “Julia: A Fast Dynamic Language for Technical Comput-
²⁵³⁸ ing”. In: *MIT*.
- ²⁵³⁹ Buccino, Alessio P. et al. (2019). “SpikeInterface, a unified framework for spike sorting”. In:
²⁵⁴⁰ *bioRxiv*.
- ²⁵⁴¹ Chen, Tsai-Wen et al. (July 2013). “Ultrasensitive fluorescent proteins for imaging neuronal
²⁵⁴² activity”. In: *Nature* 499, 295–300.
- ²⁵⁴³ Churchland, Mark M. et al. (2010). “Stimulus onset quenches neural variability: a widespread
²⁵⁴⁴ cortical phenomenon”. eng. In: *Nature neuroscience* 13.3. 20173745[pmid], pp. 369–378.
- ²⁵⁴⁵ Cohen, Marlene R. and Adam Kohn (2011). “Measuring and interpreting neuronal corre-
²⁵⁴⁶ lations”. In: *Nature Neuroscience* 14.7, pp. 811–819.
- ²⁵⁴⁷ Cohen, Marlene R. and John H. R. Maunsell (2009). “Attention improves performance pri-
²⁵⁴⁸ marily by reducing interneuronal correlations”. eng. In: *Nature neuroscience* 12.12. 19915566[pmid],
²⁵⁴⁹ pp. 1594–1600.
- ²⁵⁵⁰ Dana, Hod et al. (Sept. 2014). “Thy1-GCaMP6 Transgenic Mice for Neuronal Population
²⁵⁵¹ Imaging In Vivo”. In: *PloS one* 9, e108697.

- 2552 deCharms, R. Christopher and Michael M. Merzenich (1996). “Primary cortical representation of sounds by the coordination of action-potential timing”. In: *Nature* 381.6583,
2553 pp. 610–613.
- 2555 Deneux, Thomas et al. (July 2016). “Accurate spike estimation from noisy calcium signals
2556 for ultrafast three-dimensional imaging of large neuronal populations in vivo”. In: *Nature
2557 Communications* 7.1.
- 2558 Dombeck, Daniel A. et al. (2010). “Functional imaging of hippocampal place cells at cellular
2559 resolution during virtual navigation”. In: *Nature Neuroscience* 13.11, pp. 1433–1440.
- 2560 Éltes, Tímea et al. (2019). “Improved spike inference accuracy by estimating the peak am-
2561 plitude of unitary [Ca₂₊] transients in weakly GCaMP6f-expressing hippocampal pyra-
2562 midal cells”. In: *The Journal of Physiology* 597.11, pp. 2925–2947.
- 2563 Faas, Guido C. et al. (2011). “Calmodulin as a direct detector of Ca₂₊ signals”. In: *Nature
2564 Neuroscience* 14.3, pp. 301–304.
- 2565 Fiala, John C. and Kristen M. Harris (1999). *Dendrite Structure*.
- 2566 Flach, Boris (Sept. 2013). “A Class of Random Fields on Complete Graphs with Tractable
2567 Partition Function”. In: *IEEE transactions on pattern analysis and machine intelligence*
2568 35, pp. 2304–6.
- 2569 Forney, G. D. (1973). “The viterbi algorithm”. In: *Proceedings of the IEEE* 61.3, pp. 268–
2570 278.
- 2571 Fosdick, Bailey et al. (Aug. 2016). “Configuring Random Graph Models with Fixed Degree
2572 Sequences”. In: *SIAM Review* 60.
- 2573 Friedrich, Johannes and Liam Paninski (2016). “Fast Active Set Methods for Online Spike In-
2574 ference from Calcium Imaging”. In: *Advances in Neural Information Processing Systems*
2575 29. Ed. by D. D. Lee et al. Curran Associates, Inc., pp. 1984–1992.
- 2576 Ganmor, Elad, Ronen Segev, and Elad Schneidman (2011). “Sparse low-order interaction
2577 network underlies a highly correlated and learnable neural population code”. In: *Pro-
2578 ceedings of the National Academy of Sciences* 108.23, pp. 9679–9684.
- 2579 Girard, P., J. M. Hupé, and J. Bullier (2001). “Feedforward and Feedback Connections Be-
2580 tween Areas V1 and V2 of the Monkey Have Similar Rapid Conduction Velocities”. In:
2581 *Journal of Neurophysiology* 85.3. PMID: 11248002, pp. 1328–1331.
- 2582 Greenberg, David et al. (Nov. 2018). “Accurate action potential inference from a calcium
2583 sensor protein through biophysical modeling:” in:
- 2584 Gründemann, Jan et al. (2019). “Amygdala ensembles encode behavioral states”. In: *Science*
2585 364.6437.

Bibliography

- 2586 Hodgkin, A. L. and A. F. Huxley (1939). “Action Potentials Recorded from Inside a Nerve
2587 Fibre”. In: *Nature* 144.3651, pp. 710–711.
- 2588 Humphries, Mark et al. (Jan. 2019). “Spectral rejection for testing hypotheses of structure in
2589 networks”. In:
- 2590 Humphries, Mark D. (2011). “Spike-Train Communities: Finding Groups of Similar Spike
2591 Trains”. In: *Journal of Neuroscience* 31.6, pp. 2321–2336.
- 2592 Jun, James J. et al. (2017). “Fully integrated silicon probes for high-density recording of
2593 neural activity”. In: *Nature* 551.7679, pp. 232–236.
- 2594 Kadane, Joseph B. (June 2016). “Sums of Possibly Associated Bernoulli Variables: The
2595 Conway–Maxwell-Binomial Distribution”. In: *Bayesian Anal.* 11.2, pp. 403–420.
- 2596 Kilhoffer, Marie-Claude et al. (Sept. 1992). “Use of Engineered Proteins With Internal Tryp-
2597 topahan Reporter Groups and Perturbation Techniques to Probe the Mechanism of Ligand-
2598 Protein Interactions: Investigation of the Mechanism of Calcium Binding to Calmodulin”.
2599 In: *Biochemistry* 31.34, pp. 8098–8106.
- 2600 Koch, Christoff (1999). *Biophysics of Computation: Information Processing in Single Neu-
2601 rons*. Oxford University Press.
- 2602 Kolaczyk, Eric and Haiying Huang (Sept. 2010). “Multiscale Statistical Models for Hierar-
2603 chical Spatial Aggregation”. In: *Geographical Analysis* 33, pp. 95 –118.
- 2604 Lee, Suk-HO et al. (July 2000). “Differences in Ca²⁺ buffering properties between excitatory
2605 and inhibitory hippocampal neurons from the rat”. In: *The Journal of Physiology* 525.
- 2606 Litwin-Kumar, Ashok, Maurice Chacron, and Brent Doiron (Sept. 2012). “The Spatial Struc-
2607 ture of Stimuli Shapes the Timescale of Correlations in Population Spiking Activity”. In:
2608 *PLoS computational biology* 8, e1002667.
- 2609 Maravall, M et al. (May 2000). “Estimating intracellular calcium concentrations and buffer-
2610 ing without wavelength ratioing”. In: *Biophysical Journal* 78.5, pp. 2655–2667.
- 2611 Maugis, Pa (Jan. 2014). “Event Conditional Correlation: Or How Non-Linear Linear Depen-
2612 dence Can Be”. In:
- 2613 Meilă, Marina (2007). “Comparing clusterings—an information based distance”. In: *Journal
2614 of Multivariate Analysis* 98.5, pp. 873 –895.
- 2615 Murray, John D. et al. (2014). “A hierarchy of intrinsic timescales across primate cortex”. In:
2616 *Nature Neuroscience* 17.12, pp. 1661–1663.
- 2617 Neher, E. and G. J. Augustine (1992). “Calcium gradients and buffers in bovine chromaffin
2618 cells”. eng. In: *The Journal of physiology* 450. 1331424[pmid], pp. 273–301.

- 2619 O'Donnell, Cian et al. (Jan. 2017). "The population tracking model: a simple, scalable statistical model for neural population data". English. In: *Neural Computation* 29.1, pp. 50–93.
- 2622 Okun, Michael et al. (2015). "Diverse coupling of neurons to populations in sensory cortex". In: *Nature* 521.7553, pp. 511–515.
- 2624 Ouzounov, Dimitre G. et al. (2017). "In vivo three-photon imaging of activity of GCaMP6-labeled neurons deep in intact mouse brain". eng. In: *Nature methods* 14.4. 28218900[pmid], pp. 388–390.
- 2627 Patterson, Carolyn A. et al. (2014). "Similar adaptation effects in primary visual cortex and area MT of the macaque monkey under matched stimulus conditions". In: *Journal of Neurophysiology* 111.6. PMID: 24371295, pp. 1203–1213.
- 2630 Peron, Simon P. et al. (2015). "A Cellular Resolution Map of Barrel Cortex Activity during Tactile Behavior". In: *Neuron* 86.3, pp. 783–799.
- 2632 Pnevmatikakis, E.A. et al. (Jan. 2016). "Simultaneous Denoising, Deconvolution, and Demixing of Calcium Imaging Data". In: *Neuron* 89.2, pp. 285–299.
- 2634 Pnevmatikakis, Eftychios et al. (Nov. 2013). "Bayesian spike inference from calcium imaging data". In: *Conference Record - Asilomar Conference on Signals, Systems and Computers*.
- 2636 Pnevmatikakis, Eftychios et al. (Sept. 2014). "A structured matrix factorization framework for large scale calcium imaging data analysis". In:
- 2638 Schneidman, Elad et al. (2006). "Weak pairwise correlations imply strongly correlated network states in a neural population". eng. In: *Nature* 440.7087. 16625187[pmid], pp. 1007–1012.
- 2641 Shannon, C. E. (1948). "A Mathematical Theory of Communication". In: *Bell System Technical Journal* 27.3, pp. 379–423.
- 2643 Shimazaki, Hideaki et al. (2012). "State-space analysis of time-varying higher-order spike correlation for multiple neural spike train data". eng. In: *PLoS computational biology* 8.3. 22412358[pmid], e1002385–e1002385.
- 2646 Staude, Benjamin, Sonja Grün, and Stefan Rotter (2010). "Higher-Order Correlations and Cumulants". In: *Analysis of Parallel Spike Trains*. Ed. by Sonja Grün and Stefan Rotter. Boston, MA: Springer US, pp. 253–280.
- 2649 Stein, Astrid von and Johannes Sarnthein (2000). "Different frequencies for different scales of cortical integration: from local gamma to long range alpha/theta synchronization". In: *International Journal of Psychophysiology* 38.3, pp. 301 –313.

Bibliography

- 2652 Steinmetz, Nick, Matteo Carandini, and Kenneth D. Harris (2019). "Single Phase3" and
2653 "Dual Phase3" *Neuropixels Datasets*.
- 2654 Steinmetz, Nick et al. (Mar. 2019). "Eight-probe Neuropixels recordings during spontaneous
2655 behaviors". In:
- 2656 Stevenson, Ian H. and Konrad P. Kording (2011). "How advances in neural recording affect
2657 data analysis". In: *Nature Neuroscience* 14.2, pp. 139–142.
- 2658 Stringer, Carsen et al. (2019). "Spontaneous behaviors drive multidimensional, brainwide
2659 activity". In: *Science* 364.6437.
- 2660 Tada, Mayumi et al. (2014). "A highly sensitive fluorescent indicator dye for calcium imaging
2661 of neural activity in vitro and in vivo". In: *European Journal of Neuroscience* 39.11,
2662 pp. 1720–1728.
- 2663 Tian, Lin et al. (2009). "Imaging neural activity in worms, flies and mice with improved
2664 GCaMP calcium indicators". eng. In: *Nature methods* 6.12. 19898485[pmid], pp. 875–
2665 881.
- 2666 Tkačik, Gašper et al. (2014). "Searching for collective behavior in a large network of sen-
2667 sory neurons". eng. In: *PLoS computational biology* 10.1. 24391485[pmid], e1003408–
2668 e1003408.
- 2669 Treves, Alessandro and Stefano Panzeri (1995). "The Upward Bias in Measures of Informa-
2670 tion Derived from Limited Data Samples". In: *Neural Computation* 7.2, pp. 399–407.
- 2671 Vinh, Nguyen Xuan, Julien Epps, and James Bailey (Dec. 2010). "Information Theoretic
2672 Measures for Clusterings Comparison: Variants, Properties, Normalization and Correc-
2673 tion for Chance". In: *J. Mach. Learn. Res.* 11, 2837–2854.
- 2674 Vogelstein, Joshua T. et al. (Oct. 2010). "Fast nonnegative deconvolution for spike train infer-
2675 ence from population calcium imaging". In: *Journal of neurophysiology* 104.6, 295–300.
- 2676 Wierzynski, Casimir M. et al. (2009). ""State-Dependent Spike-Timing Relationships be-
2677 tween Hippocampal and Prefrontal Circuits during Sleep"". In: "Neuron" "61" ."4", "587
2678 –596".
- 2679 Zariwala, Hatim A. et al. (2012). "A Cre-dependent GCaMP3 reporter mouse for neuronal
2680 imaging in vivo". eng. In: *The Journal of neuroscience : the official journal of the Society
2681 for Neuroscience* 32.9. 22378886[pmid], pp. 3131–3141.
- 2682 Zou, Hui and Trevor Hastie (2005). "Regularization and variable selection via the Elastic
2683 Net". In: *Journal of the Royal Statistical Society, Series B* 67, pp. 301–320.